UNIVERSIDADE DE SANTIAGO DE COMPOSTELA

TESE DE DOUTORAMENTO

SEARCH FOR $K_S^0 \to \mu^+\mu^-$ AND TRIGGER DEVELOPMENTS AT LHCB

Miguel Ramos Pernas

ESCOLA DE DOUTORAMENTO INTERNACIONAL

PROGRAMA DE DOUTORAMENTO EN FÍSICA NUCLEAR E DE PARTÍCULAS

SANTIAGO DE COMPOSTELA

ANO 2020

DECLARACIÓN DO AUTOR DA TESE

Search for $K_S^0 \to \mu^+\mu^-$ and trigger developments at LHCb

D. Miguel Ramos Pernas

Presento a miña tese, seguindo o procedemento axeitado ao Regulamento, e declaro que:

1) A tese abarca os resultados da elaboración do meu traballo.
2) De selo caso, na tese faise referencia ás colaboracións que tivo este traballo.
3) A tese é a versión definitiva presentada para a súa defensa e coincide coa versión enviada en formato electrónico.
4) Confirmo que a tese non incorre en ningún tipo de plaxio doutros autores nin de traballos presentados por min para a obtención doutros títulos.

En Santiago de Compostela, 16 de marzo de 2020

Asdo. Miguel Ramos Pernas

AUTORIZACIÓN DO DIRECTOR/TITOR DA TESE

Search for $K_S^0 \to \mu^+\mu^-$ and trigger developments at LHCb

D. Diego Martínez Santos
Dna. Veronika Georgieva Chobanova
Dna. Jessica Prisciandaro
D. Cibrán Santamarina Ríos

INFORMAN:

Que a presente tese, correspóndese co traballo realizado por D. Miguel Ramos Pernas, baixo a miña dirección, e autorizo a súa presentación, considerando que reúne os requisitos esixidos no Regulamento de Estudos de Doutoramento da USC, e que como director desta non incorre nas causas de abstención establecidas na Lei 40/2015.

En Santiago de Compostela, 16 de marzo de 2020

Asdo. Diego Martínez Santos

Asdo. Veronika Georgieva Chobanova

Asdo. Jessica Prisciandaro

Asdo. Cibrán Santamarina Ríos

Acknowledgments

I want to start by lauding Máximo and Cibrán, who made my interest for particle physics grow and introduced me to the research world. They are both highly responsible for the start of my career as a scientist, and I think I would not be here if they had not encouraged me to follow this path. All the knowledge and skills that I have acquired during these years would not be possible without the help of my thesis directors: Diego, Jessica and Veronika, and neither without the support of Martino and Xabier, who taught me a lot of things about particle physics, and with whom I held many interesting discussions that helped me in order to become a better physicist. I feel also grateful for the help received from Marcos, who I think deserves a special mention for making me understand theoretical particle physics better, and for teaching me many important things about computing. I am also thankful to Abraham, for giving me a hand from the very beginning of my career as a researcher and for all his useful recommendations. I would like to thank also the other members of the LHCb team both from Santiago and from abroad, for fruitful discussions, for their support and for giving me the opportunity to take part of this big and beautiful project.

Cambio de lingua para referirme a toda a xente da casa. En primeiro lugar quero agradecer a tódolos meus compañeiros de batalla que durante estes anos compartiron momentos inesquecibles comigo en Santiago de Compostela, no CERN, e en distintas aventuras no estranxeiro; tanto aqueles que seguen loitando coma os que xa botaron a voar. De todos eles, quero mencionar especialmente a dúas rapazas que compartiron comigo momentos moi especiais durante a miña carreira como estudante de doutoramento. A primeira é María, á que considero unha experta axudando aos inexperimentados que dan os seus primeiros pasos no CERN, dos que formei parte. En segundo lugar quero agradecer enormemente a Miriam, coa que compartín innumerables aventuras no CERN e en conferencias, ademais de todas aquelas que xurdiron da convivencia compartindo despacho durante catro anos.

Non existen palabras para expresar o meu agradecemento aos meus pais Rosa e Eduardo, pola súa axuda incondicional e os ánimos que me deron durante toda a miña vida. Así mesmo, quero expresar a miña gratitude cara aos meus compañeiros de aventuras en orientación e natación por axudarme a desconectar do meu traballo e darme un respiro en momentos de estrés. Finalmente quero mencionar aos meus amigos, en especial a Sabela, Ana, Pablo, Aroa e Brais, por tódolos momentos que compartimos estes anos, polo seu apoio, e por ser capaces de manter a nosa amizade a pesar da distancia.

Miguel

Abstract

The Standard Model (SM) is, up to now, a robust model that describes with high accuracy the interactions between elementary particles. However, several processes, like the observation of neutrino oscillations or the presence of dark matter in the universe, constitute signs of physics beyond this model. The LHCb experiment, located at the European Organization for Nuclear Research (CERN), aims at contributing to clarify the picture we currently have about particle physics, and to understand the laws that rule our universe. By studying the decays of certain particles produced at the Large Hadron Collider (LHC), one can infer the existence of new particles. These new particles might give extra degrees of freedom and, complementing the SM, would allow to explain other processes.

This work constitutes a search for physics beyond the SM in $K_S^0 \to \mu^+\mu^-$ decays, and the development of reconstruction techniques and trigger configurations to study strange decays in the LHCb experiment.

In the first place, an overview to the theory of particle physics is presented. The SM is explained, together with new theoretical proposals, and its relation with strange decays. A description of the LHCb detector follows the previous chapter, emphasizing the features that make this unique detector able to study strange decays. Afterwards, the search for the $K_S^0 \to \mu^+\mu^-$ decay at LHCb is presented, whose result constitutes up to date, the most stringent limit on the branching fraction of this mode. To finalize, the upgrade of the LHCb detector is discussed, and a work on new reconstruction techniques for muons in this environment is presented. These results are complemented with preliminary trigger studies for some strange decays of interest, including $K_S^0 \to \mu^+\mu^-$.

Limiar

O Modelo Estándar (SM) é, hoxe en día, un modelo robusto que describe con gran precisión as interaccións entre partículas elementais. Non obstante, certos procesos, como a observación de oscilacións de neutrinos ou a presencia de materia escura no universo, constitúen indicios de física que non pode ser explicada con este modelo. O experimento LHCb, situado no CERN, ten como obxectivo mellorar a interpretación actual da física de partículas e comprender o funcionamento do universo. Mediante o estudo de desintegracións de certas partículas producidas no LHC, resulta posible inferir a existencia doutras novas. Estas novas partículas proporcionan graos de liberdade extra e, complementando o SM, permitirían explicar outros procesos.

Este traballo constitúe a busca de física máis aló do SM en desintegracións $K^0_S \to \mu^+\mu^-$, e o desenvolvemento de técnicas de reconstrución e configuracións do sistema de disparo para estudar desintegracións con estrañeza no experimento LHCb.

En primeiro lugar preséntase un resumo teórico sobre física de partículas. Este inclúe unha explicación do SM xunto con novas propostas teóricas, e a súa relación coas desintegracións con estrañeza. A este capítulo séguelle unha descrición do LHCb, onde se destacan aquelas características que fan que se poidan realizar estudos de desintegracións con estrañeza con este detector. A continuación amósase a busca da desintegración $K^0_S \to \mu^+\mu^-$ no detector LHCb, cuxo límite no cociente de ramificación é o máis baixo hoxe en día. Para rematar, amósanse as modificacións levadas a cabo na actualización do detector LHCb. A maiores inclúese un traballo sobre novas técnicas de reconstrución de muóns, xunto con resultados preliminares sobre o rendemento do sistema de disparo para desintegracións con estrañeza de interese, incluíndo $K^0_S \to \mu^+\mu^-$.

Resumen

El Modelo Estándar (SM) es, hoy en día, un modelo robusto que describe con gran precisión las interacciones entre partículas elementales. No obstante, ciertos procesos, como la observación de oscilaciones de neutrinos o la presencia de materia oscura en el universo, constituyen indicios de física que no puede ser explicada con este modelo. El experimento LHCb, ubicado en el CERN, tiene como objetivo esclarecer el panorama actual de la física de partículas y comprender las leyes que rigen el universo. Mediante el estudio de las desintegraciones de ciertas partículas producidas en el LHC, resulta posible inferir la existencia de otras nuevas. Estas nuevas partículas proporcionan grados de libertad extra y, complementando el SM, permitirían explicar otros procesos.

Este trabajo constituye la búsqueda de física más allá del SM en desintegraciones $K^0_S \to \mu^+\mu^-$, y el desarrollo de técnicas de reconstrucción y configuraciones del sistema de disparo para estudiar desintegraciones con extrañeza en el experimento LHCb.

En primer lugar se muestra un resumen teórico sobre física de partículas. Éste incluye una explicación del SM junto con nuevas propuestas teóricas, y su relación con las desintegraciones con extrañeza. A este capítulo le sigue una descripción del LHCb, donde se hace hincapié en aquellos rasgos que hacen que se puedan realizar estudios de desintegraciones con extrañeza con este detector. A continuación se muestra la búsqueda de la desintegración $K^0_S \to \mu^+\mu^-$ en el detector LHCb, cuyo límite en el cociente de ramificación es el más bajo hoy en día. Para finalizar se muestran las modificaciones llevadas a cabo en la actualización del detector LHCb. A mayores se incluye un trabajo sobre nuevas técnicas de reconstrucción de muones, junto con resultados preliminares sobre el rendimiento del sistema de disparo para desintegraciones con extrañeza de interés, incluyendo $K^0_S \to \mu^+\mu^-$.

Index

1

Overview of particle physics

The biggest improvements towards the understanding of fundamental interactions started to appear in the 1940s and 1950s. The introduction of renormalized Quantum Electrodynamics (QED), developed by Richard Feynman, together with the contributions from Yukawa, Yang and Mills to explain the nature of the strong interactions, probably constitute the most remarkable antecedents of the modern quantum field theories. Both QED and the weak interaction were later unified, followed by the inclusion of spontaneous symmetry breaking, which generates the necessary mass terms to explain the origin of the mass of the particles. In half a century, the knowledge about the nature of fundamental interactions drastically increased. The big developments done on the experimental side, with access to increasingly higher energies, allowed to test the new incoming theories and discover new processes and particles, needed to be understood from the theoretical point of view.

1.1 The Standard Model of Particle Physics

Developed in the early 1970s, the Standard Model (SM) [1, 2] is a well-tested Quantum Field Theory (QFT) that explains most of the processes observed in particle physics. The model is comprised by two different groups of particles, depending on their spin. Those with integer spin are called *bosons*, whilst those with half-integer spin are called *fermions*. The latter is subdivided into *quarks*, which can interact through the electroweak and strong forces; and *leptons*, only affected by the electroweak interactions. Fermions are divided into three different families, each composed by a weak isospin doublet. Charged leptons, like the e^-, μ^- and τ^- have negative weak isospin $-1/2$, whilst the corresponding neutral leptons ν_e, ν_μ and ν_τ, called *neutrinos*, have it positive $+1/2$. In the quark sector a similar structure is observed between u, c and t, with respect to d, s and b quarks. In addition, quarks have a charge called *color*, which is intrinsically related to the strong force. The color can be either red, blue or green, defined by the $SU(3)$ nature of Quantum Chromodynamics (QCD). By flipping the sign of all the charges of the particles, a process ruled by the C operator, one gets the antimatter sector, which also exists in nature. Transformation of particles to antiparticles is done through the C operator, in such a way that antiparticles are said to be the C-conjugated partners of particles and vice versa. An

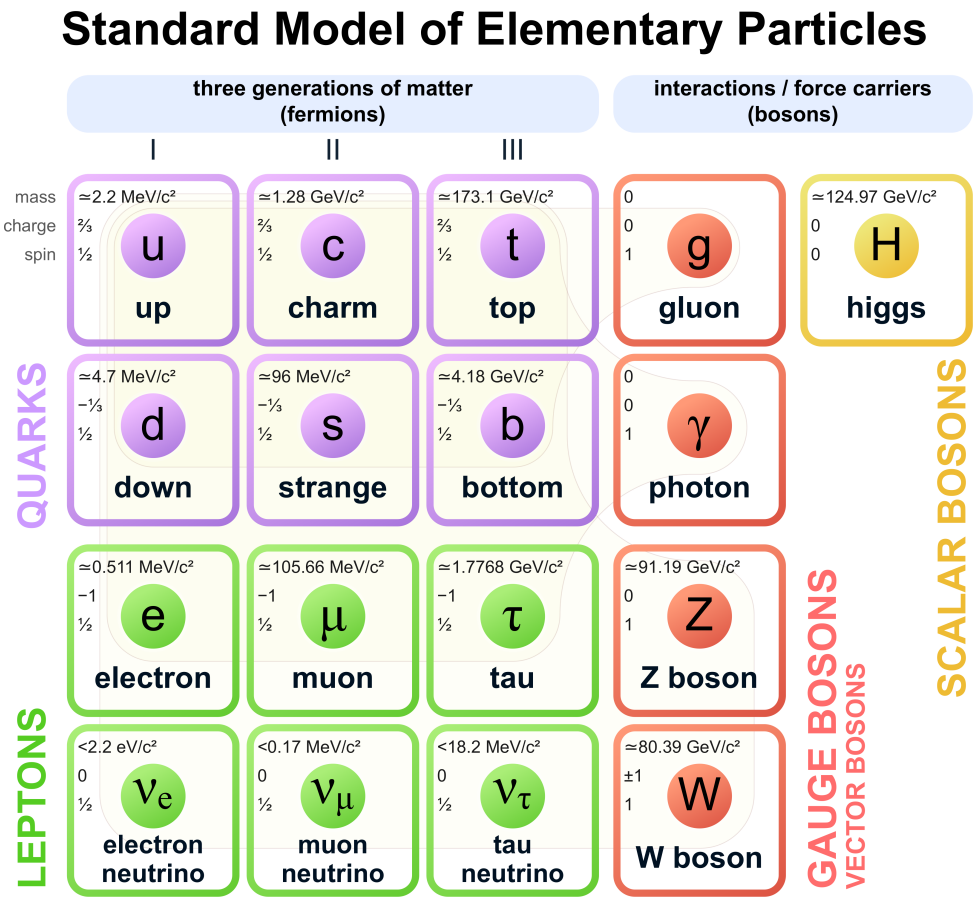

Figure 1.1: Scheme of the Standard Model of elementary particles. A replica of the fermion sector, but with opposite charges also exists, corresponding to the antimatter particles. Figure extracted from Ref. [3].

electron has the positron as its antiparticle, with the same mass and opposite electric and weak isospin charges. Similarly, the C-conjugated partner of the u is the $\bar{u}$, with opposite electric, weak isospin and color charges. A summary of the SM can be seen in Fig. 1.1.

Color confinement, a phenomenon explained by QCD, groups quarks together into hadrons, composed by quarks and/or anti-quarks. It also imposes that the combination of quarks and anti-quarks must have a global color charge equal to zero. This means that hadrons composed by two particles, called mesons, must contain a quark and anti-quark. If composed by three quarks, forming baryons, then it must contain either three quarks or three anti-quarks of different colors. Quarks and anti-quarks can also group together into more complex objects composed by four (tetraquarks) or five quarks (pentaquarks). In these cases, hadrons can have an asymmetric number of quarks and anti-quarks.

The $W^{\pm}$ and Z^0 the bosons act as mediators of the electroweak interaction, and gluons of the strong interaction. The Higgs boson is responsible for the mass of the particles, and is explained as a consequence of the electroweak symmetry breaking in the SM.

Transitions among the three families of quarks are ruled by the Cabibbo-Kobayashi-Maskawa (CKM) matrix. This unitary matrix of nine elements, defined in Eq. 1.1, gives

an idea of the coupling strength among the different flavors of quarks.

$$\begin{bmatrix} |V_{ud}| & |V_{us}| & |V_{ub}| \\ |V_{cd}| & |V_{cs}| & |V_{cb}| \\ |V_{td}| & |V_{ts}| & |V_{tb}| \end{bmatrix} = \begin{bmatrix} 0.9743 & 0.2253 & 0.0035 \\ 0.2252 & 0.9734 & 0.0412 \\ 0.0087 & 0.0404 & 0.9991 \end{bmatrix} \tag{1.1}$$

Transitions between quarks with the same weak isospin value must always proceed through an intermediate quark of opposite weak isospin value. Quarks belonging to the same family have a higher coupling, reflected in the diagonal of the matrix, whilst elements off-diagonal, corresponding to transitions among different families, are smaller. In the SM, the different behavior between matter and antimatter is determined by the combination of the charge-conjugation C and parity[1] P operators, leading to the CP transformation. If CP was a symmetry in the SM, then matter and antimatter would behave the same way. However, this symmetry is broken, and differences in the transitions between matter and antimatter particles are ruled by a single complex phase, responsible for all the CP-violating processes. The amount of CP-violation originated from it is not enough to explain the observed asymmetry between matter and antimatter in the universe, which is one of the conditions required for baryogenesis to happen [4]. From the conditions of unitarity of the CKM matrix, the inclusion of a fourth doublet of quarks would allow the SM to have two additional CP-violating phases, since its number depends on the size of the matrix N, as

$$\frac{(N-1)(N-2)}{2}. \tag{1.2}$$

However, including a new single doublet of fermions would break the $SU(2)$ gauge invariance [5]. In order to maintain the symmetry, the number of newly included fermion doublets must be even. The existence of additional families of light leptons was ruled out by studies of the Z^0 boson at the Large Electron-Positron collider (LEP) [6]. If a fourth family of quarks existed, their masses would be greater than that of the t quark, and would drastically increase the Higgs production cross-section through gluon-gluon fusion[2], which is in considerable tension with the observed Higgs signal at the LHC. The inclusion of doublets with chiral fermions (involving massless particles) is currently excluded by more than five standard deviations [7]. The presence of a new couple of fermion doublets is, in conclusion, very unlikely to happen, although it would still be possible in more complex extensions of the SM. The phase of the CKM matrix is currently the only known source of CP-violation in the SM, and the unbalance of matter and antimatter in the universe remains one of the biggest open questions in physics.

It is important to note that the particles described in Fig. 1.1 correspond to flavor eigenstates. They define states to be considered in the interactions. However, the physical states are those arising from the diagonalization of the Hamiltonian, which are mass eigenstates. By convention, the interaction eigenstates are chosen to be equal to the mass eigenstates for up-type quarks, whilst for down-type quarks they are rotated according to

[1] The parity transformation is the inversion of the spacial coordinates.

[2] This is the main source of Higgs production at the Large Hadron Collider (LHC).

Table 1.1: Relation among the strength of the four fundamental forces, normalized to that of the electromagnetic interaction, for two different scales. The gravitational strength is predicted to be several orders of magnitude below the other three, leading to a situation known as the hierarchy problem.

Scale	**Gravity (predicted)**	**Weak**	**Electromagnetic**	**Strong**
quark	10^{-41}	10^{-4}	1	60
protons/neutrons	10^{-36}	10^{-7}	1	20

the CKM matrix.

$$\begin{aligned} u_i^I &= u_j \\ d_i^I &= V_{\mathrm{CKM}} d_j \end{aligned} \tag{1.3}$$

where u_i^I and d_i^I denote the flavor eigenstates, and the mass eigenstates are defined by u_j and d_j. This means that each mass eigenstate for each down-type quark is a combination of the three different down-type flavors, in different proportions for each of them.

Besides the problem with the asymmetry between matter and antimatter in the universe, and far from being complete, the SM is unable to explain many other processes that have been observed. During its construction, it was realized that the SM was not able to explain the neutrino oscillations [8, 9]. The observation of transitions between different lepton flavors in the neutrino sector implies that they have mass. In the SM, neutrinos must have zero mass, traveling at the speed of light, which is in disagreement with the measurements.

The inclusion of gravity in the SM remains another open issue. Gravity is a very weak interaction that can be studied if large quantities of matter are present. Any attempt of studying particle-to-particle gravitational interactions of the known fundamental particles would fail, since the other forces would dominate over it by many orders of magnitude, as can be appreciated in Table 1.1. The difference in strength between the weak, strong and electromagnetic forces with respect to gravity can not be easily explained from a fundamental point of view. This is also known as the *hierarchy problem*. In addition, there are several theoretical issues that arise when trying to quantify gravitational interactions, since it leads to a non-renormalizable model [10, 11].

One of the most puzzling questions in particle physics is the strong CP problem. In the SM there is an additional term arising from QCD that contributes to the Lagrangian, and ruled by a phase θ, allows the strong interactions to violate the CP symmetry. This leads to an enormous neutron electric dipole moment, in contradiction with the most precise measurement of this quantity [12] unless $\theta < 10^{-9}$. From the theoretical perspective there is no reason for θ to be so small. Due to the large difference of CP violation in strong and weak interactions, it can be seen as an additional hierarchy problem of the SM.

Another existing issue concerns the existence of *dark matter* and *dark energy* in the universe, as reported by several astronomic observations [13]. The rotation of astronomical objects in the galaxies and the distribution of matter in their collisions suggest the presence of objects interacting with regular matter gravitationally. These objects would weakly interact, if they do, with regular matter via the interactions currently included

in the SM. Nowadays there is no evidence of the composition of the dark matter, and more investigations are needed in order to deeply understand its connection with the SM particles.

1.2 Beyond the Standard Model

In order to explain the processes not covered by the SM, discussed in the previous section, one needs to assume the existence of new particles. This provides new degrees of freedom to the model, allowing to cover the new phenomena.

During the construction of the LHC, one of the main bets was the existence of Supersymmetry (SUSY) [14]. In SUSY models, there is a link between each particle from Fig. 1.1 and a related superpartner. Particles that are fermions in the SM have an associated boson in SUSY, and each boson in the SM has an associated fermion in SUSY. Models based in SUSY can explain many of the problems described in Sect. 1.1. One of their strongest points is that many of the present issues are solved on a *natural* way, that is, without needing to fine-tune the SM parameters. The hierarchy problem and the unification of the gauge couplings at high energy are examples of it. In addition, under certain conditions [15] the theory accommodates gravity on a natural way, providing a massless particle of spin 2, the graviton. SUSY can also provide dark matter candidates, since there is no restriction on how particles and superpartners interact with each other. From astrophysical and cosmological constraints [16–18], such objects would typically need to have a large mass and interact weakly with regular matter, almost only gravitationally. On the other hand, some particles are expected also in the non-supersymmetric sector. Even the most simple SUSY model that can be realized consistently with the current results, the Minimal Supersymmetric Standard Model (MSSM), predicts the existence of more than one SM-like Higgs boson that has not been observed yet. Current experimental results keep constraining the possible masses and couplings of the supersymmetric particles, with no clear indication that a SUSY-based model will replace the current SM, pushing theoreticians to find other alternatives.

There are many other ways of introducing new particles and increase the degrees of freedom of the SM. One could accommodate, for example, the existence of another Higgs boson without needing to introduce SUSY [19]. This could provide new flavor-changing currents that could explain the neutrino masses. The inclusion of other particles like Z′ bosons can be done [20], providing a possible flavor-changing neutral current that could even break lepton-flavor universality. A possible dark matter candidate that would solve the strong CP problem is the Axion [21], which can be detected in the interaction of photons with strong magnetic fields [22, 23]. Vector-like quarks [24], which arise from many extensions of the SM, are usually motivated as a solution to the hierarchy problem. Nowadays, one of the strongest assumptions that can rule out many of the issues not solved by the SM consider the inclusion of leptoquarks [25, 26]. These particles would interact as quarks or leptons, allowing for lepton and baryon number violation. There are several limitations for leptoquarks, since there are strong experimental constraints on certain processes where they can be involved. For example, one of the strongest limits in the lifetime of particles corresponds to the proton decay. Considering leptoquarks, one could imagine a process where a proton decays into a pion and a positron, like that from Fig. 1.2. Current bounds on the proton decay [27] reveal that this is very unlikely

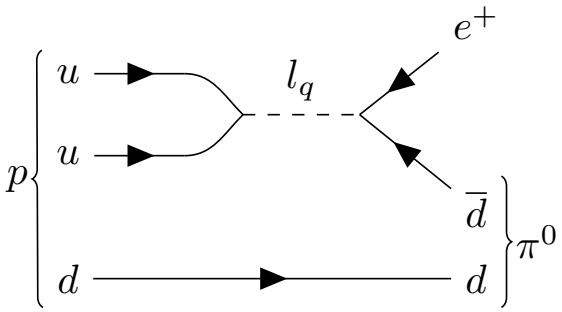

Figure 1.2: Example of a tree-level decay of a proton involving a leptoquark. Processes like this must be highly suppressed, since the current lower bound for the lifetime of the proton is around 10^{34} years [27].

to happen, which puts constraints on the masses of the leptoquarks and their spins so they can not proceed through a tree-level decay. However, models including leptoquarks have the power to explain baryogenesis and lepton flavor violation, and can accommodate the currently observed flavor anomalies [28, 29]. They have also a big impact in many other rare decays, since contributions at the loop level can enhance or suppress certain processes.

1.3 Strange decays

Decays involving the quark s have been of great relevance in the past. Before the c, b and t were discovered, the Glashow-Iliopoulos-Maiani (GIM) mechanism was proposed to explain the suppression of flavor-changing neutral currents (FCNCs) in loop diagrams, like for $K^0_{\mathrm{L}} \to \mu^+\mu^-$ [30]. This mechanism needed the inclusion of a fourth quark, leading to the first prediction of the c quark. On the other hand, the discovery of CP violation in neutral kaon decays [31] suggested the presence of a third family of quarks, since it is the minimum amount required for the quark mixing matrix to have a CP violating phase. It is important to note that the third family of quarks was also postulated before the discovery of the c quark.

From Eq. 1.1, one can easily observe that, for second-order Feynman diagrams, transitions of the type $s \to d$ have the strongest suppression in the SM. This is of high relevance for the study of strange decays, since they can provide a high sensitivity to new particles in non-minimal flavor-violating scenarios [32, 33]. Currently, one of the golden channels in this field is the $K \to \pi\nu\bar{\nu}$ decay, where both the neutral and charged modes are considered. Experimentally, the charged mode $K^+ \to \pi^+\nu\bar{\nu}$ is the easiest to study, since one can reconstruct the decay vertex from the kaon and pion tracks. The NA62 experiment [34] has been built in order to study this decay, whose current sensitivity on the branching fraction is competitive with the theoretical predictions. Its measurement will have a big impact in the theoretical community. The neutral mode is more challenging since no vertex can be reconstructed for this decay. The observation of signal is only determined from the presence of a π^0, that will mainly decay to two photons. The design of efficient vetoes is crucial in this case, since in the reconstruction it becomes quite hard to distinguish, for example, between $K^0_{\mathrm{L}} \to \pi^0\pi^+\pi^-$ and $K^0_{\mathrm{L}} \to \pi^0\mu^+\mu^-$. Currently, there is only

one experiment studying the $K_L^0 \to \pi^0\nu\bar{\nu}$ decay, which is KOTO [35], located at J-PARC. A recent proposal for a similar experiment, named KLEVER, has also been made at the European Organization for Nuclear Research (CERN) [36].

Apart from the golden channels $K \to \pi\nu\bar{\nu}$, there are many interesting decays, already of relevance in the 70s, that were left behind due to the lack of experimental capabilities to do the measurements [37]. One example is the rare decays of strange particles, like $K_S^0 \to \mu^+\mu^-$, $\Sigma^+ \to p\mu^+\mu^-$ or $K_S^0 \to \pi^0\mu^+\mu^-$. These decays involve FNCNs through penguin diagrams, and are very suppressed in the SM. The $\Sigma^+ \to p\mu^+\mu^-$ decay has been of relevance due to the observation of three events in absence of background by the HyperCP experiment, sharing the same dimuon invariant mass, pointing towards the existence of an intermediate neutral particle. Such hypothesis has been recently rejected by the LHCb collaboration [38]. On the other hand, $K_S^0 \to \pi^0\mu^+\mu^-$ is of importance due to its implication in the SM prediction for $K_L^0 \to \pi^0\mu^+\mu^-$, whose branching fraction is enhanced by one order of magnitude in models with extra dimensions [39]. There is currently a proposal of improving the previous measurement from NA48 [40] at LHCb, using the currently existing data set [41]. The $K_S^0 \to \mu^+\mu^-$ decay, whose SM prediction for the branching fraction is $\mathcal{O}(10^{-12})$ [42–44], is of particular interest since it can be affected by new physics (NP) on a different way with respect to the K_L^0 mode. It has several implications in SUSY [42] and leptoquark [45] models. The connection among them will be explained in more detail in the next section.

Other decays of importance for the theoretical community are the semileptonic hyperon decays (SHDs). Hyperons are baryons that contain one or more s quarks, together with u and/or d quarks. Apart from helping to improve the knowledge on V_{us} and V_{ud}, they are sensitive to NP, in particular scalar and tensor contributions [46].

1.4 The $K_S^0 \to \mu^+\mu^-$ decay

This decay is of particular interest due to its high suppression in the SM. The most precise SM prediction of its branching fraction is [42, 43, 47]

$$\mathcal{B}_{SM}(K_S^0 \to \mu^+\mu^-) = (5.18 \pm 1.50_{LD} \pm 0.02_{SD}) \times 10^{-12}, \tag{1.4}$$

where the two uncertainties with subscripts LD and SD relate to long- and short-distance effects, respectively. In the SM contributions to $\mathcal{B}(K_S^0 \to \mu^+\mu^-)$ and $\mathcal{B}(K_L^0 \to \mu^+\mu^-)$ differ, since CP-violating effects enter differently in each branching fraction. Both of them are dominated by long-distance effects through a $K^0 \to \gamma^*\gamma^*$ transition, whose diagram is shown in Fig. 1.3a. There are additional short-distance components ruled by diagrams like that of Fig. 1.3b.

In general, the branching fraction of both the $K_S^0 \to \mu^+\mu^-$ and $K_L^0 \to \mu^+\mu^-$ decays can be expressed as:

$$\mathcal{B}(K_{S/L}^0 \to \mu^+\mu^-) \propto \frac{m_K \beta_\mu}{8\pi}\left(|A|^2 + \beta_\mu^2 |B|^2\right), \quad \beta_\mu = \sqrt{1 - \frac{4m_\mu^2}{m_K^2}} \tag{1.5}$$

where A and B describe the s-wave and p-wave components, respectively. The two amplitudes computed from A and B have opposite CP, in such a way that the CP-conserving

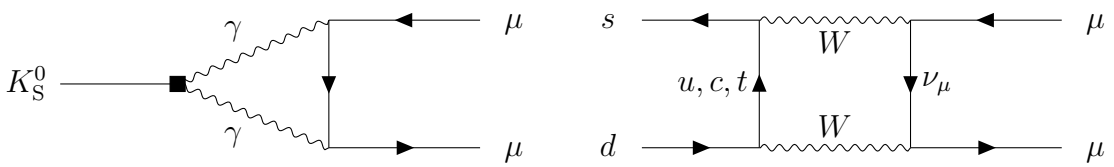

(a) Long-distance

(b) Short-distance

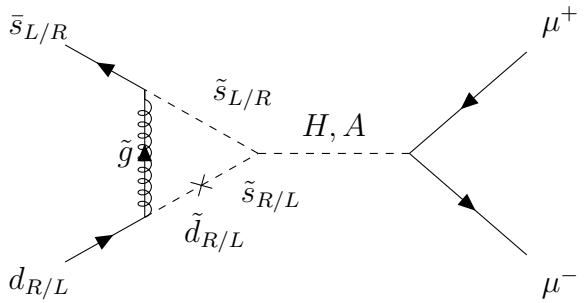

(c) Dominant MSSM contribution [42]

Figure 1.3: Examples of Feynman diagrams for the $K_S^0 \to \mu^+\mu^-$ decay. Long-distance effects dominate the decay, although the short-distance component can not be neglected. The top-right figure constitutes only an example of a short-distance contribution.

contribution for K_L^0 is given by A, whilst for K_S^0 it is given by B. The process $K_{S/L} \to \gamma^*\gamma^*$ contributes to both amplitudes, but always with a negligible CP-violating contribution. On the other hand, short-distance effects can only affect the A term. These are the reasons why for $K_L^0 \to \mu^+\mu^-$ one can neglect the B term in Eq. 1.5, and write

$$\mathcal{B}(K_L^0 \to \mu^+\mu^-) \propto \frac{m_K \beta_\mu}{8\pi} |A|^2 = \frac{m_K \beta_\mu}{8\pi} |A_{L,\gamma\gamma} + A_{\text{short}}|^2 . \tag{1.6}$$

However, for the K_S^0 mode things are different. Since the long-distance contribution to A is CP-violating it becomes negligible, so the short-distance contributions dominate. In this case both terms must be kept, and the branching fraction becomes

$$\mathcal{B}(K_S^0 \to \mu^+\mu^-) \propto \frac{m_K \beta_\mu}{8\pi} \left(|A_{\text{short}}|^2 + \beta_\mu^2 |B_{S,\gamma\gamma}|^2 \right) . \tag{1.7}$$

It is important to note that in Eq. 1.5, contributions add incoherently to the total rate. This makes easier to derive constraints on the short-distance components from the experimental measurement of $K_S^0 \to \mu^+\mu^-$ rather than from $K_L^0 \to \mu^+\mu^-$.

A measurement on the branching fraction of $K_S^0 \to \mu^+\mu^-$ around 10^{-11} would allow to set interesting bounds to the $s \to d\ell^+\ell^-$ transition. These bounds would help to discriminate among different NP scenarios in case other modes, like $K \to \pi\nu\bar{\nu}$, indicate an enhancement of the $s \to d\ell^+\ell^-$ amplitude [43].

Very interesting results can also be obtained by studying the interference between K_L^0 and K_S^0 modes [48]. The sign of the amplitude $A_{L,\gamma\gamma}$ is still unknown, and leads to two

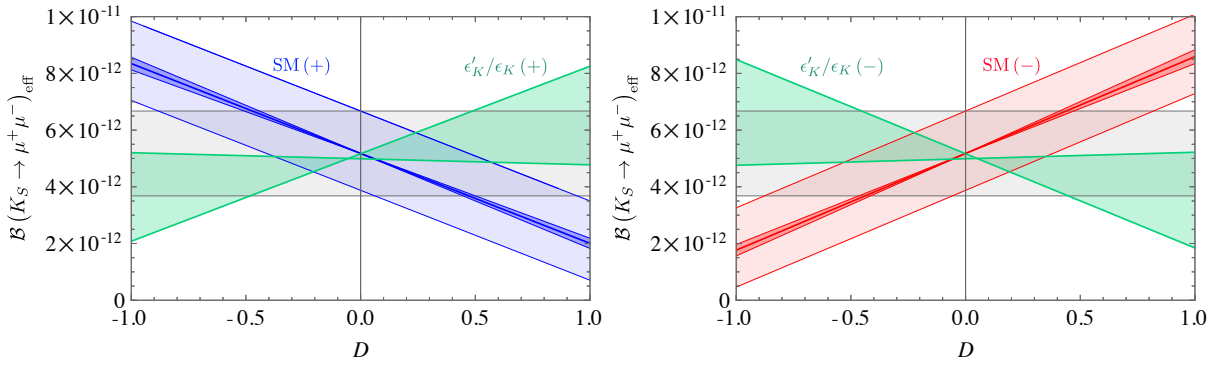

(a) (b)

Figure 1.4: Evolution of the $K^0_S \to \mu^+\mu^-$ effective branching fraction as a function of the dilution factor in Eq. 1.9. Left and right panels correspond to the positive and negative signs of $A_{L,\gamma\gamma}$, respectively. The blue and red lines correspond to the SM prediction for $\mathcal{B}(K^0_S \to \mu^+\mu^-)$, where the darker bands correspond to the uncertainty from the interference and the lighter to that of $A_{S,\gamma\gamma}$. The possible ε'/ε anomaly [50–55] can be explained, within a Z′ model, in the green regions. The value of $\mathcal{B}(K^0_S \to \mu^+\mu^-)$ from Eq. 1.4 is displayed in gray. Figure taken from Ref. [48].

different SM predictions for the $K^0_L \to \mu^+\mu^-$ decay [49]:

$$\begin{aligned} \mathcal{B}_{\rm SM}(K^0_L \to \mu^+\mu^-) &= (6.85 \pm 0.80 \pm 0.06) \times 10^{-9} \quad \text{if } A_{L,\gamma\gamma} > 0 \\ \mathcal{B}_{\rm SM}(K^0_L \to \mu^+\mu^-) &= (8.11 \pm 1.49 \pm 0.13) \times 10^{-9} \quad \text{if } A_{L,\gamma\gamma} < 0 \end{aligned} \tag{1.8}$$

A study of the interference between the K^0_S and K^0_L modes would allow to determine this sign and reduce the uncertainty on the SM prediction for $K^0_L \to \mu^+\mu^-$ so it reaches the current experimental levels $\mathcal{B}_{\rm exp}(K^0_L \to \mu^+\mu^-) = (6.84 \pm 0.11) \times 10^{-9}$ [47]. The study of the interference also serves to validate the SM due to its relation with the value of the CP-violation ratio ε'/ε [45], as can be seen in Fig. 1.4. Looking at the evolution of the branching fraction as a function of the dilution factor D, defined as the asymmetry of the number of K^0 and $\bar{K}^0$ in the production

$$D = \frac{K^0 - \bar{K}^0}{K^0 + \bar{K}^0}, \tag{1.9}$$

the allowed regions change depending on the sign of $A_{L,\gamma\gamma}$. At LHCb, the dilution factor in proton-proton collisions is expected to be negligible, loosing the sensitivity to the sign of this amplitude. However, K^0–$\bar{K}^0$ asymmetry can be generated at LHCb using different methods. The first consists on determining the flavor of the neutral kaon by looking to its companion K^-, a method known as *tagging*. Around 30% of the prompt K^0 are produced together with a K^-, and the latter can be identified using the RICH detectors. A similar tagging can be done using Λ baryons, where they would be reconstructed as $\Lambda \to p\pi^-$. Another proposal is the utilization of pion tagging, using $K^{*+} \to K^0\pi^+X$ decays.

Contributions from new particles could affect exclusively the $K^0_S \to \mu^+\mu^-$ mode and not $K^0_L \to \mu^+\mu^-$. In left-handed or right-handed NP scenarios, the two branching fractions behave on a different way. There have been recently shown interesting implications

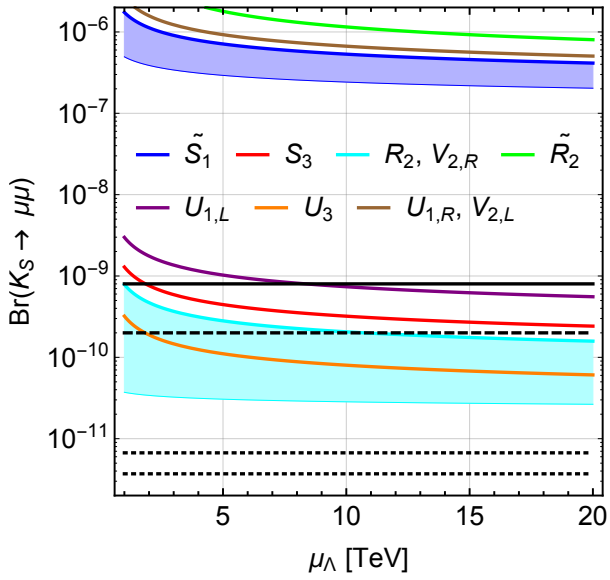

Figure 1.5: Relation of $\mathcal{B}(K_S^0 \to \mu^+\mu^-)$ with the NP scale μ_Λ, which in this case is assumed to be of the order of the leptoquark mass. Values for different leptoquark models are shown in colored solid lines. The last limit from LHCb [56], prior to this work, is marked in solid black. In dashed black a tentative expectation for LHCb in Run 2 is shown, and the SM prediction is shown in dotted black. The current limit is already excluding some leptoquark models, and the sensitivity to many others can be improved with Run 2 data. On the other hand, those involving U_3, R_2 and $V_{2,R}$ would only be reachable after the upgrade of the LHCb experiment. Figure taken from [45].

of the $K_S^0 \to \mu^+\mu^-$ measurement in SUSY models [42], where the current experimental bounds are already sensitive to certain regions of the parameter space. The $K_S^0 \to \mu^+\mu^-$ decay also helps to discriminate among other NP models, in particular those involving leptoquarks [45]. Improved limits would allow to put bounds to NP effects arising from this kind of models. The most precise measurement prior to that presented in this work [56] has already helped to constrain some of them, as can be seen in Fig. 1.5.

So far, it has been shown that the study of the $K_S^0 \to \mu^+\mu^-$ decay has the potential to constrain many new models, being complementary to other searches for strange decays. There is also an interesting connection with CP-violating quantities that serve to test the SM. It is expected that with data from the Run 2 of the LHCb experiment, whose analysis is reported in this work, together with that from its upgrades, will provide a unique opportunity to search for this very rare decay and shed light on the current interpretation of fundamental particle interactions.

2

The LHCb detector at the LHC

In 2000 the LEP accelerator, located at CERN, performed its final shutdown. During its operation, this electron-positron collider allowed to achieve many important milestones for the understanding of particle physics. The masses of the $W^{\pm}$ and Z^0 bosons were measured with a precision of one per mille [57]. Using decays of Z^0 bosons, the number of light lepton families was determined to be three in an indirect way [6]. Many other constraints on new physics could also be done, and it was suggested that, in case of running for one more year, the Higgs boson could have been discovered already using this accelerator [58].

Historically, the construction of lepton and hadron colliders for particle physics usually alternates. New particles are searched for using hadron colliders, since the energy involved in the collisions has a much wider range. Once a new particle is discovered, typically a lepton collider is built, in such a way that collisions are tuned to create such particle, and do precision measurements of its properties. An example of this phenomenon is the study of the neutral currents, mediated by the Z^0 boson. It was postulated in 1958, by Sidney Bludman [59], but it was in 1973 when the first experimental evidence supporting this idea was presented by the Gargamelle collaboration [60] on studies of neutrino-electron elastic interactions. The Z^0 boson was later searched for, and discovered at the SPS, operating as a proton-antiproton collider [61,62]. However, its properties were studied at LEP, were a much larger sample of bosons could be produced [6].

A similar story repeats for the LHC. Before its construction, the existence of the Higgs boson as a particle arising from a spontaneous-symmetry-breaking mechanism was very clear. Almost any model attempting to explain the origin of the mass within the SM included at least one Higgs boson. There were also big expectations on searches for NP at the TeV scale, which was theoretically favored at the time. SUSY scenarios were the most elegant solutions for many of the issues unresolved by the SM, and it was thought that many SUSY particles could be visible at the LHC. There was also a need to perform studies about the behavior of matter at high energies. In particular, the QCD behavior at high energies was completely unknown, and having a hadron collider operating at the TeV scale constitutes an ideal environment to do such studies. On the other hand, the uncertainties in the CKM parameters were very large, in particular those involving the c, b and t quarks. The huge production of b and c hadrons in proton-proton collisions would allow to improve the precision on these quantities. The LHC also opened the door

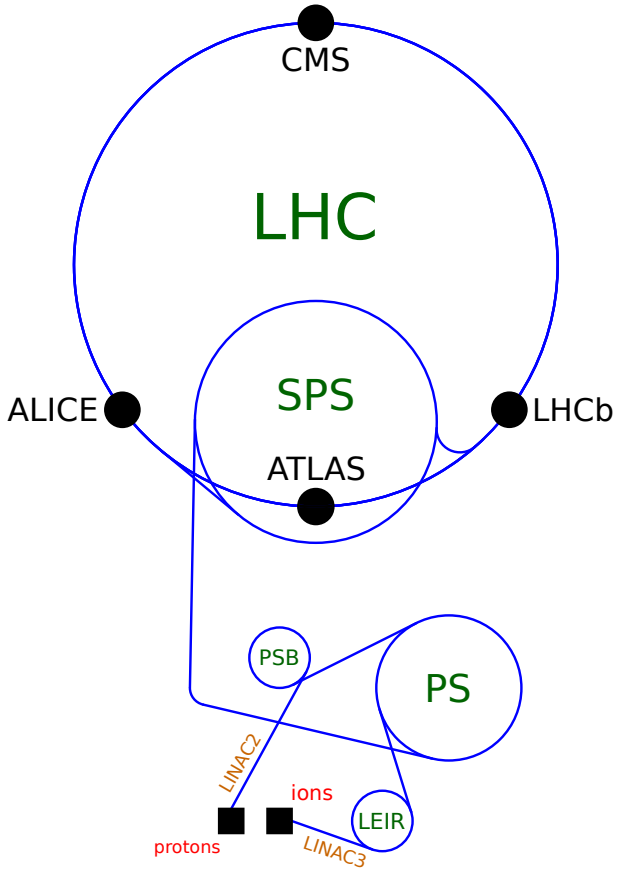

Figure 2.1: Scheme of the accelerators used to boost particles at the LHC. The starting point is different for protons and ions, but they later coincide at the PS. Collisions are done simultaneously at four points in the LHC ring, where the main detectors are located.

to do searches for CP-violation and spectroscopy studies. Quantities like ϕ_s, the CP-violating phase of B_s^0 hadrons, typically studied in $B_s^0 \to J/\psi\phi$ decays, were probed to be very sensitive to NP effects. Interesting results could be achieved, competing with the B Factories [63, 64]. Indirect searches for NP could also become possible in very rare decays, like $B_s^0 \to \mu^+\mu^-$, that could provide evidence for new particles with masses greater than the operation energy of the LHC.

2.1 The Large Hadron Collider

Located at CERN, the LHC is a proton-proton collider, which started its operation in 2008. It is constituted by 27 km of superconducting magnets and accelerators to boost the energy of protons to an energy of ∼6.5 TeV. Protons travel in two independent beam pipes in opposite directions. The direction of the magnetic fields are also opposite for the two beams. Protons collide in four main detectors located along the ring: ATLAS [65], CMS [66], ALICE [67] and LHCb [68]. In order to shield them from cosmic rays, the accelerator is located on average 100 m underground. The tunnel holding it is the same that was used for the LEP accelerator.

A simplified scheme of the accelerators involved in the LHC operation together with the

four main detectors can be seen in Fig. 2.1. The process of accelerating protons starts on a bottle of hydrogen. Protons are extracted from the gas using a Duoplasmatron. A strong electrical field breaks the hydrogen molecules H_2 into its basic constituents via electron-induced reactions. Protons are then accelerated using grids with a potential difference of 100 kV. At this stage protons travel at 1.4% of the speed of light, that is ∼4000 km/s. The beam is then focused and accelerated using a radio-frequency quadrupole, which also divides it in bunches, and enters into the first accelerator, the LINAC2. The LINAC2 accelerator is the only linear accelerator in the path of the protons to the LHC. It consists on a multi-chamber resonant cavity tuned to an specific frequency which creates potential differences in different sub-cavities, accelerating the protons to 50 MeV. They enter then into the first circular accelerator, the Proton Synchrotron Booster (PSB)[1]. This four-rings accelerator boosts the protons to an energy of 1.4 GeV and focuses again the beam, improving its quality. The accelerated particles are then introduced into the Proton Synchrotron (PS). The PS is the accelerator responsible for providing 81 bunches with 25 ns spacing between them, the configuration at which LHC operates. It also accelerates protons to 25 GeV, before being injected to the Super Proton Synchrotron (SPS). The SPS is the final accelerator before the LHC. It also provides protons to many other experiments, like NA62 or CNGS, as well as for detector and accelerator studies in test-beam facilities. When they leave the SPS, protons have been boosted to an energy of 450 GeV, and are transferred to the LHC both in clockwise and anti-clockwise directions. The filling of the LHC plus the ramp-up in energy to reach the nominal energy of $[7, 8, 13]$ TeV takes approximately 45 minutes.

Beams are then squeezed so the size of the bunches decreases. This is important since protons could otherwise deviate in the cavities and damage certain detectors and devices along the beam by directly colliding with them at high energy. Any big deviation in the beam trajectory or focusing detected while the LHC is functioning leads to a beam-dump. A beam-dump can be produced automatically by the LHC controlling system or manually. In any case, protons are rapidly extracted from the LHC and are made to collide with dedicated absorbers surrounded by big blocks of concrete and iron. After this, the LHC needs to be refilled.

In nominal conditions, the LHC has been operating mainly at energies of $[7, 8, 13]$ TeV, with bunches separated by 25 ns. Protons are made to collide in the four detectors mentioned above. Beams are tuned right before each colliding point to adapt them to the necessities of each experiment. This process barely affects the functioning of the other detectors. Not all the protons are consumed in each bunch-bunch collision. Only a few of them collide, and the remaining continue orbiting the LHC, producing new collisions. The intensities of the beams decrease with time, till it reaches a point where the amount of protons per bunch is very small, leading to a small number of collisions. In this situation, beams are dumped and the LHC is filled again. Typically, the LHC is filled at least two times per day.

During the construction of the LHC, the ALICE detector was meant to study also proton-ion and ion-ion collisions at high energies. This forced the accelerators to accommodate to this new necessity. The path of the ions through the acceleration system is

[1]For the Run-III of the LHC, the LINAC2 will be replaced by the LINAC4. This new device will also improve the acceleration of different types of heavy-ions. Particles will be boosted to an energy of 160 MeV.

very similar to that of the protons. Due to the interest on studying highly-condensed matter, the most interesting ion to use is $^{208}_{82}$Pb given its nuclear properties. The isolation of atoms of this element starts with a pure sample of solid $^{208}_{82}$Pb. This sample is heated to become a vapor. These atoms are then ionized, becoming a plasma, and accelerated through a potential difference in a different linear accelerator, the LINAC3, and then in LEIR, which is the first circular collider in this specific process. Ions are then injected to the PS and follow the same path as the protons. Due to the characteristics of the SPS, ions can be injected either clock-wise or anti-clockwise. This is of particular interest for experiments like ALICE and LHCb, which are not symmetric with respect to the beam.

Up to now, the LHC constitutes the biggest accelerator ever built. A long and fruitful future is foreseen for this device, which is expected to operate till 2030s. A wide physics program, provided by the unique opportunity to test processes at very high energy well under experimental control, makes it the main meeting point for most of the particle physics community. The LHC will allow to perform many searches for NP and, if not found, put bounds on many existing models, as well as to clarify the picture we currently have about fundamental physics.

2.2 The LHCb detector

The LHCb detector [69, 70] is a single-arm spectrometer operating at the LHC. It covers a pseudorapidity range of $2 < \eta < 5$. The main purpose of this experiment is to measure the properties of b and c hadron decays. The characteristics of this detector have been optimized for the detection of the decay products of these particles in proton-proton collisions at high-energies.

The LHCb detector strongly differs from other experiments focused on the same field of physics, like the B Factories [63,64], in many aspects. In these experiments, b hadrons are produced in electron-positron collisions with an energy tuned in the mass of the $\Upsilon(4S)$ meson, which mainly decays into two b-hadrons. This is a much cleaner environment compared to LHCb, since the energy involved in the collisions is known beforehand, allowing to apply kinematic constraints in the analyses. However, it limits the opportunity to search for new particles, at least on a direct way, since collisions must be done at a certain energy. At LHCb, the spectrum of particles produced is richer. Nowadays, it constitutes the only detector capable of producing and studying b-baryons, and B_s^0 hadrons are produced more efficiently than in the B Factories. In the LHCb experiment, there is also a high production of c hadrons, providing a unique environment to search for NP in the decays of this quark, and to search for CP-violation in up-type quarks. During its operation, the LHCb detector has proved to be have a big flexibility to increase its physics program [71–74]. Nowadays, it can be described as a general-purpose detector in the forward region, complementing the low-pseudorapidity range and momentum resolution of ATLAS and CMS [75–77]. Many interesting results have been achieved also in proton-ion collisions, cross-checking many results from the ALICE collaboration [78–80].

2.2.1 Geometry and subdetectors

The LHCb detector follows the typical layout of a high-energy detector, as can be seen in Fig. 2.2. A high-precision tracking system, the VELO, surrounds the collision point.

This subdetector is composed by silicon strips with different layers that alternately measure radial and angular positions. The tracking system is complemented by a silicon-microstrip subdetector, the Tracker Turicensis (TT), located before the magnet, and additional tracking stations situated after the magnet. The latter are composed by silicon-microstrip detectors in the region closer to the beam-pipe, constituting the Silicon Tracker (ST), and straw-tubes in the outer region, forming the Outer Tracker (OT). In an experiment focused to flavor-physics, it becomes strictly necessary to identify the flavor of the decay products. This is achieved in three different ways. Electrons and photons are identified using an electromagnetic calorimeter (ECAL). The information is complemented by using a Scintillator Pad Detector (SPD) and a Preshower (PS), separated by a lead wall. Both the SPD and PS allow to provide a reasonable precision and background control to identify π^0, photons and electrons. Hadrons are identified using two different RICH detectors (RICH1 and RICH2) located before and after the magnet. This allows to distinguish among pions, kaons and protons. A hadronic calorimeter (HCAL) is also present, providing additional information. Finally, muons are identified using five muon chambers, which alternate layers of iron and sensitive material. The latter is composed by Multi Wire Proportional Chambers for regions close to the beam-pipe, and Resistive Plate Chambers around them.

2.2.2 Muon identification

The correct identification of muons is crucial for a big part of the LHCb physics program, and it is of particular interest for the studies done in this work. Historically, two of the most important decays of study at LHCb: $B_s^0 \to \mu^+\mu^-$ and $B_s^0 \to J/\psi(\to \mu^+\mu^-)\phi$, involve muons in the final state. Many algorithms have been developed through the years thanks to the increase of knowledge about the behavior of particles in the muon chambers and the inclusion of better algorithms to understand the differences between muons and the rest of particles.

The identification of muons starts with the association of hits in the muon chambers to each track. This is done by linearly extrapolating the input tracks to the stations. A field of interest (FoI) is built around the extrapolated position that depends on the momentum of the tracks, the muon station and the region. Hits are searched for within the FoIs of different muon stations, depending on the momentum. The closest hits are taken, and only tracks with valid hits are furtherly processed by the next algorithms. The boolean variable resulting from this algorithm, called `IsMuon` in the LHCb jargon, constitutes the most basic kind of muon identification.

Once the tracks with valid associated hits are identified a muon probability can be calculated in order to gain further rejection. The average squared distance between the position of the extrapolations and the closest hit in each FoI can be used in order to distinguish muons from the rest of particles

$$d^2 = \frac{1}{N}\sum_{i=0}^{N}\left[\left(\frac{x_{\text{closest},i} - x_{\text{track},i}}{\text{pad}_{x,i}}\right)^2 + \left(\frac{y_{\text{closest},i} - y_{\text{track},i}}{\text{pad}_{y,i}}\right)^2\right]. \tag{2.1}$$

In the previous equation, i denotes the station, x and y refer to the positions and *pad* corresponds to the size of the pad in the muon station region. Studying the behavior

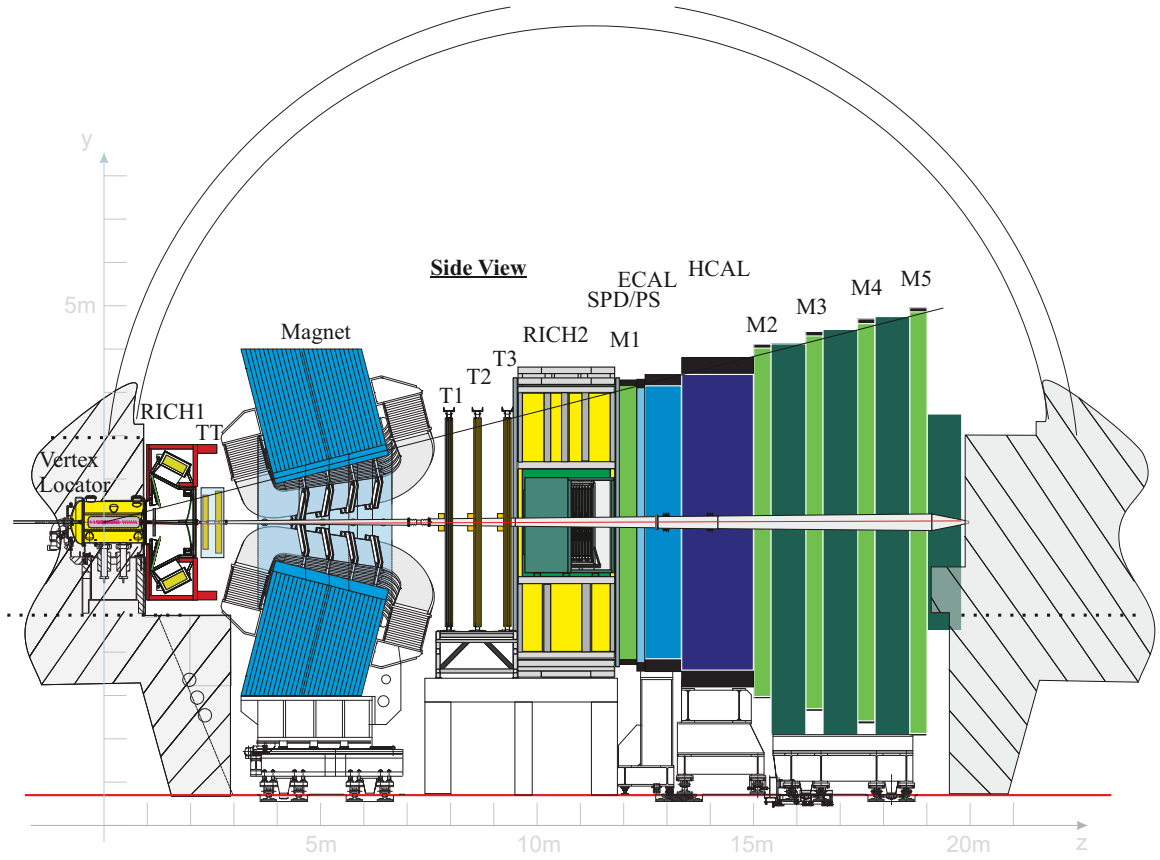

Figure 2.2: Cross-section of the LHCb detector [68].

of this quantity in different calibration samples (for muon and non-muon particles) it is possible to define a test statistic and use it in order to identify real muons

$$\texttt{DLL} = \log\left(\frac{P(\mu)}{P(\text{not } \mu)}\right) = \log\left[P(\mu)\right] - \log\left[P(\text{not } \mu)\right]. \tag{2.2}$$

A fit of the muon hits to a straight line is also done, and the resulting χ^2/ndof is kept. The information achieved with the previous algorithms can be combined with that of the other subdetectors in order to have a more complete understanding of the behavior of muons in the detector. Likelihoods from every subdetector can be added linearly in order to get a combined likelihood $\texttt{DLL}_{\text{comb}}$. This new variable gives a measure of how likely the mass hypothesis under consideration is, for any given track, relative to a certain hypothesis (in general a pion).

A more efficient particle identification is achieved with the usage of Neural Networks (NNs). This allows to account for the different correlation between subdetectors and include additional information. The goal is similar to that of the `DLL`, obtain a single magnitude (a probability) defining how likely a track is from being produced by a muon. These variables are called `ProbNN` at LHCb.

In Run 1 an additional algorithm was designed to identify low-p_T muons. This new algorithm allows to compute a variable using additional information from the muon stations and RICH subdetectors. The information from the variables described above is combined with the timing information and number of hits around the extrapolated track position to each muon station, a χ^2 computed from the muon hits positions and the track extrapolation points and other variables related to the tracking and response of the RICH and calorimeter detectors. This new variable, called `muonIDPlusBDT`, constitutes one of the major improvements to study strange decays at LHCb, and it has been used for analyses involving 2012 and Run 2 data. Unfortunately, the algorithm is too slow to run at the trigger level, and could only be used offline. More information about the muon identification at LHCb can be found in Refs. [81, 82].

2.2.3 The trigger system in Run 2

The LHCb detector worked at a frequency of 40 MHz for Run 2. This translates into having one event each 25 ns. The beams are tuned so that the average number of primary vertices (PVs) produced is 1.6. Every time the LHC is filled with protons, the data-taking is considered to be within a *fill*. Each fill is subdivided in *runs*, each of them with a possible different configuration. Differences between runs include changes in the Data Acquisition (DAQ), trigger system, calibration or alignment, among others. Discarding interruptions due to operation issues or configuration changes, runs were configured to last for one hour. The amount of integrated luminosity collected per year, together with the energy of the proton-proton collisions at the LHC can be seen in Table 2.1.

The trigger is the part of the detector responsible for doing an online selection of events of interest. In a proton-proton collider, many of the events correspond to peripheral collisions of protons, where the amount of energy involved is small, or simply to events where it is unlikely to find particles of interest. To avoid accumulating a large amount of data files with uninteresting events; and in order to reduce the throughput of the detector, that would drastically increase the computing costs of the detector; applying

Table 2.1: Luminosity collected by the LHCb detector together with the center-of-mass energy for different years of data-taking.

Year	2010	2011	2012	2015	2016	2017	2018
Integrated luminosity (fb^{-1})	0.04	1.11	2.08	0.33	1.67	1.71	2.19
Energy (TeV)	7	7	8	13	13	13	13

online selections to the events becomes completely necessary. The LHCb trigger [83] uses information from the event in order to determine whether there are decays of interest in it or not, and save the information accordingly. It has been designed and optimized for the main physics purpose of the experiment, the study of b and c hadron decays. However, its high flexibility has allowed to modify its internal structure and adapt it to the new necessities of the collaboration, increasing the physics range of the detector. It is composed by three levels, each of them being made of different selections (trigger lines) focused on different kinds of decays:

- **Level Zero Trigger (L0):** The first level of the LHCb trigger is implemented in hardware. Selections are applied directly to the output information from the sub-detectors doing a simple conversion to physical units. Due to the requirement of the LHC to run at 40 MHz only basic physical quantities are used, like the transverse momentum or transverse energy, calculated using the information from the calorimeters and muon detectors, with an averaged resolution of $\sim$25%. Additional requirements are set on the occupancy in the SPD, and the information from the PS is used to distinguish between photon and electron candidates. The rate of the data-taking is reduced at this stage from 40 MHz to 1 MHz.

- **High Level Trigger (HLT):** After the L0, the trigger is based in software, allowing for a high flexibility in the selections made in the subsequent stages. Given that for the Run 2 of the LHCb detector the alignment and calibration has been done online, the performance of the reconstruction at the HLT is very similar to that achieved offline, leading to more efficient selections.

    1. **HLT1 trigger:** The second level of the LHCb trigger reconstructs trajectories of charged particles traversing the full LHCb tracking system, called long tracks, and a precise reconstruction of the PV is performed. Selections are based on kinematical and topological information. No particle-identification is done at this stage, except for a very fast and simple muon identification, that will be discussed later. The output rate after running the selections of HLT1 is reduced to 110 kHz.
    2. **HLT2 trigger:** This is the last level of the LHCb trigger, and in Run 2 it ran asynchronously with respect to the data-taking. A 10 PB buffer is placed between HLT1 and HLT2, giving flexibility to the online system. This allows the HLT2 to be processed in inter-fill periods, and it allows to calibrate and align the detector run-by-run. Provided that the calibration and alignment of the detector is done before this stage, and the information from the RICH detectors is added, selections can be identical to those made offline. This level

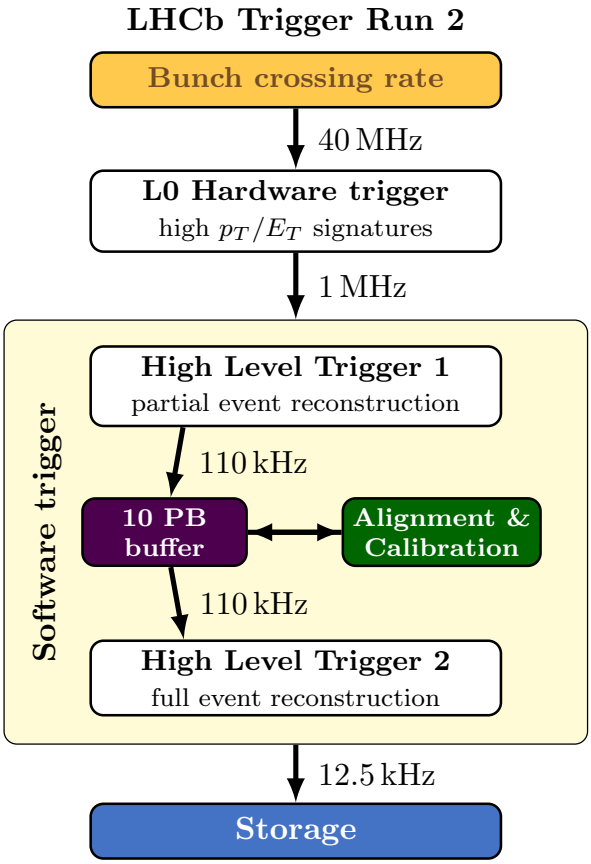

Figure 2.3: Overview of the LHCb trigger system in Run 2, as taken from Ref. [83].

sets the final rate of the LHCb trigger to 12.5 kHz, which translates in about 0.6 GB/s being written to disk.

An event is processed in the next level of the trigger system if it satisfies any of the selections present in the previous stage. Trigger lines can be either *inclusive*, that is, select particles following a certain topology; or *exclusive*, selecting a particular decay. Selections applied at L0 and HLT1 are all inclusive. At L0, selections run on single particles, except for dimuon lines, whilst in HLT1 more flexibility is present, allowing to apply selections on any kind of topology. The HLT2 stage is composed by both inclusive and exclusive trigger lines. A 40% of the output rate is dedicated to inclusive topological selections. Another 40% is reserved to exclusive trigger lines to study c-hadron decays, while the rest is dedicated to other exclusive analyses. The number of trigger lines and their requirements can change by run. Each trigger configuration has an associated Trigger Configuration Key (TCK), which is an hexadecimal number that identifies the trigger conditions. This allows to tag the modifications done at the trigger level and facilitates the access to the trigger information of each run.

At LHCb, different conditions can be applied at the trigger level in order to select a decay of interest. If the trigger requirements are satisfied by certain particles forming a candidate, it is said that they have been Triggered On Signal (TOS). On the other hand, if the event is triggered because other particles satisfy the requirement, the candidate is said to be Triggered Independently of Signal (TIS). As an example, let us consider

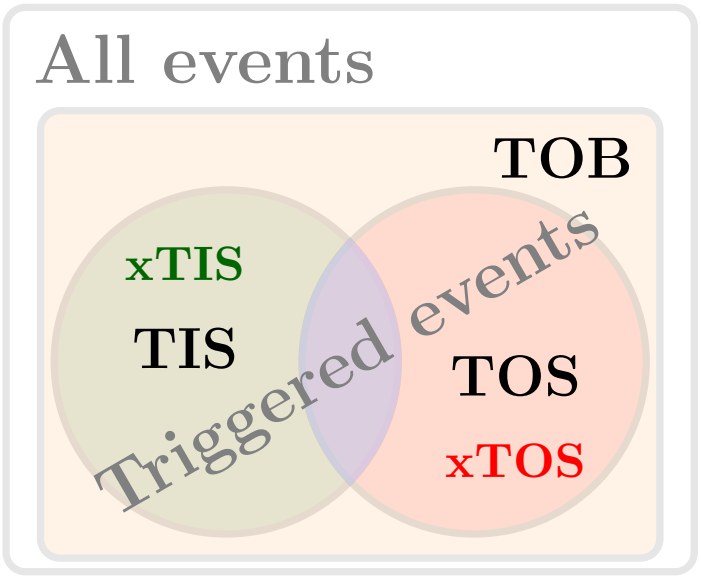

Figure 2.4: Definition of the different trigger categories commonly used at LHCb. The TIS and TOS categories are displayed as green and red regions, respectively, including the overlap between the two circles. The xTIS (xTOS) category contains candidates from the TIS (xTOS) area that do not belong to the blue region. TOB candidates are defined by those that are not TIS nor TOS, but that come from events that have satisfied the trigger requirements.

a trigger line to select two muons independently of the charge, and an event with three muons in it: μ_1, μ_2 and μ_3. If μ_1 and μ_2 satisfy the requirements they are TOS, while μ_3 is TIS. It is important to note that TOS and TIS categories are not exclusive, since μ_1 and μ_3 could also satisfy the selection, a situation where all the muons would be TIS and TOS at the same time. If the particles of interest are the only ones satisfying the requirements, the candidate is Exclusively Triggered On Signal (xTOS). A situation where the trigger requirements are not satisfied by the particles of interest, but only by particles from the rest of the event, is also possible. In this situation the candidate is said to be Exclusively Triggered Independently of Signal (xTIS). Candidates can be built from particles that do not completely satisfy the trigger requirements, and the rest of the event is not sufficient to satisfy them either, but the combination is. In this situation the candidate is said to be Triggered On Both (TOB). An example of a TOB candidate would be if our aforementioned trigger line had selected μ_1 and μ_2 only because part of the information from μ_3 was actually associated to either μ_1 or μ_2 at the trigger level. In general, TOB candidates have worse quality than TIS and TOS candidates, so they are oftenly not used in the analyses. In Fig. 2.4, a detailed diagram explaining the meaning of each trigger category can be found. These definitions apply to any combination of trigger selections.

For the Run 2 of the LHCb, the physics program was extended in order to include strange decays, electroweak, soft QCD, and heavy-ion physics. This was made possible due to the flexible real-time reconstruction and high-level trigger system. Unfortunately, the L0 trigger could not be tuned to increase the efficiency for measurements in many

of the aforementioned fields. The main problem is due to the transverse energy and transverse momentum requirements. L0 trigger lines designed to select single muons had a requirement on single particles to have a p_T greater than $\sim$1 GeV/c. This requirement, highly efficient for most of the b-hadron and electroweak studies, is highly inefficient for strange decays, and is also a stringent constraint to study some c-hadron decays.

During data-taking, random events are persisted independently on whether particles in the event satisfy the trigger requirements or not. This produces a trigger-unbiased sample, since no selection is applied at this stage. In LHCb jargon, this is typically referred to as minimum bias (MB). Despite the majority of the analyses at LHCb are done using exclusively events satisfying the trigger requirements, for some cross-section measurements and luminosity studies, having a trigger-unbiased sample becomes strictly necessary. It is also used to make improvements of the detector and to test the performance of simulated samples. For the study of strange decays, it provides big samples of strange hadrons like K^0_S or Λ. Independently of the presence of efficient trigger lines for many control channels, like $K^0_S \to \pi^+\pi^-$ or $\Lambda \to p\pi^-$, at the L0 and HLT, candidates from MB events can be used to normalize other branching fractions. Trigger-unbiased events are kept at a much lower rate than for normal events. The downscale was applied by TCK for the first part of Run 2 (2015, 2016), whilst it was allowed to vary by run for the second (2017, 2018). By calculating the average downscale factor of the MB trigger per sample, one can easily get the luminosity ratio with respect to the main trigger stream. Since in MB events the normal trigger selections also run, one can easily calculate trigger efficiencies directly on data dividing the candidates that survive to the trigger requirements in the MB by the overall number of candidates in MB:

$$\varepsilon_{\text{trigger}} = \frac{N^{\text{observed}}_{\text{trigger,MB}}}{N^{\text{observed}}_{\text{MB}}}. \tag{2.3}$$

As long as the number of candidates and trigger efficiencies are high enough, this method becomes very useful to calculate trigger efficiencies. This is usually not the case, since the amount of candidates of interest in the MB sample is typically very low. However, for studies involving strange particles Eq. 2.3 becomes very useful due to their very high production rate.

2.2.4 The LHCb trigger for strange decays

The study of strange decays in the LHCb detector constitutes a big challenge due to its configuration designed for b-hadron decays. Already at the trigger level, the big amount of tracks present at very low angles with respect to the beam-pipe, strongly related with the p_T of the particles, drastically increases the computing time needed to process an event. In order to build a decay, without considering the charge of the particles, there are

$$N_{\text{c}} = \begin{cases} \frac{N!}{m!(N-m)!} & \text{if } m \leq N \\ 0 & \text{otherwise} \end{cases} \tag{2.4}$$

combinations, where N is the number of tracks in the event and m the number of tracks to combine. The number of combinations, for a big number of tracks, grows as N^m. A lower p_T selects more background, since chances to find candidates satisfying the requirements

increase with the number of particles. However, profiting from the topology of many decays to study, and applying smart reconstruction techniques at the trigger level, it was possible to overpass this limitation for the Run 2 of the LHCb experiment. A redesigned trigger system allowed to increase the efficiency of this detector to study strange decays, and constitutes the mayor improvement from Run 1.

For the Run 2 of the LHCb detector, two new trigger lines were included at HLT1 and HLT2 to cover strange decays. Additionally, some of the existing lines were also tuned to complement the previous and increase the statistics. The development of the new trigger lines for HLT1 and HLT2 was possible thanks to the inclusion of a smart reconstruction technique for low-p_T muons at HLT1. In proton-proton collisions at the LHC energies there is a large amount of charged particles being generated. Most of them are pions that arise from QCD-induced reactions in the collisions. As a consequence, trigger lines to select pions from strange decays are typically too time consuming to be run for each event. Only downscaled lines[2], or lines with very strong requirements in the pions are allowed to run within the trigger system. This is not the case for muons, since they are produced in smaller quantities in proton-proton collisions at the LHC. In consequence, the occupancy of the MUON system is smaller, so a prompt selection of low-p_T tracks can be made using this detector, reducing the timing cost of tracking at the trigger level.

In the Run 1 of the LHCb detector, the idea of doing a prompt muon identification using VELO tracks and MUON hits was first implemented [84]. This allowed to reduce the p and p_T thresholds at the trigger level, improving the efficiency of the HLT1 muon selections. However, tracks built in the VELO pattern recognition do not have information about the momentum. The momentum was assumed to be 6 GeV/c, a guess that has to be made in order to extrapolate the tracks through the magnet region. Afterwards, a search was done in the muon chambers using M3, the chamber in the middle of the subdetector, to correct the momentum estimate. Tracks were then required to have associated hits in all the muon chambers, and if these satisfied certain requirements the track was considered to pass the selection. Although this method could be used for b-hadron decays, where the transverse momentum of muons is typically above 500 MeV/c, it is not the case for strange decays, where values are around 250 MeV/c. For the Run 2 of the LHCb detector, a similar procedure was considered [85] using tracks with the information from both the VELO and the TT stations. Due to the increased rate of HLT1 in the Run 2 of LHCb, it was possible to promote the VELO tracks using the information from the TT. The presence of a remnant of the magnetic field in the TT region allowed to determine the sign of the track and define the search windows to the left or right of the beam-pipe accordingly. This filtering method was incorporated to several HLT1 lines, not only focused to strange decays, reducing the overall timing in the HLT1 reconstruction sequence. Different studies on Monte Carlo (MC) samples were done, using decays like $K^0_S \to \mu^+\mu^-$, $\Sigma^+ \to p\mu^+\mu^-$ and $K^0_S \to \pi^0\mu^+\mu^-$ to study the impact of the new trigger lines in the efficiency for strange decays. The results [86] showed that, despite the L0 efficiencies remained ∼10% for most of them, the HLT efficiency increased from ∼8% to ∼63%. The overall efficiencies for these decays increased by a factor ∼8 that, together with the increase of luminosity in Run 2, provided a very promising scenario for their study.

[2]A downscaled selection only runs once per a certain amount of events. This is typically achieved by using a random number generator between zero and one. If the number is smaller than the associated downscale, the selection runs on that event.

2.2.5 Simulation at LHCb

In high-energy experiments the usage of simulated samples is widely extended in order to understand the behavior of the detectors and the passage of particles through matter. At LHCb, the simulation process comprises many different steps aiming to reproduce the experimental conditions. Proton-proton collisions are simulated using Pythia [87, 88] with a specific LHCb configuration [89]. Decays of hadronic particles are described by EvtGen [90], in which final-state radiation is generated using Photos [91]. The interaction of the generated particles with the detector and its response are implemented using the Geant4 toolkit [92, 93], as described in Ref. [94].

The aforementioned software packages allow to adapt the conditions to any hadron decay of interest, and to the different operational conditions: energy of the beams, number of protons per bunch, scattering angle and number of visible interactions, among others. In order to generate b and c hadrons, simulated events are forced to contain hard collisions, so it is ensured that at least one of these particles is produced. On the other hand, the large abundance of strange hadrons in any kind of interaction, of around 2.7 K^0_S mesons per event, suggests to use plain proton-proton collisions, which boosts the generation process for these particles.

Simulation of large samples is oftenly a high time and resource consuming task. At LHCb, there are many techniques developed to boost the simulation process. The most basic consists of adding requirements at generator level, like forcing a K^0_S to decay inside the VELO[3]. It is also possible to reduce the number of subdetectors to simulate, like avoiding the propagation of photons in the RICH detectors if their information will not be used afterwards, or simulating only the tracking detectors if no particle identification is needed. In the simulation process, most of the time is spent on simulating the behavior of particles from the underlying event (those that do not correspond to the decay of interest) through the detector. A recent technique has shown that reusing the underlying event many times is possible [95], as long as the correlation between the decay of interest and the underlying event is not needed in the analysis. Since for all these techniques the simulation process is being biased, analysts need to treat properly the magnitudes that can extract from the generated samples, in such a way that biased quantities are not used in the analysis.

[3] Otherwise the tracks from the decay products would not generate hits in this subdetector.

3

Search for the $K^0_S \to \mu^+\mu^-$ decay

In the past, most of the experiments were not able to measure the $K^0_S \to \mu^+\mu^-$ decay due to the shorter lifetime of the K^0_S with respect to the K^0_L, and due to a small production of neutral kaons in the accelerators. Whilst the $K^0_L \to \mu^+\mu^-$ was successfully studied, with a branching fraction currently in agreement with the SM [49, 96], the K^0_S mode was left behind. The last limit on the branching fraction of $K^0_S \to \mu^+\mu^-$ before the LHCb collaboration started to study it, comes from the CERN PS [97], with a value

$$\mathcal{B}_{\text{exp}}(K^0_S \to \mu^+\mu^-) < 3.1 \times 10^{-7} \text{ at } 90\% \text{ CL}. \tag{3.1}$$

No update was done for forty years. The big production of K^0_S at the LHC, together with a redesign of parts of the detector, makes possible for the LHCb experiment to contribute to the measurement of this decay. In 2013, the LHCb collaboration improved the limit using data collected in 2011 [98] by a factor thirty

$$\mathcal{B}(K^0_S \to \mu^+\mu^-) < 9.0\ (11.2) \times 10^{-9} \text{ at } 90\ (95)\% \text{ CL} \tag{3.2}$$

which, after combining it with the result using data from 2012 [56], brought the value down to

$$\mathcal{B}(K^0_S \to \mu^+\mu^-) < 0.8\ (1.0) \times 10^{-9} \text{ at } 90\ (95)\% \text{ CL}. \tag{3.3}$$

In this chapter, the search for the $K^0_S \to \mu^+\mu^-$ decay using the Run 2 data set collected by the LHCb detector is described. The results were compiled for the publication in Ref. [99]. The measurement of the value in Eq. 3.3 is also part of this work. However, differences in the analysis strategy between Run 1 and Run 2 depend mostly on the different data-taking conditions. As a consequence, the analysis of Run 1 data is not presented here.

3.1 Introduction

The LHCb detector has been designed and optimized for the study of b and c hadron decays. However, in proton-proton collisions, a huge amount of strange particles are produced. At LHCb, around 10^{13} K^0_S/fb^{-1} decay inside the VELO. Considering efficiencies

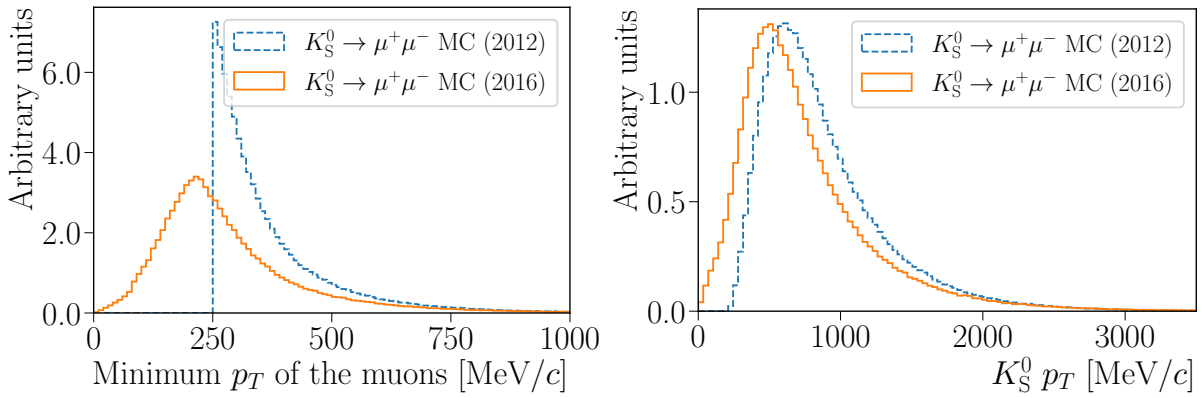

(a) (b)

Figure 3.1: Distribution of the transverse momentum of muons (left) and K^0_S mesons (right) from simulated $K^0_S \to \mu^+\mu^-$ decays. Improvements in the low-p_T reconstruction and more relaxed p_T requirements allowed to increase the trigger and selection efficiencies.

at the percent level for K^0_S decays, one can naively assume sensitivities to branching fractions on the order of $\mathcal{O}(10^{-10})$ for the Run 2 of LHCb.

The main challenge at LHCb is to maintain the efficiency high enough for this decay. For Run 1 and Run 2, the main bottleneck was present at the trigger level. The L0 trigger, with p_T requirements of $\mathcal{O}(1\ \text{GeV}/c)$ on both single muons or muon pairs, is very inefficient for strange decays, as can be seen in Fig. 3.1. In the HLT, most of the trigger lines were not efficient for strange decays either. The modification of some of the selections to include the K^0_S mass range allowed to increase the efficiency for 2012. During the Run 2 of the LHCb, the reconstruction of low-p_T muons was improved, as discussed in Sect. 2.2.3, allowing to relax the p_T requirements to 80 MeV/c. As a consequence, more efficient trigger lines could be developed, this time completely focused on strange decays. Unfortunately, these improvements were put in place in 2016, and due to the small amount of luminosity collected in 2015, data from this year was not used in this analysis. The studies presented here were done using LHCb data collected in 2016–2018 at a center-of-mass energy of 13 TeV, corresponding to a total luminosity of 5.57 fb^{-1}.

The $K^0_S \to \pi^+\pi^-$ decay is the most suitable candidate to serve as control and normalization mode for $K^0_S \to \mu^+\mu^-$ due to its abundance and similar topology. Although the HLT trigger could be modified to efficiently select $K^0_S \to \mu^+\mu^-$, this is not the case for $K^0_S \to \pi^+\pi^-$. The large amount of pions in proton-proton collisions at high energies makes impossible to follow a similar procedure to reconstruct and select $K^0_S \to \pi^+\pi^-$ at an acceptable rate. As a consequence, $K^0_S \to \pi^+\pi^-$ candidates are taken from MB samples due to its large abundance. Through the analysis, requirements on $K^0_S \to \pi^+\pi^-$ and $K^0_S \to \mu^+\mu^-$ candidates have been kept as close as possible, so systematic uncertainties are reduced in the normalization

$$\mathcal{B}(K^0_S \to \mu^+\mu^-) = \frac{N^\mu_{\text{observed}}}{N^\pi_{\text{observed}}} \times \frac{\varepsilon^\pi}{\varepsilon^\mu} \times \mathcal{B}(K^0_S \to \pi^+\pi^-), \tag{3.4}$$

where superscripts μ and π refer to the $K^0_S \to \mu^+\mu^-$ and $K^0_S \to \pi^+\pi^-$ decay, respectively.

Since this is a search for a new decay mode of a known particle, a blind approach is

adopted. The dimuon invariant mass region 490–510 MeV/c^2 is not studied till the full analysis strategy is fixed. This includes the optimization of the selection, the definition of the fit model and the way to extract the limit of the branching fraction and its central value. Once these are set, the fit to the full dimuon invariant mass is performed.

3.2 Corrections to simulation

Due to discrepancies between simulated and data candidates, a correction must be applied to the former in order to get more realistic samples. In this analysis, two different methods have been used to correct for these discrepancies.

A dedicated Gradient Boosted Decision Tree (GBDT) was trained to do a regression so a weight can be assigned to each simulated candidate, emulating the distributions of the data sample. In order to weight the simulated samples of K^0_S decays, $K^0_S \to \pi^+\pi^-$ candidates from both MC and data are used. Candidates are asked to satisfy minimal selection requirements, common for both samples. Topological variables are used to train this algorithm, since the amount of simulated candidates is not high enough to account for differences in more complex variables, like the ghost probability of the tracks. These include the momentum, p_T, impact parameter (IP) and impact parameter significance (χ^2_{IP}) of the K^0_S candidate, the latter defined as the variation of the χ^2 of the fit to the secondary vertex (SV) when considering the track of this particle, and the distance of closest approach (DOCA) of the two tracks. The distributions of the variables before and after weighting the simulated $K^0_S \to \pi^+\pi^-$ sample can be seen in Fig. 3.2.

Weights calculated with the GBDT algorithm are used in the multivariate analysis (MVA) analysis described in Sect. 3.4.2. However, they are not used to estimate efficiencies, since evaluating the associated systematic uncertainties would be too expensive computationally. Samples can also be weighted by using the distributions of certain variables of interest that are representative of the decay. The p_T of the K^0_S is a good variable to weight the simulated candidates, since under the LHCb conditions most of the other variables are correlated with it. Due to the good momentum resolution of the LHCb detector $[0.5, 1.0]\%$ [70] it is also possible to weight the simulated samples at the generator level, that is, without simulating the detector response. The distribution of the p_T is binned for both data and simulated $K^0_S \to \pi^+\pi^-$ candidates using adaptive binning in order to have the same amount of simulated candidates in each of them. The weight is determined as

$$\omega_i = \frac{N^{\text{MB}}_{\text{selection},i}}{N^{\text{MC}}_{\text{selection},i}}, \tag{3.5}$$

where the subscript i refers to the p_T bin. The p_T distributions before and after weighting the simulated $K^0_S \to \pi^+\pi^-$ sample can be seen in Fig. 3.3. Simulated samples for K^0_S decays are weighted by assigning a weight corresponding to the associated p_T bin for each candidate.

3.3 Trigger

Since the L0 trigger could not be rearranged to increase the efficiency for strange decays, it was decided to split the analysis in two samples depending on the decisions taken at

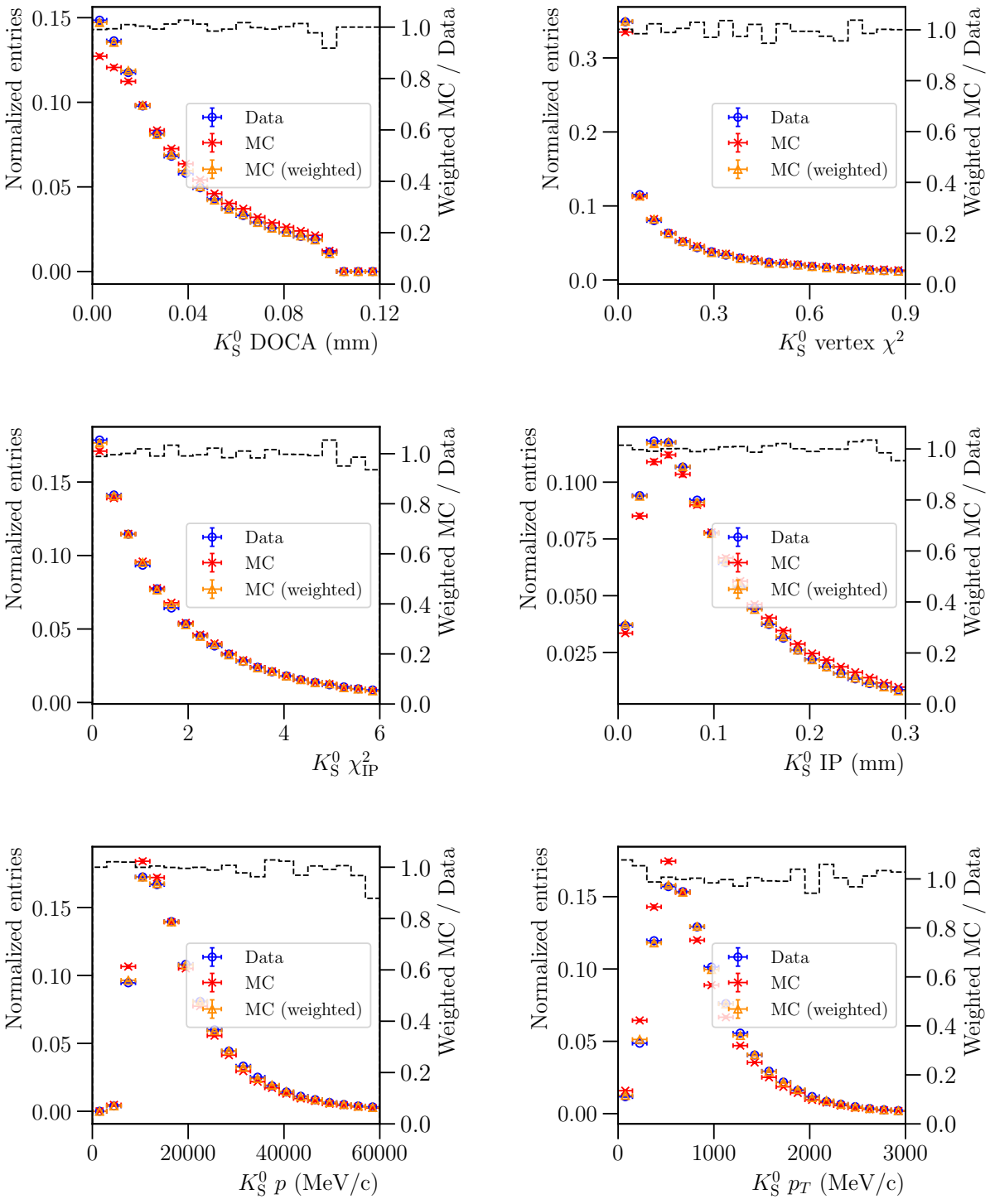

Figure 3.2: Distribution of the variables used in the GBDT-based regression to improve the agreement between data and simulated samples. Data is shown in blue circles, whilst the corrected MC is displayed as orange triangles. The distribution of simulated candidates before the correction is shown in red crosses. The ratio between data and corrected MC is displayed as a dashed black histogram.

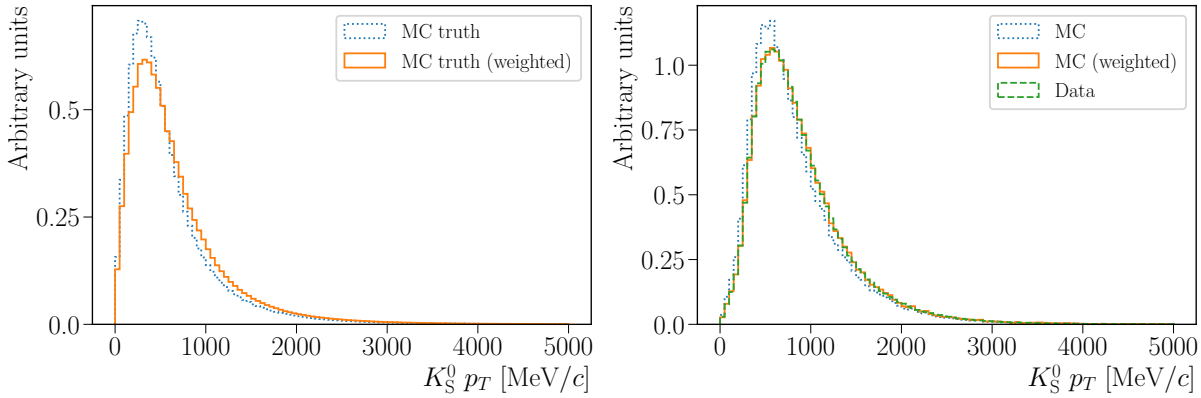

(a) (b)

Figure 3.3: Distribution of simulated candidates before (left) and after (right) the detector simulation steps and fiducial selection requirements. The dotted blue line in the right figure is used, together with the dashed green, to define the weights. The shapes for both weighted and un-weighted samples are shown.

this stage. L0 lines select events depending on the number of hits in the SPD detector (nSPD), which give an idea of the multiplicity of the event, and on a bare calculation of the transverse energy (E_T) and the p_T using the calorimeters and muon chambers. Additional discrimination between electrons and photons is done using the PS. For 2017 and 2018, an additional requirement was applied to each event on the sum of the E_T from the previous event (`SumEtPrev`). This requirement was included in order to reduce the throttle caused by the OT due to its higher drift-time, with small impact in this analysis. The L0 trigger lines used in the analysis were:

- **L0Muon:** This line required nSPD < 450, which stayed constant throughout the entire three-year period. In the years 2017 and 2018 the line had an additional requirement of `SumEtPrev` < 1 GeV. Additionally, this line had requirements on the transverse momentum of the muon candidate varying in 0.7–1.9 GeV/c.

- **L0Muon,lowMult:** Similar to `L0Muon`, but with stronger requirements in the multiplicity nSPD < 20, and a more relaxed requirement in the transverse momentum of the muons $p_T > 400$ MeV/c. The thresholds remained constant for the three years.

- **L0DiMuon:** This line was designed to select dimuon candidates with high-p_T signatures. A more relaxed requirement of nSPD < 900 was applied, constant for the entire three-year period. The requirement on the p_T of the dimuon candidate varied in 0.9–1.8 GeV/c.

- **L0Electron, L0Photon, L0Hadron:** These lines select either electrons, photons or hadrons, respectively. The requirement on the multiplicity was set to nSPD < 450 for the three years. In the years 2017 and 2018 the line had an additional requirement of `SumEtPrev` < 1 GeV. The `L0Electron` line had requirements on the transverse energy to be greater than 1.95–2.8 GeV. For `L0Photon`, the requirements on this

magnitude were a bit tighter, varying in 2.4–3.2 GeV. Finally, for `L0Hadron`, the transverse energy had to be greater than 3.10–4.05 GeV.

Requirements on the nSPD and `SumEtPrev` can be seen in Fig. 3.4. The first sample corresponds to TIS candidates, coming from events where reconstructed particles (excluding those used to form the candidate) satisfy any of the requirements from the main physics lines of the L0 (all discussed above excluding `L0Muon,lowMult`), independently of whether the candidate itself satisfies them. The second sample is defined by xTOS candidates, composed by those satisfying either the `L0Muon`, `L0DiMuon` or the `L0Muon,lowMult` line, and not contained in the previous category. This sample is smaller than that of TIS, although a higher purity is achieved due to the stronger requirements.

At the HLT, a common selection follows for both categories, requiring the candidates to be TOS at both HLT1 and HLT2. For HLT1, two trigger lines are used, called `Hlt1DiMuonNoL0` and `Hlt1DiMuonLowMass`. Both profit from the low-p_T reconstruction algorithm presented in Sect. 2.2.3. Requirements on the IP, momentum, transverse momentum, χ^2_{IP} and track quality are applied to the muons. The combination of the two oppositely-charged muons must generate a vertex with good quality, with dimuon invariant mass in the nominal K^0_{S} mass range. At the last stage of the trigger, only one trigger line is used, called `Hlt2DiMuonSoft`. Some of the requirements from HLT1 are tightened, like for the IP of the muons and the track quality. The decay products must also satisfy certain muon identification requirements based on the output of a neural-network. A requirement is applied to the angle between two oppositely-charged muons in order to avoid muon candidates formed from the same VELO track. This is followed by a requirement on the direction of flight of the candidate and on the SV position to avoid decay-vertices reconstructed in the beam-pipe, where most of the background concentrates.

The selection of $K^0_{\text{S}} \to \pi^+\pi^-$ candidates follows a different path with respect to $K^0_{\text{S}} \to \mu^+\mu^-$. The lack of efficient trigger lines at L0 and HLT1 to select this decay, together with the high value of the branching fraction for K^0_{S} decaying to two pions [47]

$$\mathcal{B}(K^0_{\text{S}} \to \pi^+\pi^-) = (69.20 \pm 0.05)\,\% \tag{3.6}$$

makes the usage of candidates from MB necessary. The topology of the events containing $K^0_{\text{S}} \to \pi^+\pi^-$ and $K^0_{\text{S}} \to \mu^+\mu^-$ candidates is identical, and so is the response of the trigger to the underlying event for any of the two decays. This way, TIS efficiencies are expected to be the same for $K^0_{\text{S}} \to \pi^+\pi^-$ and $K^0_{\text{S}} \to \mu^+\mu^-$. The $K^0_{\text{S}} \to \pi^+\pi^-$ candidates from MB samples can be used to determine the efficiency of the TIS requirement at L0. From equation Eq. 2.3, and using the number of observed candidates for each case:

$$\varepsilon_{\text{L0TIS}} = \frac{N^{\text{observed}}_{\text{L0TIS,MB}}}{N^{\text{observed}}_{\text{MB}}}. \tag{3.7}$$

This can be studied in both data and simulated candidates, and serves as a check for data/MC agreement.

3.4 Topological selection

As explained in Sect. 3.1, the selections for both the signal channel $K^0_{\text{S}} \to \mu^+\mu^-$ and the control mode $K^0_{\text{S}} \to \pi^+\pi^-$ are kept as close as possible to reduce the systematic

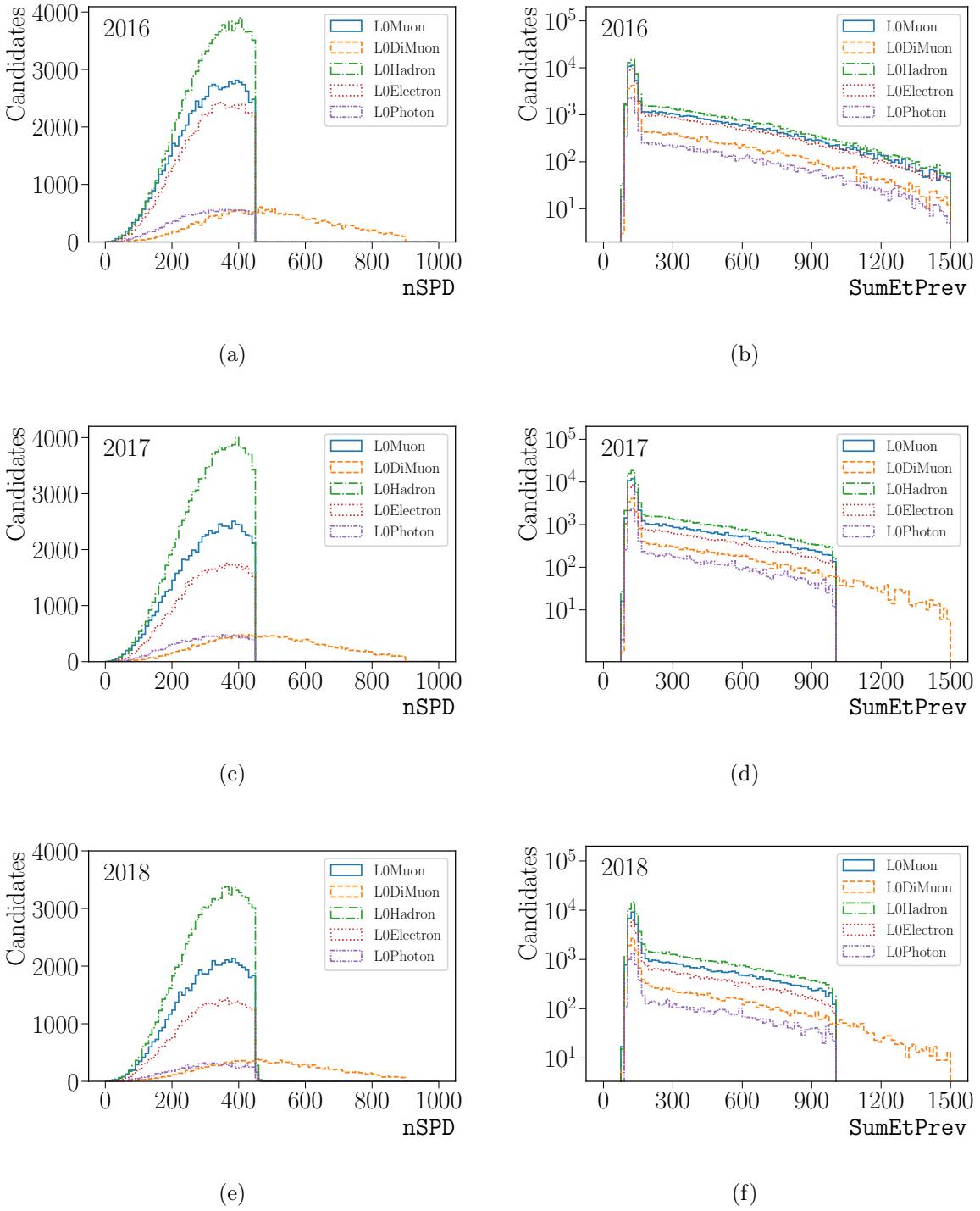

Figure 3.4: Distribution of nSPD (left) and `SumEtPrev` (right) for the three years, in different trigger conditions, for $K^0_S \to \pi^+\pi^-$ candidates from MB samples. The thresholds for the different L0 trigger selections can be clearly seen.

uncertainties. The first part of the selection is common for both $K^0_S \to \mu^+\mu^-$ trigger categories, since the impact in the efficiency is very similar. For the two decays of interest, candidates are formed from two oppositely-charged tracks, with a χ^2_{IP} greater than 100. The decay products must form a good vertex, with a DOCA smaller than 0.1 mm. In order to force the K^0_S candidate to arise from the PV, the IP of the K^0_S candidate must be smaller than 0.4 mm. An additional requirement is applied to the measured K^0_S lifetime $\tau > 0.6 \times \tau_{K^0_S}$, so the SV is detached from the PV. The mass range considered for $K^0_S \to \mu^+\mu^-$ and $K^0_S \to \pi^+\pi^-$ is different, since for the former the sample is expected to be dominated by $K^0_S \to \pi^+\pi^-$ decays, where the two pions are misidentified as muons. This contribution is expected to lie to the left of the K^0_S nominal mass, so only candidates with an invariant mass greater than 470 MeV/c^2 and smaller than 600 MeV/c^2 are considered. For $K^0_S \to \pi^+\pi^-$, the mass range is set to 400–600 MeV/c^2. For the $K^0_S \to \mu^+\mu^-$ selection, muon candidates are required to have a certain number of associated hits (which depends on the momentum) in the muon chambers. For $K^0_S \to \pi^+\pi^-$ a similar condition is applied by asking the pion candidates to be within the acceptance of the muon subdetector. These requirements are aligned with those of the trigger discussed in Sect. 3.3. After these selections, based on the topology of the decays, further requirements are applied in order to reduce specific backgrounds.

3.4.1 Background from Λ decays

A big background from $\Lambda \to p\pi^-$ decays is expected, due to the large production of Λ baryons and the high branching fraction. The misidentification of protons as pions affects the selection of $K^0_S \to \pi^+\pi^-$ candidates, used in the normalization. The contribution from $\Lambda \to p\pi^-$ decays is removed by applying a requirement in the Armenteros–Podolanski plane [100]. The latter is generated by representing the transverse momentum versus the asymmetry in the longitudinal momentum

$$\alpha = \frac{p^1_L - p^2_L}{p^1_L + p^2_L}, \tag{3.8}$$

both with respect to the direction of flight of the decaying particle. This method has been widely used in the past in order to separate $K^0_S \to \pi^+\pi^-$ from $\Lambda \to p\pi^-$ decays. In the Armenteros–Podolanski plane particles are represented by ellipses. If the two decay products have the same mass, the decay generates a single ellipse. If the masses are different, two ellipses are generated depending whether one is dealing with a particle or an anti-particle. In Fig. 3.5a, the distributions for different decays can be seen, as taken from simulated proton-proton collisions. The $\Lambda \to p\pi^-$ contribution is removed imposing the condition

$$\left| \left[\left((\alpha \pm \alpha^*) \frac{M_\Lambda p_{K^0_S}}{2p^* \sqrt{p^2_{K^0_S} + M^2_\Lambda}} \right)^2 + \left(\frac{p'_T}{p^*} \right)^2 \right] - 1 \right| > 0.3, \tag{3.9}$$

where

$$\alpha^* \equiv \frac{M^2_p - M^2_\pi}{M^2_\Lambda} \tag{3.10a}$$

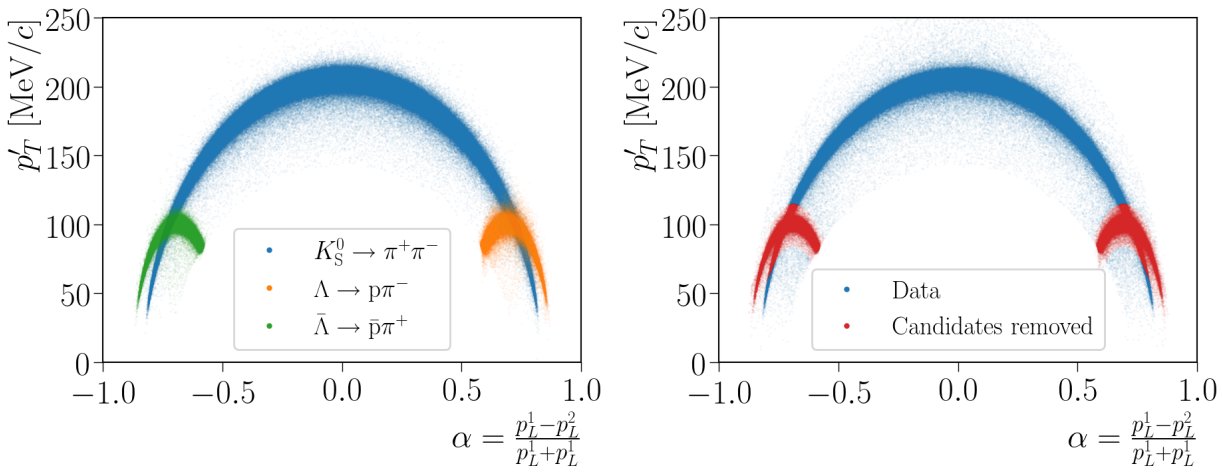

(a) Simulated candidates

(b) Data candidates

Figure 3.5: Distribution of simulated (left) and data (right) $K^0_S \to \pi^+\pi^-$ candidates in the Armenteros–Podolanski plane [100]. The $K^0_S \to \pi^+\pi^-$, $\Lambda \to p\pi^-$ and $\bar{\Lambda}^0 \to \bar{p}\pi^+$ can be clearly seen. The region in red present in the right figure is removed applying the requirement in Eq. 3.9.

$$p^* \equiv \frac{(M_\Lambda^2 - M_p^2 - M_\pi^2)^2 - 4M_p^2 M_\pi^2}{4M_\Lambda^2}. \tag{3.10b}$$

This has an efficiency of 99% for $K^0_S \to \pi^+\pi^-$ candidates, with a negligible impact for $K^0_S \to \mu^+\mu^-$. The effect of this requirement in $K^0_S \to \pi^+\pi^-$ data candidates can be seen in Fig. 3.5b.

3.4.2 Material interactions and combinatorial background

In proton-proton collisions, particles arising from the PV can produce inelastic interactions with the material of the detector, generating new particles from it. For b and c hadron decays, with a flight distance of a few millimeters, the decay vertices are very unlikely to be produced within the detector material. However, for particles with a greater lifetime like the K^0_S, this effect must be considered. When looking at position of the SV for $K^0_S \to \mu^+\mu^-$ candidates in the right sideband of the invariant mass the pattern of the VELO and the surrounding cavity can be clearly seen, as shown in Fig. 3.6. Having a good description of the detector is crucial to remove such background. For the Run 2, an specific tool was developed in order to deal with this problem, called `VeloMatterVeto`. Using data proton-gas events, collected by LHCb, a parametrization of the VELO subdetector could be done [101]. This tool allows to compute an uncertainty-weighted distance to the material using the information of the SV position and its uncertainties

$$D = \sqrt{\frac{(\mathrm{SV}_x - x)^2}{\sigma_x^2} + \frac{(\mathrm{SV}_y - y)^2}{\sigma_y^2} + \frac{(\mathrm{SV}_z - z)^2}{\sigma_z^2}}. \tag{3.11}$$

In the last years, the usage of MVA has been widely extended. In particle physics, NN and Boosted Decision Tree (BDT) algorithms are used to do pattern recognition, particle

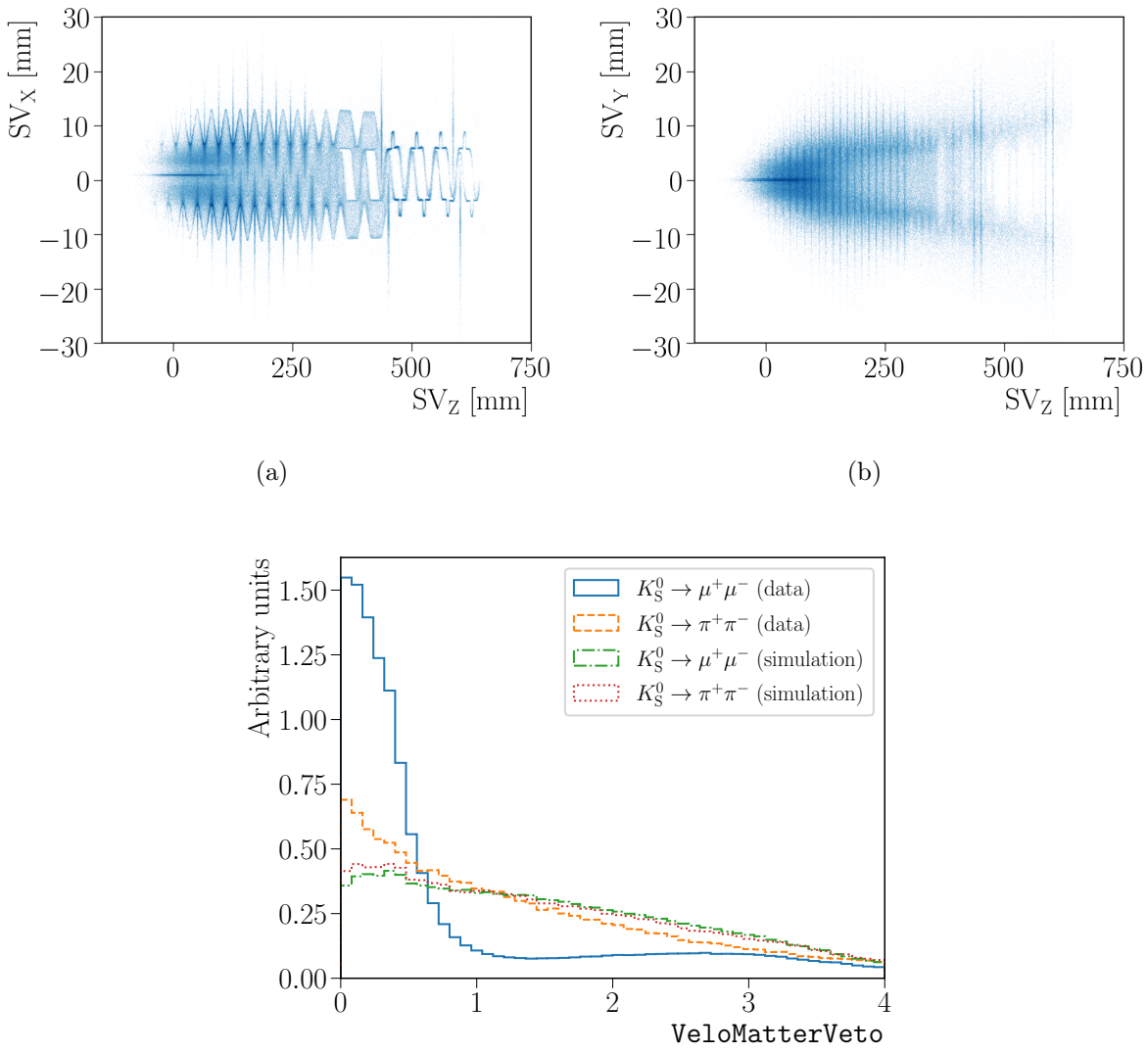

(a) (b)

(c)

Figure 3.6: Top: Distribution of $K^0_S \to \mu^+\mu^-$ candidates satisfying $m_{\mu^+\mu^-} > 520$ MeV/c^2. The pattern of the VELO can be clearly seen, as well as that of the surrounding cavity. Bottom: Distribution of the `VeloMatterVeto` variable for simulated and data $K^0_S \to \mu^+\mu^-$ and $K^0_S \to \pi^+\pi^-$ candidates. Data candidates are required to have an invariant mass greater than 520 MeV/c^2. Background coming from material interactions is smaller in the $K^0_S \to \pi^+\pi^-$ selection, due to the higher purity of the sample.

identification, clustering and background discrimination, among others. For $K^0_S \to \mu^+\mu^-$, Adaptive Boosted Decision Tree (ABDT) algorithms are used in order to reduce the amount of combinatorial background, arising from random combinations of tracks, and particles from inelastic material interactions. Due to the different features of TIS and xTOS candidates, it is decided to train two different classifiers. In order to reduce the backgrounds described above, a suitable proxy must be found. For this purpose $K^0_S \to \mu^+\mu^-$ candidates from the right sideband[1] $m_{\mu^+\mu^-} > 520$ MeV/c^2 of the data samples of the three years are used. Simulated $K^0_S \to \mu^+\mu^-$ candidates satisfying the trigger and selection requirements are utilized as a proxy for signal. The MVA-based weights described in Sect. 3.2 are included in order to have a more realistic signal proxy.

Candidates of the background proxy will be later included in the fit to the dimuon invariant mass. Overtraining could make the ABDT algorithm be suitable to fight only against the background candidates in the right-sideband, but not for those in the signal region. It could also lead to an overestimation of the efficiency if taken from simulation, since the algorithm would be describing the properties of each simulated candidate and not that of the general sample. To avoid it, the *k-folding* approach is used [102]. The sample is divided in two, where the first sample is used to train an algorithm that is later applied to the second, and vice versa.

Once the proxies were prepared, the two ABDT algorithms could be trained. In order to keep the algorithm efficient also to select $K^0_S \to \pi^+\pi^-$ candidates, only topological variables were used. The ABDT input variables are: the kaon candidate decay time and $\chi^2_{\rm IP}$; the $\chi^2_{\rm IP}$, track-fit χ^2, and the ghost probability of each of the two tracks, defined from a neural-network algorithm trained to identify fake tracks; the distance of closest approach between the two tracks; the cosine of the helicity angle; the χ^2 of the SV fit; two SV isolation variables, defined as the difference in the χ^2 in the vertex fit with only the two final-state tracks and that obtained when adding the one or two nearest tracks; and the VELO material veto variable. The performance of the algorithms can be seen in Fig. 3.7. No indication of overtraining is found from the difference between training and test samples for signal and background proxies, as shown in Fig. 3.8.

Several checks were needed to be done in order to determine whether the ABDT algorithm could be biasing the samples on an unexpected way. In this study the goal is to measure a branching fraction searching for a peaking structure in the dimuon invariant mass spectrum. It becomes strictly necessary that the algorithms do not distort the shape of the mass for background candidates, generating a peak. A check is done in $K^0_S \to \mu^+\mu^-$ data candidates from the left and right sidebands, shown in Fig. 3.9. No evidence for an increase (decrease) of the signal probability is observed for the higher (lower) mass region in the left (right) sideband. A check in the signal region could only be done using simulated candidates asking explicitly not to match a true $K^0_S \to \pi^+\pi^-$ decay. In this case, no peaking structure is observed, and the shape is very similar to that from the $K^0_S \to \mu^+\mu^-$ sidebands. In conclusion, no correlation of the ABDT algorithm with the mass is observed.

Since the ABDT algorithm must be efficient for both $K^0_S \to \mu^+\mu^-$ and $K^0_S \to \pi^+\pi^-$, a check is done to look for a correlation with the muon identification variable that will be later used to discriminate $K^0_S \to \mu^+\mu^-$ against $K^0_S \to \pi^+\pi^-$ and $K^0 \to \pi\mu\nu$. The presence of a high correlation would be a clear signature that the algorithm is making a distinction

[1]The left sideband is dominated by $K^0_S \to \pi^+\pi^-$ decays where both pions are misidentified as muons.

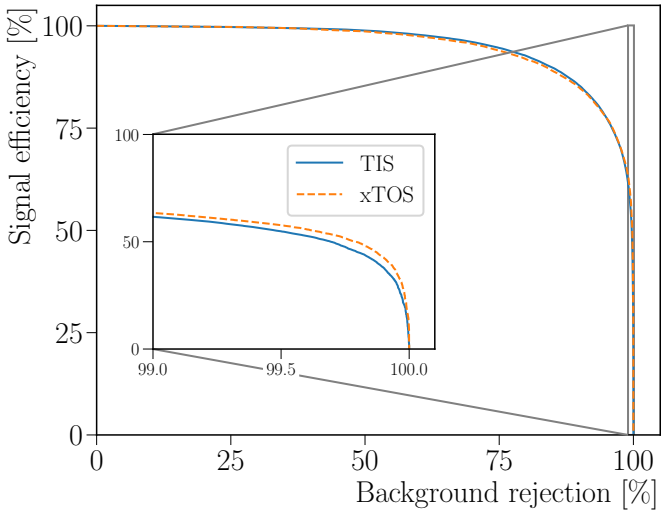

Figure 3.7: Receiver Operating Characteristic (ROC) curves for the two different ABDT algorithms trained to discriminate against combinatorial background and material interactions. The difference in the performance of the two algorithms can only be appreciated when requiring a high background rejection. The small plot corresponds to the performance when the requirement to remove 99% of the background is applied.

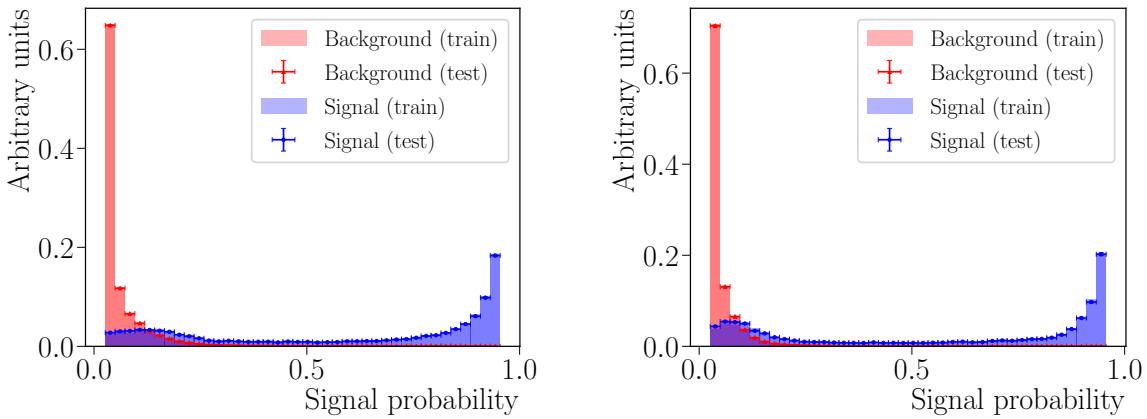

(a) (b)

Figure 3.8: Distribution of the signal probability for the TIS (left) and xTOS (right) trigger categories. Test samples are shown as red triangles for background and blue circles for signal. The associated training samples are displayed as filled histograms of the same color, respectively.

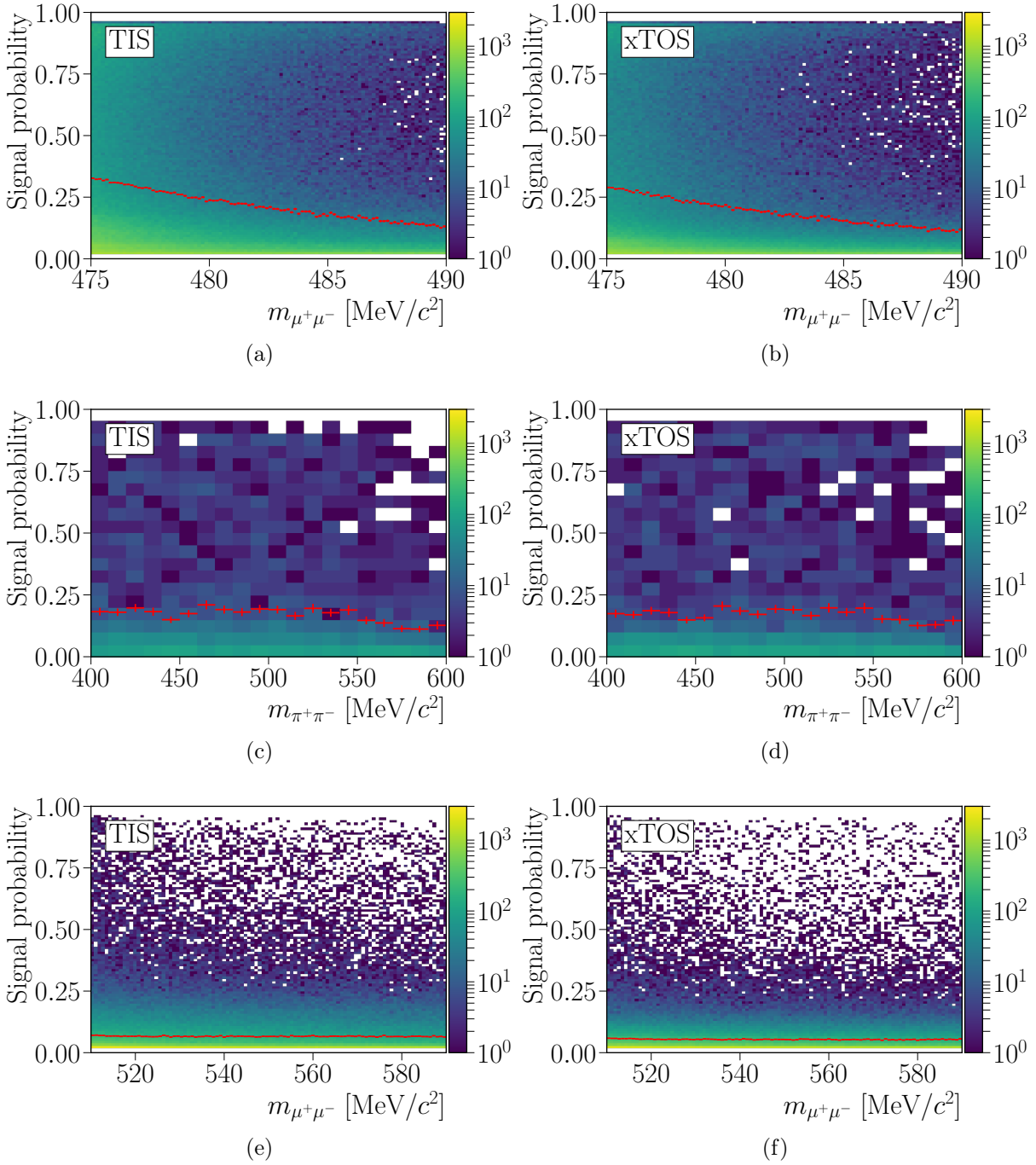

Figure 3.9: Correlation of the two ABDT classifiers (one per trigger category) with the invariant mass of the decay products. Top and bottom plots are obtained from data dimuon candidates, revealing no increase of the signal probability around the signal region. The middle plots were obtained from simulated candidates explicitly requiring not to match a $K^0_S \to \pi^+\pi^-$ decay.

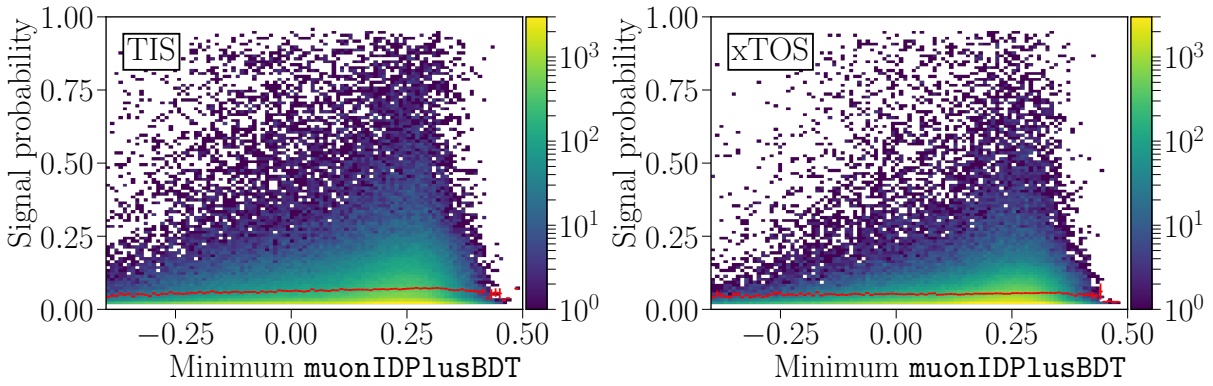

(a) (b)

Figure 3.10: Distribution of the signal probability for the two ABDT classifiers versus the minimum value of the `muonIDPlusBDT` algorithm for the two decay products, obtained from data $K^0_S \to \mu^+\mu^-$ candidates satisfying $m_{\mu^+\mu^-} > 520$ MeV/c^2. The profile of the distribution is displayed in red. No significant correlation is observed.

between pions and muons. The results are shown in Fig. 3.10. Only a small correlation can be appreciated, which is normal due to the fact that muons have in general a better track quality than pions. The efficiency of the ABDT algorithm is high enough to maintain a big sample of $K^0_S \to \pi^+\pi^-$ candidates after this step, corresponding to 63%(65%) for TIS (xTOS).

In order to remove most of the background, a requirement on the signal probability to be greater than 0.50(0.36) is imposed to the TIS (xTOS) category. This leads to a background rejection of 99%, maintaining an efficiency of 62%(64%) for TIS (xTOS). Samples are then splitted in ten bins for each classifier, so the $K^0_S \to \mu^+\mu^-$ efficiency is the same for each bin. The final sample is composed by the remaining candidates in the twenty bins. This is an approach commonly used in searches for new decays since it allows to increase the sensitivity, fully exploiting the power of the ABDT algorithms.

3.5 Muon identification

Misidentification of pions as muons is the major source of background for the study of $K^0_S \to \mu^+\mu^-$ at LHCb. The most dangerous background is $K^0_S \to \pi^+\pi^-$, where the two pions are misidentified as muons. This comes from the large abundance of $K^0_S \to \pi^+\pi^-$ candidates, due to its high branching fraction. Despite the good resolution of the LHCb around the K^0_S mass, on the order of 4 MeV/c^2, the right tail of doubly-misidentified $K^0_S \to \pi^+\pi^-$ decays, as shown in Fig. 3.11, can still contaminate the signal region. In order to increase the sensitivity for the $K^0_S \to \mu^+\mu^-$ search this tail must be reduced as much as possible, so applying offline muon identifications requirements becomes strictly necessary. Another decay that can be misidentified as signal is $K^0 \to \pi\mu\nu$. The branching fraction of $K^0_S \to \pi\mu\nu$ has been recently measured by the KLOE-2 collaboration [103], with a value of

$$\mathcal{B}(K^0_S \to \pi\mu\nu) = (4.57 \pm 0.11 \pm 0.16) \times 10^{-4}. \tag{3.12}$$

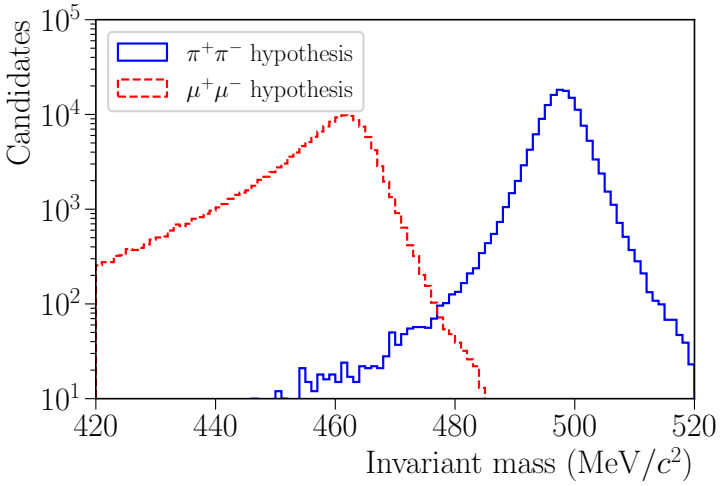

Figure 3.11: Distribution of simulated $K^0_S \to \pi^+\pi^-$ candidates reconstructed as $K^0_S \to \pi^+\pi^-$ (solid blue) and as $K^0_S \to \mu^+\mu^-$ (dashed red). Peaks are separated by 40 MeV/c^2, corresponding to 10 times the resolution.

The less suppressed K^0_L mode [1],

$$\mathcal{B}(K^0_L \to \pi\mu\nu) = (27.04 \pm 0.07)\,\% \tag{3.13}$$

has much lower detection efficiency at LHCb, so both K^0_S and K^0_L decays are expected to contribute in similar amounts. Despite some of the selection requirements are efficient rejecting this type of background, like that on the IP of the K^0_S, if the neutrino is soft enough it becomes very similar to a two-body decay, where only one pion needs to be misidentified as a muon.

At LHCb, there are two main ways of misidentifying pions as muons. The difference between these two particles is related to the track quality and to the muon chamber response. Early decays-in-flight of pions through the process $\pi \to \mu\nu$ will lead to the reconstruction of a track that belongs to a true muon. The energy carried by the neutrino is the only responsible for making the initial part of the track (belonging to the pion) and the second (belonging to the muon) differ. If the momentum of the pion is low, the angle between the two parts of the track is high, and these candidates can be easily identified and removed. However, at LHCb low-mass particles from the PV have a big boost in z making them to be more aligned. Furthermore, if the energy of the neutrino is small enough the impact on the track quality is negligible and turns out to be a background that is not possible to remove. The other main source of misidentification comes from the incorrect assignment of hits in the muon chambers to pion tracks. This can happen if real muons from the underlying event leave hits right in front of the pion track. Again, one can disentangle real muons from these kind of pions by looking at the properties of the hits in the muon chambers. A muon would have the hits aligned with its track, whilst for misidentified pions, associated hits will be scattered in the different stations. For low-p_T tracks, the occupancy of the muon detector is higher, so chances to find pion tracks matched to muon hits increase.

For the second part of the Run 1 of the LHCb, a new muon identification algorithm, described in Sect. 2.2.2, was introduced to provide coverage for low-p_T muons. This was

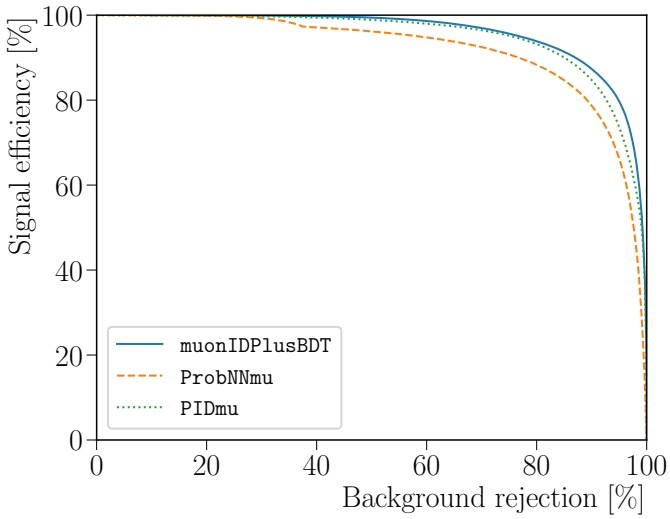

Figure 3.12: ROC curves for different muon identification algorithms available within the LHCb framework. The signal efficiency has been calculated using simulated $K^0_S \to \mu^+\mu^-$ candidates. The background rejection is computed from data $K^0_S \to \mu^+\mu^-$ candidates from the left sideband $m_{\mu^+\mu^-} < 490$ MeV/c^2, where doubly-misidentified $K^0_S \to \pi^+\pi^-$ candidates dominate. The best performance is achieved with the `muonIDPlusBDT` algorithm, used in this analysis.

one of the major improvements in the analysis of data from 2012. For Run 2, the same algorithm was used in order to fight against misidentification of pions as muons in the detector. This algorithm, called `muonIDPlusBDT`, has a better performance at low-p_T than other algorithms used in LHCb, as can be seen in Fig. 3.12, by making a more smart usage of the information of the different subdetectors of LHCb.

An optimization of the requirement on the output from this algorithm was done per bin of the two BDT classifiers described in Sect. 3.4.2. The optimization is done using the following procedure:

- For each ABDT bin, a fit to a power law, accounting for the $K^0_S \to \pi^+\pi^-$ contribution; and an exponential, representing the remaining background, is done outside the blind region with no requirement on the muon identification. This fit serves as a template to generate pseudo-experiments, and it is not repeated in order to avoid statistic noise and fit failures.

- The efficiency on simulated $K^0_S \to \mu^+\mu^-$ candidates and the background rejection from the sidebands in data are calculated for different requirements on the `muonIDPlusBDT` variable. Afterwards, background-only pseudo-experiments are generated using the model from the previous step.

- The CLs [104], assuming one signal candidate in each ABDT bin[2] is used as a figure of merit to maximize the significance. The optimal requirements arise as the minimum of the expected CLs.

[2]This corresponds to $\mathcal{B}(K^0_S \to \mu^+\mu^-) \sim 4 \times 10^{-11}$.

Table 3.1: Minimum value required for the `muonIDPlusBDT` variable of both tracks forming a $K^0_S \to \mu^+\mu^-$ candidate. The same requirements apply to the TIS and xTOS trigger categories. For simplicity, the requirements have been forced to be the same among different bins.

ABDT bins	Minimum `muonIDPlusBDT`
$[1, 2, 3]$	0.30
$[4, 5]$	0.25
$[6, 7, 8]$	0.15
$[9, 10]$	0.10

This method assumes that the background model does not vary with the requirement on the `muonIDPlusBDT` variable that is, for the precision needed, a good approximation. The optimization curves can be consulted in Appendix B. The results are similar for both the TIS and xTOS trigger categories, and a wide range of values with an expected CLs close to the optimal requirement is observed. For simplicity, bins with similar optimized values for the requirement have been forced to match, also between the two trigger categories. The requirements for the different bins can be seen in Table 3.1.

3.6 Backgrounds

Although $K^0_S \to \pi^+\pi^-$ is the most dangerous background, a wider set of decays that could distort the dimuon invariant mass spectrum have been studied. These studies have been done based either on the known or on the SM-predicted branching fractions, using both data and simulated samples.

3.6.1 $K^0_S \to \pi^+\pi^-$ and $K^0 \to \pi\mu\nu$

To discriminate against these two types of background, arising from misidentification of pions as muons, the muon identification algorithm described in Sect. 3.5 is used. Due to the large abundance of $K^0_S \to \pi^+\pi^-$, a big contribution from these decays is expected in the dimuon invariant mass. Those candidates are modeled with a power-law distribution

$$f(x) = \frac{N}{(x-m)^n}, \tag{3.14}$$

where the location of the asymptote, ruled by m, is forced to be outside the fit range; n is the power of the distribution; and N the normalization constant. The shape of doubly-misidentified $K^0_S \to \pi^+\pi^-$ candidates was validated using three different simulated samples. Sample A is composed by pions from $K^0_S \to \pi^+\pi^-$ decays that are stable, and do not decay in the LHCb detector volume. The other two, named B and C, are composed by $K^0_S \to \pi^+\pi^-$ candidates where one pion and the two pions are forced to decay inside the VELO, respectively. There is a good agreement between the distribution of simulated candidates and the power-law function, as can be seen in Fig. 3.13. The fitted function is

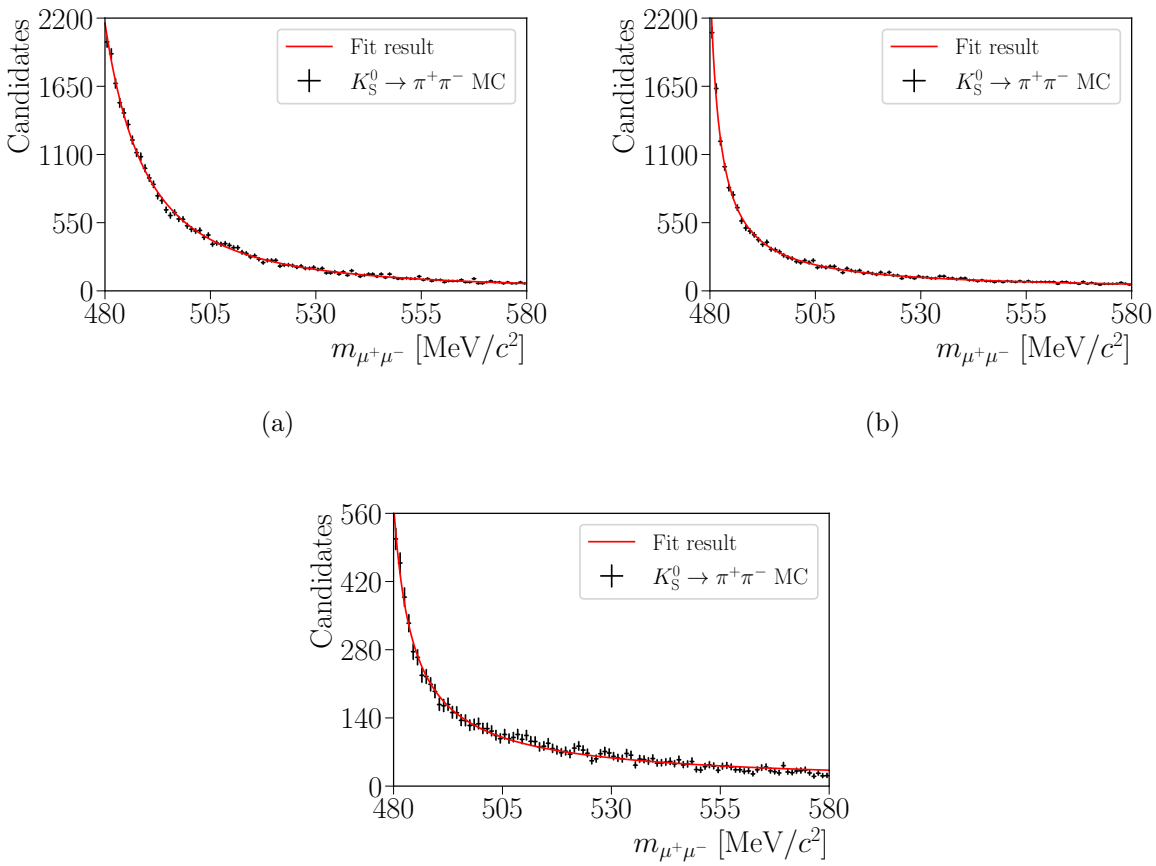

(a)

(b)

(c)

Figure 3.13: Distribution of the dimuon invariant mass of simulated $K^0_S \to \pi^+\pi^-$ candidates where the two pions are stable (top left), one of them is forced to decay inside the VELO (top right), and both are forced to decay inside the VELO (bottom). The results of the fits to a power-law function are displayed in red.

Table 3.2: Expected and observed $K^0_S \to \pi^+\pi^-$ yields from the fit to the dimuon invariant mass of simulated $K^0_S \to \pi^+\pi^-$ candidates, together with the number of observed $K^0_S \to \mu^+\mu^-$ candidates after considering a free signal component. The rows refer to combinations of the simulated $K^0_S \to \pi^+\pi^-$ samples under different conditions on the decay time of the pions.

Sample	**Exp. $K^0_S \to \pi^+\pi^-$**	**Obs. $K^0_S \to \pi^+\pi^-$**	**Obs. $K^0_S \to \mu^+\mu^-$**
A	13328 ± 115	13103	-130 ± 130
B	6364 ± 80	6338	21 ± 86
C	3002 ± 55	2936	-89 ± 68
A + B	19491 ± 140	19441	-33 ± 160
A + C	16301 ± 128	16039	-250 ± 150
B + C	9289 ± 96	9274	-2 ± 100
A + B + C	22447 ± 150	22377	-120 ± 170

used in order to compare the number of expected and observed $K^0_S \to \pi^+\pi^-$ candidates in the signal region. These two numbers are found to be very similar, as shown in Table 3.2. Additional fits were done including a free signal component, obtaining values for the number of signal candidates that are compatible with zero.

For $K^0_S \to \pi\mu\nu$, studies using fast simulation revealed that candidates satisfying the selection, trigger and muon identification requirements will have a dimuon invariant mass distribution flattened in the signal region. Due to the lower number of expected candidates with respect to doubly-misidentified $K^0_S \to \pi^+\pi^-$, this contribution would be absorbed by the power-law function used to describe the $K^0_S \to \pi^+\pi^-$ background, so it is not considered in the fit. Candidates from $K^0_L \to \pi\mu\nu$ decays are expected to contribute on a similar way.

3.6.2 $K^0_L \to \mu^+\mu^-$

This decay is an irreducible background for $K^0_S \to \mu^+\mu^-$. The longer lifetime of the K^0_L hadron makes the efficiency to reconstruct $K^0_L \to \mu^+\mu^-$ much lower than that for the K^0_S. Taking into account its known branching fraction [47]

$$\mathcal{B}(K^0_L \to \mu^+\mu^-) = (6.84 \pm 0.11) \times 10^{-9}, \tag{3.15}$$

the effective branching fraction is measured to be

$$\mathcal{B}_{\text{eff}}(K^0_L \to \mu^+\mu^-) = \mathcal{B}(K^0_L \to \mu^+\mu^-) \times \frac{\varepsilon_L}{\varepsilon_S} \sim 10^{-11}, \tag{3.16}$$

were $\varepsilon_{S(L)}$ is the global efficiency for the K^0_S (K^0_L) decay mode. The contamination was negligible for Run 1 analyses, but it is considered in this study since the effective branching

fraction approaches the current sensitivity $\mathcal{O}(10^{-10})$. The $K^0_L \to \mu^+\mu^-$ contribution is included in the fit to the dimuon invariant mass in a similar way to $K^0_S \to \mu^+\mu^-$:

- The mass shape parameters are shared with those of $K^0_S \to \mu^+\mu^-$.
- The branching fraction of $K^0_L \to \mu^+\mu^-$ is well known and is added as an external constraint to the fit.
- The normalization factors and distributions across the different ABDT bins are also shared with the signal. An additional factor is added, which accounts for the difference of the efficiency between K^0_S and K^0_L decay modes due to the detector lifetime acceptance.

The interference between K^0_S and K^0_L states has a lifetime much shorter than the K^0_L, being only twice that of the K^0_S. Its contribution is only non-zero in the case of a sizeable $K^0/\bar{K}^0$ production asymmetry, or a tagged analysis. Since at LHCb the production of neutral kaons and anti-kaons is very similar [48], this effect is neglected in the analysis.

3.6.3 $\Lambda \to p\pi^-$ and $\Lambda \to p\mu\nu_\mu$

A veto has been applied to these decays during the selection step, described in Sect. 3.4.1. Due to the presence of a neutrino, the mass shape of $\Lambda \to p\mu\nu_\mu$ is different to that of $\Lambda \to p\pi^-$, and the two-body invariant mass distribution extends softly towards the left sideband in both dimuon and dipion mass hypotheses. From a simulated sample of $\Lambda \to p\mu\nu_\mu$ decays, a high suppression is found in the $K^0_S \to \mu^+\mu^-$ selection step $\varepsilon_{\text{selection}} < 9.7 \times 10^{-6}$ at 95%CL. Considering the extra suppression factor due to the different cross-section of Λ baryons with respect to K^0_S mesons $\sim$0.45 [105], similar efficiencies for the muon identification ($\sim$60% for `IsMuon` only), trigger 11% and ABDT $\sim$60% to $K^0_S \to \mu^+\mu^-$, the total efficiency is $\sim 10^{-8}$. Together with the known branching fraction $\mathcal{B}(\Lambda \to p\mu\nu_\mu) = (1.57 \pm 0.35) \times 10^{-4}$ [106], the number of expected candidates would be similar to those expected for $K^0_S \to \mu^+\mu^-$, but mostly lying in the region corresponding to doubly misidentified $K^0_S \to \pi^+\pi^-$ decays, and are thus neglected. In the $K^0_S \to \pi^+\pi^-$ samples, due the higher cross-section, branching fraction and relative efficiency $\sim 10^3$ for $K^0_S \to \pi^+\pi^-$, this contribution is also neglected.

3.6.4 Radiative decays of neutral kaons

Background events from $K^0_L \to \mu^+\mu^-\gamma$ and $K^0_S \to \mu^+\mu^-\gamma$ can be selected as signal if the photon momentum is small enough. The $\mathcal{B}(K^0_L \to \mu^+\mu^-\gamma)$ has been measured to be [47]

$$\mathcal{B}(K^0_L \to \mu^+\mu^-\gamma) = (3.59 \pm 0.11) \times 10^{-7}. \tag{3.17}$$

The $\mathcal{B}(K^0_S \to \mu^+\mu^-\gamma)$ is expected to be $(1.45 \pm 0.27) \times 10^{-9}$ in the SM [49]. The efficiency of reconstruction and selection in $\mathcal{B}(K^0_S \to \mu^+\mu^-\gamma)$ phase-space (PHSP) MC is 8.8×10^{-5} including the ABDT requirements. This number reduces to 4.1×10^{-5} for $m_{\mu^+\mu^-} > 480$ MeV/c^2, to be compared to $\varepsilon^{\text{selection}}_{\text{MC}} = 4.5 \times 10^{-3}$ for signal. A correction must be applied to account for the fact that $K^0_S \to \mu^+\mu^-\gamma$ and $K^0_L \to \mu^+\mu^-\gamma$ decays do not follow

a PHSP differential decay rate. Instead, they peak at low values of the dimuon mass. Reweighting the events accordingly, one obtains:

$$\frac{\varepsilon(K^0_S \to \mu^+\mu^-\gamma)}{\varepsilon(K^0_S \to \mu^+\mu^-\gamma)^{\text{PHSP}}} \lesssim 0.121, \tag{3.18}$$

integrated over all the ABDT bins. Hence, the overall efficiency ratio to the signal is 1.1×10^{-3} yielding an effective branching fraction of at most 10^{-12} (assuming all events are around the peak) and hence negligible for the current level of sensitivity. The expected yield in the left sideband is $\lesssim 1$ candidate, and thus negligible compared to $K^0_S \to \pi^+\pi^-$. A similar level is expected from the K^0_L mode, because of the 2×10^{-3} extra suppression due to the lifetime acceptance. The contribution from $K^0 \to \mu^+\mu^-\gamma\gamma$ is expected to be even smaller, since the branching fractions are further suppressed for both K^0_S and K^0_L mesons.

3.6.5 Decays from light-unflavored resonances

Another possible source of background comes from the detached decays of $\omega\,(782)$ and η hadrons. These particles can be generated in the decays of b and c hadrons, which could produce detached vertices. Dedicated simulated samples of $\omega\,(782) \to \pi^0\pi^+\pi^-$ and $\eta \to \pi^+\pi^-\gamma$ decays have been created, where the $\omega\,(782)$ and η mesons are forced to come from b or c hadrons. No simulated candidates survive the $K^0_S \to \pi^+\pi^-$ selection. In addition, no peaking structures have been observed in the dipion invariant mass of the $K^0_S \to \pi^+\pi^-$ data samples. The muonic modes, suppressed by a factor $\sim 10^4$ with respect to the pionic, are even more unlikely to survive the $K^0_S \to \mu^+\mu^-$ selection and trigger requirements. In conclusion, contributions from these decays are neglected.

3.6.6 Other rare strange decays

Contributions from other rare strange decays could also appear in the dimuon invariant mass spectrum. These include $\Sigma^+ \to p\mu^+\mu^-$, $K^0_S \to \pi^0\mu^+\mu^-$, $K^+ \to \pi^+\mu^+\mu^-$. For decays of the Σ^+, the dimuon invariant mass has an upper bound of ~ 251 MeV/c^2, corresponding to the invariant mass difference of the Σ^+ and the proton. In the $K^0_S \to \pi^0\mu^+\mu^-$ decay, the absence of the π^0 makes the maximum value allowed for $m_{\mu^+\mu^-}$ to be shifted ~ 135 MeV/c^2 to the left of the K^0_S nominal mass. Finally, for decays of the K^+, the argument is similar to that of the K^0_S, with an additional suppression due to the higher lifetime of the K^+. In conclusion, no candidates from these decays are expected in the final samples.

3.7 Normalization

Efficiencies are quantities based on a binomial distribution, since the numerator and denominator are correlated (they are quantities taken from the same sample). Although the measured value

$$\varepsilon = \frac{n_{\text{pass}}}{N_{\text{total}}} \tag{3.19}$$

is easy to calculate independently of whether we are dealing with a weighted sample or not, it is not the same for its uncertainty. If the sample is not weighted, quite often the

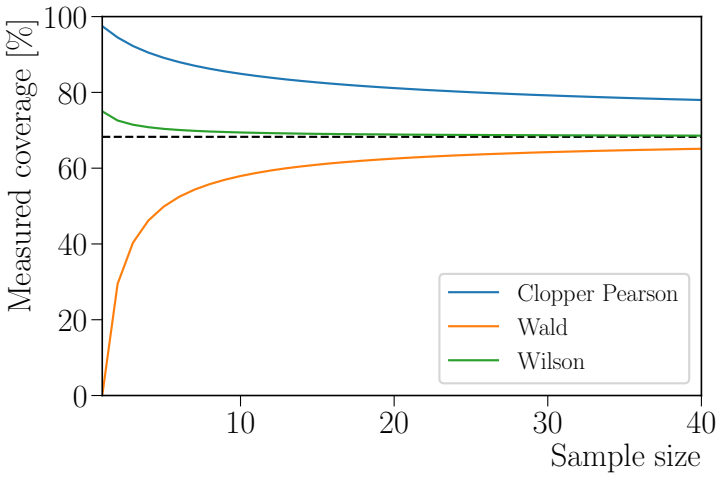

Figure 3.14: Evolution of the measured coverage as a function of the sample size for different methods to calculate uncertainties on efficiencies. The Wilson method provides the best coverage independently of the sample size, slightly overestimating it for small samples.

normal approximation, or Wald method [107], is used to estimate the uncertainties

$$\varepsilon \pm \sqrt{\frac{\varepsilon(1-\varepsilon)}{N_{\text{total}}}}. \tag{3.20}$$

However, it produces empty intervals for $n_{n_{\text{pass}}} = 0$ or $n_{\text{pass}} = N_{\text{total}}$. Furthermore, intervals have much less coverage than 68%, leading to predictions that are too good. To take into account the binomial nature of the efficiencies, the Clopper-Pearson can be used [108]. This provides a method not based on any approximation

$$\varepsilon \in \left[B\left(\frac{1-\alpha}{2}; n_{\text{pass}}, N_{\text{total}} - n_{\text{pass}} + 1\right), B\left(\frac{1+\alpha}{2}; n_{\text{pass}} + 1, N_{\text{total}} - n_{\text{pass}}\right)\right], \tag{3.21}$$

where $B(q; a, b)$ denotes the q^{th} quantile of a beta distribution with shape parameters a and b, and α is the desired coverage (68% for 1σ). The problem of Eq. 3.21 is that it drastically overcovers. On the other hand, the Wilson method [109]

$$\frac{2n_{\text{pass}} + 1}{2\left(1 + N_{\text{total}}\right)} \pm \frac{1}{1 + \frac{1}{N_{\text{total}}}} \pm \sqrt{\frac{\varepsilon(1-\varepsilon)}{N_{\text{total}}} + \frac{1}{4N_{\text{total}}^2}} \tag{3.22}$$

has a good coverage, although it is underestimated for low values of N_{total}, leading to a conservative case. A comparative of the coverage for the different methods can be seen in Fig. 3.14. For the non-weighted case, the Wilson method is the preferred way to calculate the uncertainties of the efficiencies in this analysis.

If the sample is weighted, the Wilson method from Eq. 3.22 can not be used, since it only works for integers. However, the expression from Eq. 3.20 can be readapted to cover weighted samples

$$\varepsilon \pm \sqrt{\frac{W_1^2\sigma_2^2 + W_2^2\sigma_1^2}{\left(W_1 + W_2\right)^4}}, \tag{3.23}$$

where

$$n_1 + n_2 = N_{\text{total}} \tag{3.24a}$$

$$W_{1(2)} = \sum_{i=1}^{n_1(n_2)} \omega_i \tag{3.24b}$$

$$\sigma^2_{1(2)} = \sum_{i=1}^{n_1(n_2)} \omega_i^2. \tag{3.24c}$$

This expression is chosen to estimate the efficiencies from the p_T-weighted simulated samples. It can be easily seen that Eq. 3.23 converts into Eq. 3.20 when the weights are all set to one.

3.7.1 Efficiencies from simulation

The determination of the efficiencies for the signal and control mode is done using simulated samples for the two decays, and $K^0_S \to \pi^+\pi^-$ candidates from data. In order to correct for data/MC differences, the p_T-based weights, described in Sect. 3.4.2, are used. Efficiencies from the different analysis steps (reconstruction, selection, trigger, ABDT, muon identification) are calculated separately by taking into account the number of events before each requirement and after applying it. However, total efficiencies are directly calculated from the number of candidates in the first and last steps of the selection procedure. This avoids calculating erroneously the uncertainties of the total efficiencies, since otherwise correlations would need to be taken into account. The general expression to normalize the $K^0_S \to \mu^+\mu^-$ decay is

$$\mathcal{B}(K^0_S \to \mu^+\mu^-) = \frac{N^{\mu}_{\text{observed}}}{N^{\pi}_{\text{observed}}} \times \frac{\varepsilon^{\pi}_{\text{selection}}}{\varepsilon^{\mu}_{\text{selection}}} \times \frac{\varepsilon^{\pi}_{\text{trigger}}}{\varepsilon^{\mu}_{\text{trigger}}} \times \frac{1}{\varepsilon^{\mu}_{\text{muon-ID}}} \times \mathcal{B}(K^0_S \to \pi^+\pi^-), \tag{3.25}$$

where the superscript μ (π) denotes the efficiency for $K^0_S \to \mu^+\mu^-$ ($K^0_S \to \pi^+\pi^-$). The first factor in Eq. 3.25 is the number of $K^0_S \to \pi^+\pi^-$ and $K^0_S \to \mu^+\mu^-$ candidates that are observed in the samples. The next factor comes from the different selection and requirements in the ABDT classifier, which have been made to be as close as possible for both the signal and control decays. The efficiency of the trigger is taken into account in the third factor, where $\varepsilon^{\pi}_{\text{trigger}}$ is simply the average downscale factor of the no-bias stream (s_{MB}). There are twenty different subsets of data: ten bins of the ABDT response for each of the two trigger categories. As a consequence, Eq. 3.25 is applied to each of them separately, leading to a different efficiency value in each bin.

Reconstruction and selection efficiencies are similar for both $K^0_S \to \mu^+\mu^-$ and $K^0_S \to \pi^+\pi^-$, as shown in Table 3.3. However, there is a substantial increase for $K^0_S \to \mu^+\mu^-$ at low p_T, as can be seen in Fig. 3.15, due to the different reconstruction efficiency for muons and pions. The efficiencies for $K^0_S \to \mu^+\mu^-$ and $K^0_S \to \pi^+\pi^-$ after splitting in bins of the ABDT classifiers are summarized in Table 3.4 and Table 3.5, respectively. The values of the efficiencies obtained counting the number of candidates in the MC samples and using the GBDT weights explained in Sect. 3.2 can be consulted in Appendix C. The difference among the methods is later used to compute a systematic uncertainty.

Table 3.3: Selection efficiencies for $K^0_S \to \mu^+\mu^-$ and $K^0_S \to \pi^+\pi^-$ candidates before the division in bins of the ABDT classifiers. The p_T-based weights described in Sect. 3.2 have been considered to calculate these values.

	$\boldsymbol{K^0_S \to \mu^+\mu^-}$	$\boldsymbol{K^0_S \to \pi^+\pi^-}$
Reconstruction + selection	$(7.639 \pm 0.011) \times 10^{-3}$	$(5.223 \pm 0.017) \times 10^{-3}$
TIS	$(6.726 \pm 0.036) \times 10^{-2}$	
xTOS	$(4.108 \pm 0.028) \times 10^{-2}$	

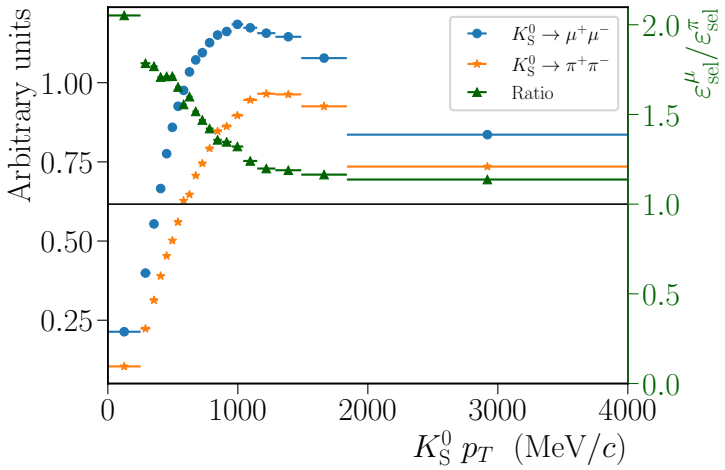

Figure 3.15: Selection efficiencies for different bins based on the p_T of the K^0_S candidate in $K^0_S \to \mu^+\mu^-$ and $K^0_S \to \pi^+\pi^-$ simulated decays. The difference between the two relies mostly on the different reconstruction efficiency for muons and pions.

Table 3.4: Efficiencies of the requirements in the ABDT algorithms and muon identification, together with the overall efficiency for $K^0_S \to \mu^+\mu^-$ candidates in each trigger category. The p_T-based weights described in Sect. 3.2 have been considered to calculate these values.

	TIS			**xTOS**		
ABDT bin	**ABDT**	**muon-ID**	**Total**	**ABDT**	**muon-ID**	**Total**
1	$(6.20 \pm 0.13) \times 10^{-2}$	0.263 ± 0.010	$(8.38 \pm 0.36) \times 10^{-6}$	$(6.37 \pm 0.17) \times 10^{-2}$	0.302 ± 0.013	$(6.04 \pm 0.31) \times 10^{-6}$
2	$(6.20 \pm 0.13) \times 10^{-2}$	0.250 ± 0.010	$(7.96 \pm 0.35) \times 10^{-6}$	$(6.37 \pm 0.17) \times 10^{-2}$	0.277 ± 0.013	$(5.53 \pm 0.30) \times 10^{-6}$
3	$(6.20 \pm 0.13) \times 10^{-2}$	0.273 ± 0.010	$(8.68 \pm 0.37) \times 10^{-6}$	$(6.37 \pm 0.17) \times 10^{-2}$	0.315 ± 0.013	$(6.30 \pm 0.31) \times 10^{-6}$
4	$(6.20 \pm 0.13) \times 10^{-2}$	0.495 ± 0.011	$(1.58 \pm 0.05) \times 10^{-5}$	$(6.37 \pm 0.17) \times 10^{-2}$	0.531 ± 0.014	$(1.06 \pm 0.04) \times 10^{-5}$
5	$(6.19 \pm 0.13) \times 10^{-2}$	0.517 ± 0.011	$(1.65 \pm 0.05) \times 10^{-5}$	$(6.37 \pm 0.17) \times 10^{-2}$	0.576 ± 0.014	$(1.15 \pm 0.04) \times 10^{-5}$
6	$(6.20 \pm 0.13) \times 10^{-2}$	0.827 ± 0.008	$(2.64 \pm 0.06) \times 10^{-5}$	$(6.37 \pm 0.17) \times 10^{-2}$	0.866 ± 0.009	$(1.73 \pm 0.05) \times 10^{-5}$
7	$(6.20 \pm 0.13) \times 10^{-2}$	0.829 ± 0.008	$(2.64 \pm 0.06) \times 10^{-5}$	$(6.37 \pm 0.17) \times 10^{-2}$	0.887 ± 0.009	$(1.77 \pm 0.05) \times 10^{-5}$
8	$(6.20 \pm 0.13) \times 10^{-2}$	0.836 ± 0.008	$(2.66 \pm 0.06) \times 10^{-5}$	$(6.37 \pm 0.17) \times 10^{-2}$	0.882 ± 0.009	$(1.76 \pm 0.05) \times 10^{-5}$
9	$(6.20 \pm 0.13) \times 10^{-2}$	0.914 ± 0.006	$(2.91 \pm 0.07) \times 10^{-5}$	$(6.36 \pm 0.17) \times 10^{-2}$	0.927 ± 0.007	$(1.85 \pm 0.05) \times 10^{-5}$
10	$(6.19 \pm 0.13) \times 10^{-2}$	0.932 ± 0.005	$(2.97 \pm 0.07) \times 10^{-5}$	$(6.36 \pm 0.17) \times 10^{-2}$	0.948 ± 0.006	$(1.89 \pm 0.05) \times 10^{-5}$

Table 3.5: Efficiency of the requirements in the ABDT classifiers, together with the overall efficiency for $K^0_S \to \pi^+\pi^-$ candidates in each trigger category. The total efficiencies do not include the average downscale factor of minimum bias. The p_T-based weights described in Sect. 3.2 have been considered to calculate these values.

	TIS		**xTOS**	
ABDT bin	**ABDT**	**Total**	**ABDT**	**Total**
1	$(7.05 \pm 0.08) \times 10^{-2}$	$(3.68 \pm 0.05) \times 10^{-4}$	$(7.76 \pm 0.09) \times 10^{-2}$	$(4.05 \pm 0.05) \times 10^{-4}$
2	$(7.22 \pm 0.08) \times 10^{-2}$	$(3.77 \pm 0.05) \times 10^{-4}$	$(7.60 \pm 0.09) \times 10^{-2}$	$(3.97 \pm 0.05) \times 10^{-4}$
3	$(7.12 \pm 0.08) \times 10^{-2}$	$(3.72 \pm 0.05) \times 10^{-4}$	$(7.66 \pm 0.09) \times 10^{-2}$	$(4.00 \pm 0.05) \times 10^{-4}$
4	$(6.82 \pm 0.08) \times 10^{-2}$	$(3.56 \pm 0.04) \times 10^{-4}$	$(8.10 \pm 0.09) \times 10^{-2}$	$(4.23 \pm 0.05) \times 10^{-4}$
5	$(7.18 \pm 0.08) \times 10^{-2}$	$(3.75 \pm 0.05) \times 10^{-4}$	$(7.06 \pm 0.08) \times 10^{-2}$	$(3.69 \pm 0.05) \times 10^{-4}$
6	$(6.33 \pm 0.08) \times 10^{-2}$	$(3.31 \pm 0.04) \times 10^{-4}$	$(5.87 \pm 0.08) \times 10^{-2}$	$(3.06 \pm 0.04) \times 10^{-4}$
7	$(6.12 \pm 0.08) \times 10^{-2}$	$(3.20 \pm 0.04) \times 10^{-4}$	$(5.62 \pm 0.08) \times 10^{-2}$	$(2.93 \pm 0.04) \times 10^{-4}$
8	$(5.78 \pm 0.08) \times 10^{-2}$	$(3.02 \pm 0.04) \times 10^{-4}$	$(5.15 \pm 0.07) \times 10^{-2}$	$(2.69 \pm 0.04) \times 10^{-4}$
9	$(4.90 \pm 0.07) \times 10^{-2}$	$(2.56 \pm 0.04) \times 10^{-4}$	$(5.41 \pm 0.07) \times 10^{-2}$	$(2.83 \pm 0.04) \times 10^{-4}$
10	$(4.53 \pm 0.07) \times 10^{-2}$	$(2.36 \pm 0.04) \times 10^{-4}$	$(4.67 \pm 0.07) \times 10^{-2}$	$(2.44 \pm 0.04) \times 10^{-4}$

Table 3.6: Values for the average downscale factor of the no-bias stream for the different years of data-taking associated to this analysis, together with the value of the parameter to cross-check the procedure. The different quantities needed for the calculation of this parameter are also shown.

	2016	**2017**	**2018**
s_{MB}	5.66509×10^{-7}	5.30689×10^{-7}	4.43192×10^{-7}
$\mathcal{L}$	1619.00 ± 80.95	1666.43 ± 83.32	2027.74 ± 101.39
N^{π}_{MB}	1046988 ± 1170	965636 ± 1095	1003799 ± 1095
α	$(8.76 \pm 0.44) \times 10^{-10}$	$(9.16 \pm 0.46) \times 10^{-10}$	$(8.95 \pm 0.45) \times 10^{-10}$

3.7.2 Determination of s_{MB}

As discussed in Sect. 2.2.3, the usage of MB samples implies that one has to calculate the average downscale factor of the no-bias trigger stream, s_{MB}. In 2016, the downscale varied by TCK, whilst for 2017 and 2018 it was allowed to modify it by run. In order to calculate s_{MB}, both the integrated luminosity from the main stream and the downscale factor, determined run by run, need to be used. The average downscale factor is calculated as

$$s_{MB} = \frac{\sum_i s^i_{MB} \mathcal{L}_i}{\mathcal{L}}, \tag{3.26}$$

where i refers to each run, and $\mathcal{L}$ stands for the integrated luminosity of the main stream

$$\mathcal{L} = \sum_i^{\text{runs}} \mathcal{L}_i. \tag{3.27}$$

The downscale factor for a single run can be calculated as

$$s^i_{MB} = \frac{R^i_{MB}}{f^i_{LHC} N^i_{cb}} \tag{3.28}$$

where R^i_{MB} is the overall rate of the no-bias stream, f^i_{LHC} is the revolution frequency of the LHC and N^i_{cb} is the number of colliding bunches. A cross-check for the value of s_{MB} was done using the number of observed $K^0_S \to \pi^+\pi^-$ candidates in the different years of data-taking. Assuming a similar selection efficiency for the three years, the value

$$\alpha = \frac{s_{MB}\mathcal{L}}{N^{\pi}_{MB,\text{selection}}} \tag{3.29}$$

must be constant for all of them, where $N^{\pi}_{MB,\text{selection}}$ is the number of observed $K^0_S \to \pi^+\pi^-$ candidates in the MB sample satisfying the selection requirements[3]. The values for s_{MB} during the different years of data-taking associated to this analysis can be consulted in Table 3.6, together with the values for Eq. 3.29. The number of $K^0_S \to \pi^+\pi^-$ candidates were obtained from fits to the dipion invariant mass spectra, using a double Crystal-ball probability density function (PDF) [110, 111] to describe the signal and an exponential for the background. The results of the fits are shown in Fig. 3.16.

[3]The responses of the ABDT classifiers are not considered here.

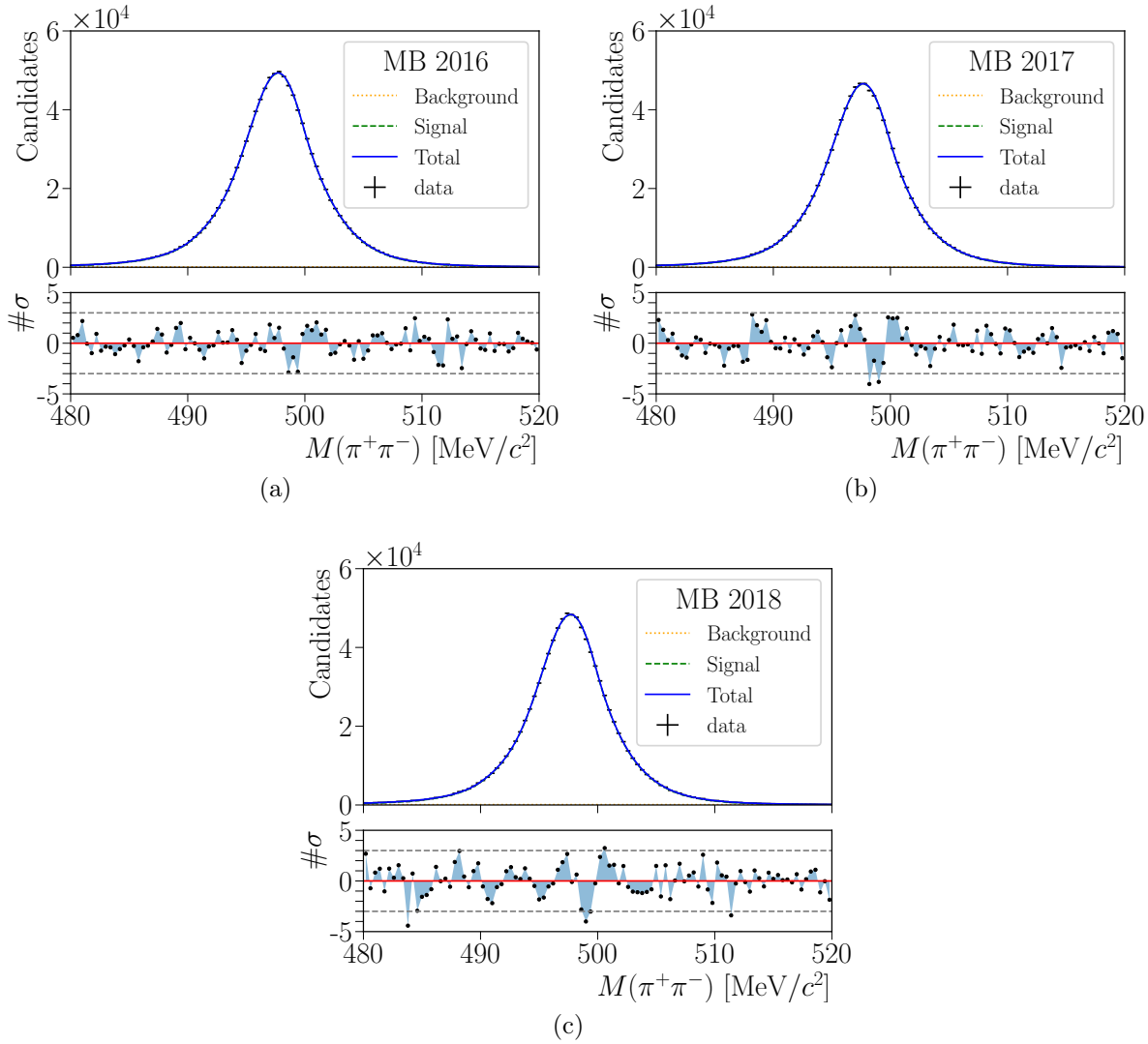

Figure 3.16: Results of the fits to the dipion invariant mass spectrum of $K^0_S \to \pi^+\pi^-$ candidates from MB data. Candidates satisfy the selection criteria excluding the requirements on the output of the ABDT classifiers.

Table 3.7: Values for the L0 TIS efficiency measured using simulated candidates of different decays.

Decay	**L0 TIS efficiency**
$K^0_S \to \pi^+\pi^-$ (MB)	$(18.0 \pm 0.1)\%$
$K^0_S \to \pi\mu\nu$ (MB)	$(19.8 \pm 1.9)\%$
$K^0_S \to \pi\mu\nu$ (forced)	$(13.2 \pm 0.2)\%$
$K^0_S \to \mu^+\mu^-$ (forced)	$(12.2 \pm 0.3)\%$

3.7.3 Trigger efficiencies from data

Using candidates from MB sample, it is possible to estimate the trigger efficiencies by using Eq. 2.3. The L0 TIS efficiency is assumed to be the same for $K^0_S \to \pi^+\pi^-$ and $K^0_S \to \mu^+\mu^-$, and can be extracted from $K^0_S \to \pi^+\pi^-$ data candidates. Unlike b or c hadrons, strange hadrons are produced in large quantities at LHCb. When generating simulated candidates from rare K^0_S decays, these are created independently of the multiplicity of the event, since there is almost always one K^0_S in it, which is forced to decay as requested. If we look at $K^0_S \to \pi\mu\nu$ from a MB sample (no decay is forced), then the probability of having one candidate after the selection requirements increases as it does the multiplicity, since the number of K^0_S hadrons in the sample becomes bigger. The number of candidates after the requirements is

$$n = N_{K^0_S} \times \mathcal{B} \times \varepsilon, \tag{3.30}$$

where $N_{K^0_S}$ is the number of K^0_S mesons in the event, $\mathcal{B}$ the branching fraction and ε the efficiency. For simulated MB, this expression would tend to reproduce what we observe in data. If the number of K^0_S increases, more of them will decay through the desired mode (it depends on the multiplicity). On the other hand, if one of the K^0_S mesons is forced to decay through the desired mode, the value $N_{K^0_S} \times \mathcal{B}$ is always equal or greater to one, biased with respect to the previous case. For decays with low branching fractions $\mathcal{B} \lesssim 10^{-3}$, this means that the product $N_{K^0_S} \times \mathcal{B}$ is almost always equal to one, independently of the multiplicity. This translates into a lower multiplicity for samples where one K^0_S meson is forced to decay through a certain mode, leading to a lower TIS efficiency. Hence the L0 TIS efficiency can not be calculated from MC, since forced signal decays have different multiplicities than those generated from MB. In Table 3.7, the values for the L0 TIS efficiency are compared for different decay modes. It can be seen that, whilst values are similar for $K^0_S \to \pi^+\pi^-$ and $K^0_S \to \pi\mu\nu$ when measured on the simulated MB sample, for the second it disagrees when the decay is forced. On the other hand, for $K^0_S \to \mu^+\mu^-$ and $K^0_S \to \pi\mu\nu$ efficiencies are closer, and they agree if the requirements in the selections applied to both decays are made more similar.

The L0 TIS efficiency is determined using $K^0_S \to \pi^+\pi^-$ data candidates from the MB samples

$$\varepsilon'_{\text{L0TIS}} = \frac{N^{\pi}_{\text{MB,selection,L0TIS}}}{N^{\pi}_{\text{MB,selection}}}. \tag{3.31}$$

Table 3.8: Number of observed $K^0_S \to \pi^+\pi^-$ candidates in MB data samples, before and after the L0 TIS trigger requirements, together with the measured efficiency. The last column contains the efficiencies corrected for the different thresholds per TCK. For 2018 the L0 trigger thresholds remained constant through the year.

	$N^{\pi}_{\text{MB,selection}}$	$N^{\pi}_{\text{MB,selection,L0TIS}}$	$\varepsilon_{\text{L0TIS}}$	$\varepsilon^{\text{corrected}}_{\text{L0TIS}}$
2016	1046988 ± 1170	121926 ± 393	$(11.645 \pm 0.039)\%$	$(11.556 \pm 0.059)\%$
2017	965636 ± 1095	109880 ± 367	$(11.379 \pm 0.040)\%$	$(11.173 \pm 0.060)\%$
2018	1003799 ± 1095	94452 ± 356	$(9.409 \pm 0.037)\%$	$(9.409 \pm 0.037)\%$

The number of $K^0_S \to \pi^+\pi^-$ candidates in the MB samples before N^{π}_{MB} and after $N^{\pi}_{\text{MB,L0TIS}}$ applying trigger requirements are obtained from fits to the dipion invariant mass distributions, using a double Crystal-ball PDF to describe the signal and an exponential for the background. The results for the fits with no trigger requirements and with the L0 TIS selection applied can be seen in Fig. 3.16 and Fig. 3.17, respectively. The measured efficiency must be corrected, since the trigger thresholds changed during data-taking. The different trigger configurations are stored with different TCKs. The corrected efficiencies are obtained from the number of observed candidates and the associated luminosity recorded with a given TCK

$$\varepsilon_{\text{L0TIS}} = \sum_{\text{TCK}} \frac{\mathcal{L}_{\text{TCK}}}{\mathcal{L}} \frac{N^{\pi}_{\text{MB,selection,TCK,L0TIS}}}{N^{\pi}_{\text{MB,selection,TCK}}}. \tag{3.32}$$

In Table 3.8 the number of observed $K^0_S \to \pi^+\pi^-$ candidates before and after the trigger requirements, and the corresponding efficiencies, for each year, can be seen. The L0 TIS efficiency has been measured to be very similar across the years and TCKs.

3.8 Systematic uncertainties

In addition to the propagation of statistical uncertainties, arising from the sizes of the samples, systematic uncertainties have been considered. The sources of systematic uncertainty are multiple, starting from the agreement between data and simulated candidates, determination of efficiencies and stability of the conditions across the years. Analyses with low statistics, aiming for discoveries of new particles or improvements on the limits of physical quantities, are more affected by statistics rather than by systematic uncertainties. These kind of uncertainties are accounted for as Gaussian constraints in the fit.

A set of systematic uncertainties affecting the overall normalization have been calculated. These include any systematic uncertainty for quantities not related to the ABDT binning of Eq. 3.25. In many cases, the $K^0_S \to \pi\mu\nu$ decay is used in order to estimate the associated systematic for data/MC discrepancies. $K^0_S \to \pi\mu\nu$ candidates are obtained from a similar selection to that used in the main analysis for $K^0_S \to \mu^+\mu^-$ and $K^0_S \to \pi^+\pi^-$. By looking at the invariant mass obtained from the reconstructed pion and muon, in Fig. 3.18 it can be seen that the spectrum is dominated by doubly-misidentified

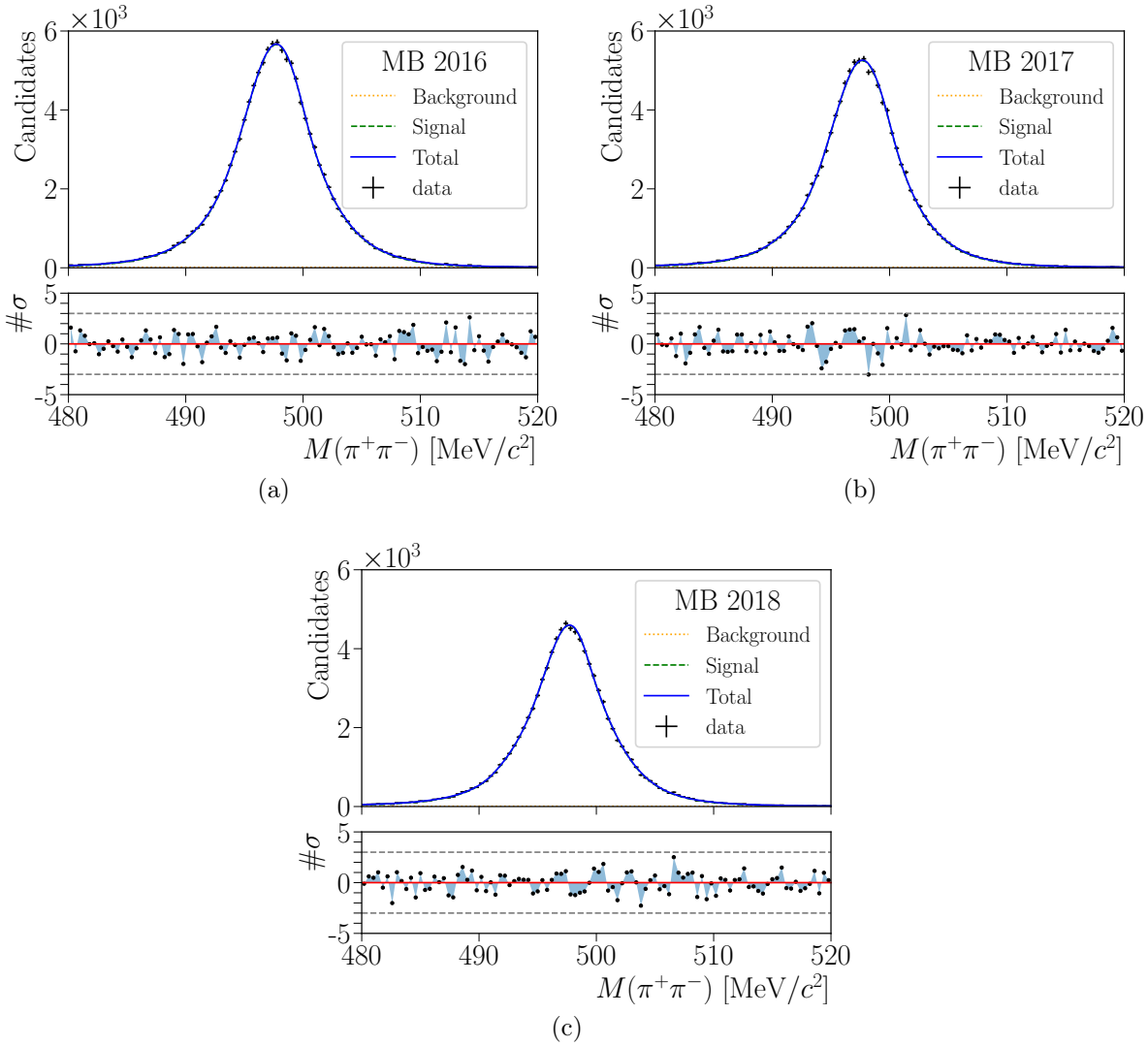

Figure 3.17: Results of the fits to the dipion invariant mass spectrum of $K^0_S \to \pi^+\pi^-$ candidates from MB data. Candidates satisfy the selection criteria excluding the requirements on the output of the ABDT classifiers, in addition to the L0 TIS requirements.

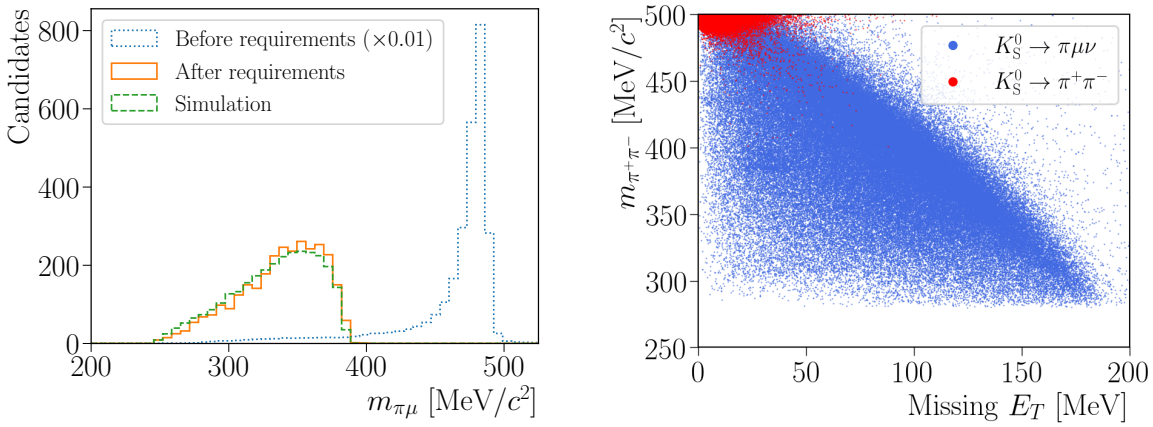

(a) (b)

Figure 3.18: Left: Invariant mass assuming the two reconstructed particles are a pion and a muon. Data $K^0_S \to \pi\mu\nu$ candidates before the requirements on the mass-related quantities described in the text are applied, are represented in dotted blue. This distribution has been downscaled by a factor 100, in order to make the others visible. In solid orange, the same distribution is shown after the requirements are applied. The dashed green line corresponds to simulated $K^0_S \to \pi\mu\nu$ candidates satisfying the previous requirements. Right: Dipion invariant mass as a function of the E_T^{miss} of simulated $K^0_S \to \pi\mu\nu$ and $K^0_S \to \pi^+\pi^-$ candidates.

$K^0_S \to \pi^+\pi^-$. However, the purity of the sample can be drastically increased by using the missing transverse energy (E_T^{miss}) of the pair. This quantity is calculated assuming the K^0_S is produced at its closest PV and the direction of flight is determined by the reconstructed SV. The E_T^{miss} is obtained from the projection of the sum of the momenta of the pion and the muon, in the plane perpendicular to the direction of motion of the K^0_S. Due to the conservation of momentum, if the K^0_S is produced in the PV this value would coincide with the transverse momentum carried by the outgoing neutrino. The $K^0_S \to \pi\mu\nu$ data sample is composed by candidates with a dipion invariant mass smaller than 400 MeV/c^2, and with a requirement $m_{\pi^+\pi^-} < (300 + (200 - E_T) \times 5/3)$ MeV/c^2.

The biggest source of uncertainty comes from the determination of the trigger efficiency, and its discrepancy with what was obtained from data in Sect. 3.7.3. The L0 TIS efficiency ratio has been validated at the level of ∼10%, whilst for xTOS, the checks using $K^0_S \to \pi\mu\nu$ decays show deviations ∼11%. At HLT, studies also with $K^0_S \to \pi\mu\nu$ concluded on a systematic of 13%. A big systematic uncertainty is assigned to the requirement on muon identification in the base selection (`IsMuon`), evaluated using data and simulated $J/\psi \to \mu^+\mu^-$ decays, to 4.3%. The determination of the efficiencies using the p_T-based weights from Sect. 3.2 includes an additional uncertainty of 5.1%, determined from the difference with respect to the efficiencies measured without weights. The usage of simulated samples in 2016 conditions to determine the efficiencies for the full Run 2 period has been taken into account with an additional systematic of 1%. Other sources of systematic uncertainties, like those arising from the variation of the $K^0_S \to \pi^+\pi^-$ yields in the fits for different models, the determination of s_{MB} or the uncertainty on $\mathcal{B}(K^0_S \to \pi^+\pi^-)$, have

contributions smaller than 1%. The systematic uncertainty affecting coherently to all bins is evaluated to be as high as 18%, being limited by the small size of the simulated samples.

For each bin of the ABDT classifier, additional systematic uncertainties have been calculated. The difference in the ABDT response between signal and control modes has been evaluated with and without the p_T-based weights from Sect. 3.2, as 3%. A systematic uncertainty has been assigned due to the requirement on the `muonIDPlusBDT` variable, and is evaluated to be between 1%, for the higher bins, and 11% for the lowest[4]. A study of the stability of the ABDTs responses, together with the L0 and HLT requirements through the years has also been done. For the offline selection, differences between 2016, 2017 and 2018 have been evaluated to 5%. At the trigger level, the associated systematic is evaluated to be between 1% and 5% for TIS bins, whilst it goes from 1% to 7% for xTOS. The final systematic uncertainties, associated independently to each bin, oscillate between 6% and 14%. This translates into a total uncertainty that takes values between 19% and 23%.

3.9 Fit to the dimuon invariant mass

In order to extract the limit on the new branching fraction, a fit to the dimuon invariant mass is done. The fit model is independent for each ABDT bin and trigger category, and can be expressed as

$$f_{b,c}(m_{\mu^+\mu^-};\hat{\theta}_{b,c},\hat{\phi}_{b,c},\hat{\psi}_{b,c}) = \alpha_c\beta_{b,c}\left[\frac{1}{\mathcal{B}(K^0_S\to\mu^+\mu^-)}S(m_{\mu^+\mu^-};\hat{\theta}_{b,c})+ \frac{\delta_{b,c}}{\mathcal{B}(K^0_L\to\mu^+\mu^-)}S(m_{\mu^+\mu^-};\hat{\theta}_{b,c})\right] + K(m_{\mu^+\mu^-};\hat{\phi}_{b,c}) + B(m_{\mu^+\mu^-};\hat{\psi}_{b,c}), \quad (3.33)$$

were the subscript b refers to each ABDT bin, and c to each trigger category. The function $S(m_{\mu^+\mu^-};\hat{\theta}_{b,c})$ corresponds to the signal PDF. An Hypatia distribution [112] is used to parameterize it. On the other hand the $K^0_L\to\mu^+\mu^-$ component, which is parameterized with the same shape as for $K^0_S\to\mu^+\mu^-$, is multiplied by additional factors $\delta_{b,c}$ that take into account the lower reconstruction efficiency for the $K^0_L\to\mu^+\mu^-$ decay with respect to that of the K^0_S meson. The background component is divided in two. The first parameterizes the doubly-misidentified $K^0_S\to\pi^+\pi^-$, and a power-law distribution of the form

$$K(m_{\mu^+\mu^-};m,n) = \frac{N}{(m_{\mu^+\mu^-}-m)^n}, \quad (3.34)$$

is chosen. The second parameterizes both the combinatorial background and the material interactions $B(m_{\mu^+\mu^-};\hat{\psi}_{b,c})$. In this case, an exponential distribution is chosen. The branching fractions of $K^0_S\to\mu^+\mu^-$ and $K^0_L\to\mu^+\mu^-$ are shared among all the ABDT bins and trigger categories. The factors related to the normalization are split between one common factor α_c and bin-dependent factors $\beta_{b,c}$. In Eq. 3.33, the values of α_c are constrained in the fit with a Gaussian of mean equal to one and a standard deviation that depends on the systematic uncertainties discussed in Sect. 3.8. The factors $\beta_{b,c}$

[4]The requirement on `muonIDPlusBDT` increases as the ABDT decreases.

correspond to the normalization factors of the signal PDFs, computed from the estimation of the efficiencies. The latter are also constrained, using the statistical and systematic uncertainties from Sect. 3.7 and Sect. 3.8. All these constraints are included as additional factors contributing to the likelihood. Taking $f'_{b,c}(m_{\mu^+\mu^-}; \hat{\theta}_{b,c}, \hat{\phi}_{b,c}, \hat{\psi}_{b,c})$ as the normalized version of Eq. 3.33, the likelihood is defined as

$$\mathcal{L} = \prod_{c}^{\text{TIS,xTOS}} \prod_{b=0}^{9} \prod_{i=1}^{N} f'_{b,c}(m_{\mu^+\mu^-}; \hat{\theta}_{b,c}, \hat{\phi}_{b,c}, \hat{\psi}_{b,c}) \mathcal{C}(\alpha_c) \mathcal{C}(\theta_{b,c}) \ldots , \tag{3.35}$$

where all the constraints $\mathcal{C}$, each one depending of a different parameter, multiply the value of the PDF.

The different background PDFs in Eq. 3.33 have their corresponding yields and normalization factors included. For those describing the K^0_{S} and K^0_{L} contributions, they only contain the normalization factors, since the values of the yields are ruled by the values of α_c, $\beta_{b,c}$ and the branching fractions, that are left to float in the fit.

Since the number of expected $K^0_{\text{S}} \to \mu^+\mu^-$ is close to zero, the parameters for the signal PDF must be determined from simulation and fixed for the final fit. The fact that simulation does not describe perfectly what one observes in data must be accounted for. This can be observed in Fig. 3.19, where the dipion invariant mass in simulation is displaced towards higher values compared to data in $K^0_{\text{S}} \to \pi^+\pi^-$ MB candidates. However, differences between simulation and data can be corrected by applying a small downscale $\sim$0.99939 to the daughters momenta in simulation. This downscale is computed matching the invariant mass distributions of $K^0_{\text{S}} \to \pi^+\pi^-$ candidates from simulation and data. In order to obtain the values of the parameters for the $K^0_{\text{S}} \to \mu^+\mu^-$ fit component, the momentum scale factor is applied to simulated $K^0_{\text{S}} \to \mu^+\mu^-$ candidates, and a maximum likelihood fit using the Hypatia PDF is done to the resulting dimuon invariant mass distribution. This process is repeated for each trigger category and ABDT bin. The results of the fits to the dimuon invariant mass can be seen in Appendix D. There are also differences between $K^0_{\text{S}} \to \mu^+\mu^-$ and $K^0_{\text{S}} \to \pi^+\pi^-$, as observed in Fig. 3.20, due to the difference in the reconstruction and selection between the two types of decay products, and due to the different kinematics. A systematic uncertainty is added to take into account any missing effect that could make the dimuon spectra behave differently in data and simulation. This uncertainty, evaluated to 4.3%, has been computed using simulated $K^0_{\text{S}} \to \pi^+\pi^-$ and $K^0_{\text{S}} \to \mu^+\mu^-$ candidates using the signal-to-background ratio obtained after unblinding.

The fit is done with Minuit [113], which is a widely used algorithm to minimize functions of an arbitrary number of parameters. A simultaneous maximum likelihood fit is done to the twenty bins of the dimuon invariant mass. The results for the four most sensitive bins are shown in Fig. 3.21. The full list of fits for all the categories can be found in Appendix E. The fit yields 34 ± 23 observed $K^0_{\text{S}} \to \mu^+\mu^-$ candidates, compatible with zero. The sensitivity with respect to the background-only hypothesis is 1.5σ. In order to calculate the limit, the posterior probability of the branching fraction is used. This is obtained by running successive fits to the dimuon invariant mass for fixed values of the branching fraction. The usage of the $\log \mathcal{L}$ profile might introduce a bias in the result, since fitting with a fixed value of the branching fraction can yield different results with respect to setting it free. In order to make sure that the profile is built properly, different

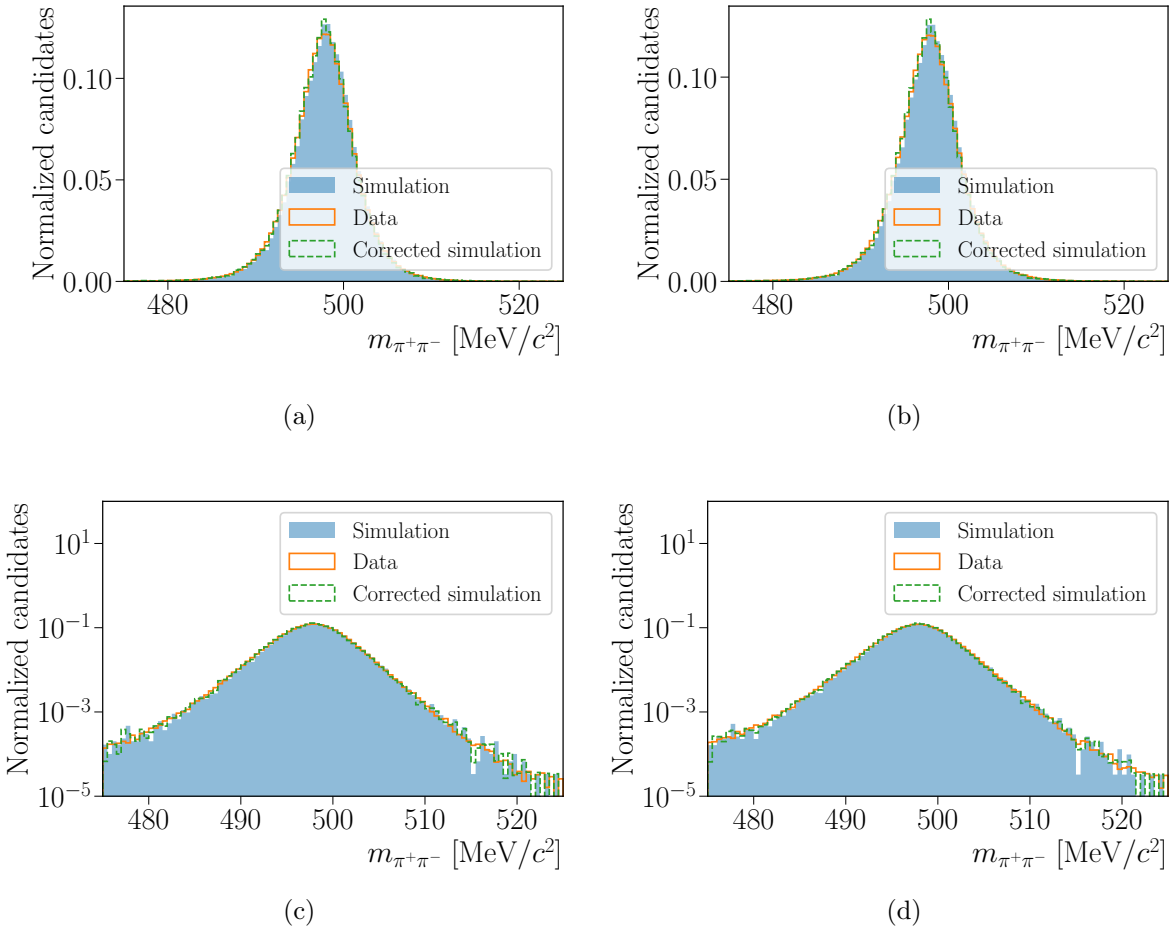

Figure 3.19: Top: Distribution of the two-body invariant mass for simulated (filled blue) and data (solid orange) $K^0_S \to \pi^+\pi^-$ candidates, together with the distribution of the latter after applying a downscale on the momentum of the decay products (dashed green). Candidates are asked to satisfy the minimum requirement on the ABDT classifier for the TIS (left) and xTOS (right) trigger categories. Bottom: Same plots as the previous but in logarithmic scale.

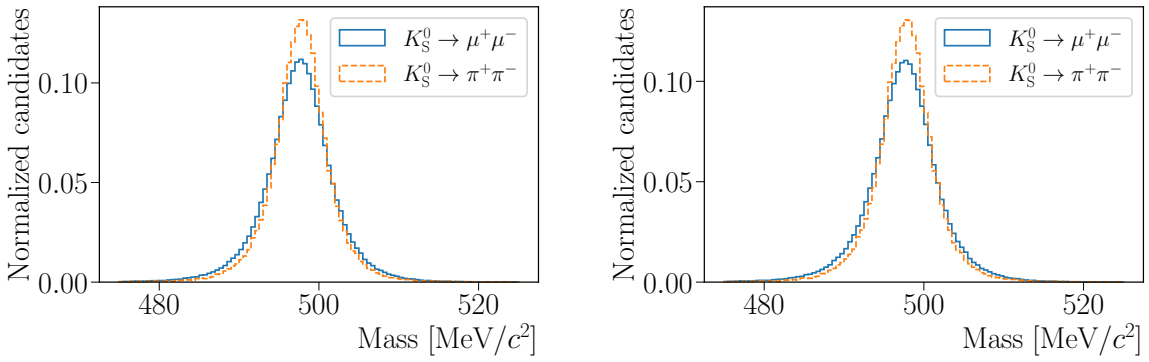

(a) (b)

Figure 3.20: Distribution of the two-body invariant mass for simulated $K^0_S \to \mu^+\mu^-$ (solid blue) and $K^0_S \to \pi^+\pi^-$ (dashed orange) candidates. Candidates are asked to satisfy the minimum requirement on the ABDT classifier for the TIS (left) and xTOS (right) trigger categories.

cases are considered, and the smallest value from all of them is used[5]:

- The $\log \mathcal{L}$ is built by letting the nuisance parameters of the fit model free to vary in wide ranges. The initial values are set to those from the main fit result.
- Similar to the previous, the process is repeated by setting the initial values to the modes of the marginal likelihood obtained with MultiNest [114]. This process serves to account for possible multiple relative minimums in the likelihood.
- The value of the parameter ruling the power of the $K^0_S \to \pi^+\pi^-$ component in Eq. 3.34 has shown to cause some instabilities when doing successive fits. In order to account for possible biases due to the behavior of this parameter, an additional profile is built fixing its value to that of the main fit result.
- For those bins where the amount of data does not allow to determine the slope of the background from material interactions or combinatorics, an additional profile is built setting the slope of the exponential to zero.

The logarithm of likelihood can be seen in Fig. 3.22, together with the previous result from Run 1.

3.10 Results and future prospects

The limit on the branching fraction of $K^0_S \to \mu^+\mu^-$ is calculated from Fig. 3.22, by transforming the likelihood into a probability and integrating it. Considering Run 2 data only, the integral of the probability yields a result

$$\mathcal{B}(K^0_S \to \mu^+\mu^-) < 2.2(2.6) \times 10^{-10} \text{ at } 90(95)\% \text{ CL} \tag{3.36}$$

[5]The smallest value of the $\log \mathcal{L}$ profile corresponds to the maximum probability of $\mathcal{B}(K^0_S \to \mu^+\mu^-)$, and gives a conservative result.

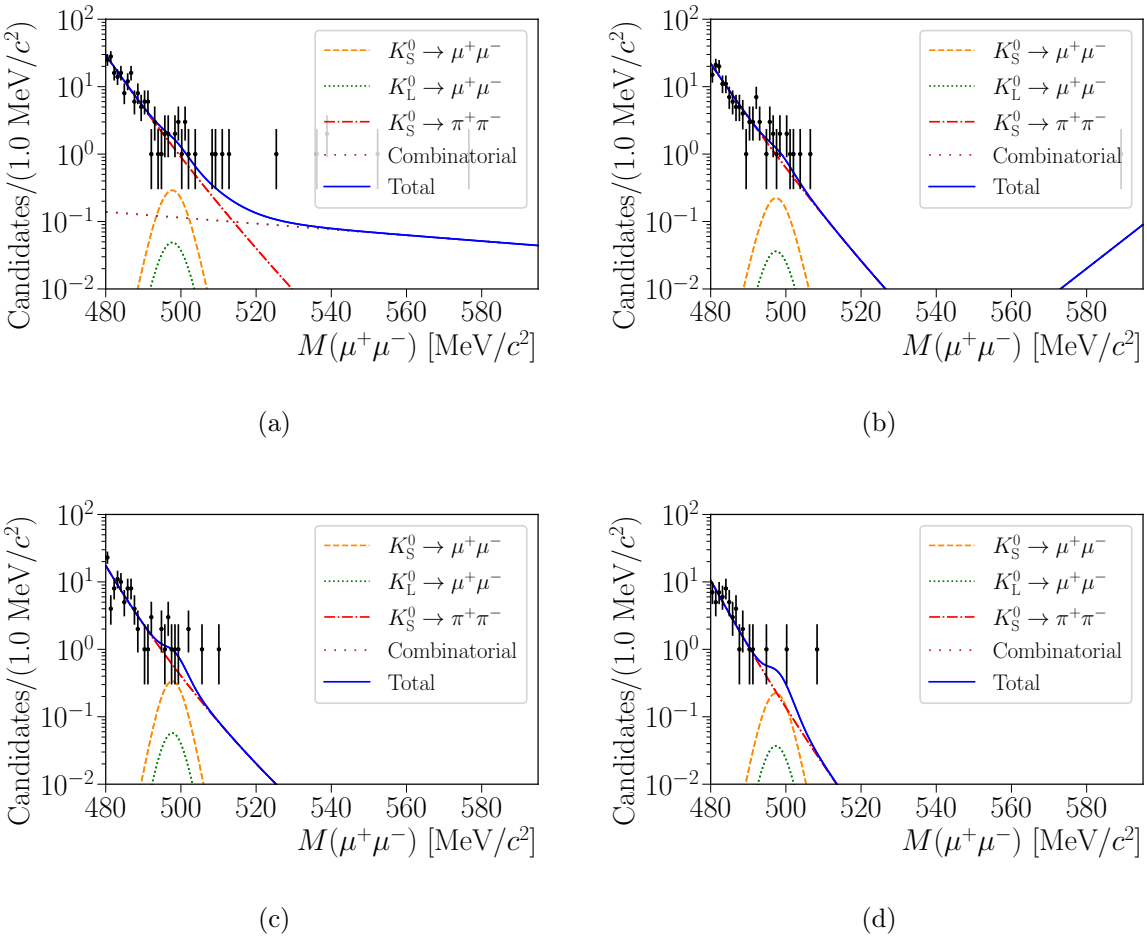

Figure 3.21: Projection of the fit to the dimuon invariant mass distribution for (left) two TIS and (right) two xTOS ABDT bins. These bins correspond to the ABDT response with the biggest signal-to-background ratio (increasing from top to bottom). The spectra are dominated by doubly-misidentified $K^0_S \to \pi^+\pi^-$ decays.

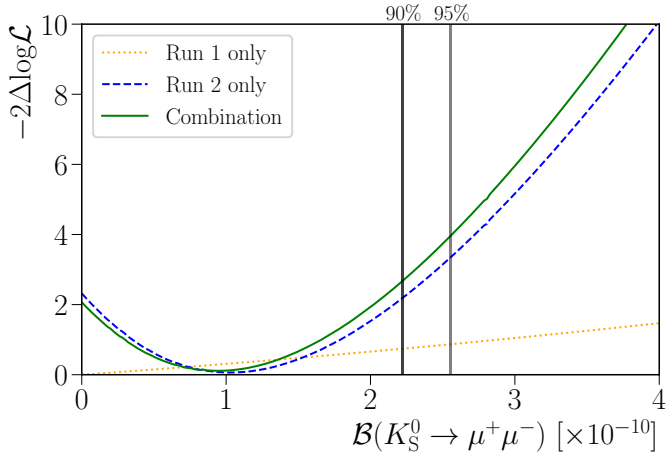

Figure 3.22: Logarithm of the likelihood for the branching fraction of $K^0_S \to \mu^+\mu^-$, obtained by running fits for fixed values of $\mathcal{B}(K^0_S \to \mu^+\mu^-)$.

Combining the likelihood with that from the Run 1 gives

$$\mathcal{B}(K^0_S \to \mu^+\mu^-) < 2.1(2.4) \times 10^{-10} \text{ at } 90(95)\% \text{ CL} \tag{3.37}$$

which is, to-date, the world best limit on the branching fraction of this mode, and one of the lowest set by the LHCb collaboration in any decay.

An additional fit was run interpreting the result as a measurement of $\mathcal{B}(K^0_L \to \mu^+\mu^-)$ at LHCb. The $K^0_S \to \mu^+\mu^-$ component was removed from the fit, and the yield corresponding to the K^0_L decay was set unconstrained. The branching fraction was measured to be

$$\mathcal{B}(K^0_L \to \mu^+\mu^-) = 5.0^{+3.2}_{-2.9} \times 10^{-8} \tag{3.38}$$

with a significance of 1.6σ with respect to the background-only hypothesis.

The new limit on $K^0_S \to \mu^+\mu^-$ will allow to set more stringent constraints to supersymmetric and leptoquark models, and consolidates the power of LHCb to study strange decays. The Upgrade of the LHCb detector constitutes a more promising environment. Luminosity is expected to increase from 4×10^{32} cm^{-2}s^{-1} to $2 \times 2 \times 10^{33}$ cm^{-2}s^{-1}, collecting 50 fb^{-1} at the end of Run 4. On the other hand, the removal of the L0 hardware trigger, constituting nowadays the main bottleneck for the study of strange decays at LHCb, will remove the limitations on the efficiency for $K^0_S \to \mu^+\mu^-$. In the ideal case, the performance of the trigger could be very similar to the current offline selection. This would mean an efficiency of $\mathcal{O}(10^{-3})$, increasing it by two orders of magnitude. Extrapolating from the current result and assuming zero background in the signal region, the branching fraction limit can be brought down to $\mathcal{O}(10^{-11})$, one order of magnitude above the SM prediction. The challenge relies on being able to control the backgrounds, mainly $K^0_S \to \pi^+\pi^-$, and on reducing the systematic uncertainties. The absence of clear control samples for the determination of the trigger and muon identification efficiencies is one of the main issues to study this decay. For the Upgrade, dedicated trigger lines to select $\rho \to \mu^+\mu^-$ and $\phi \to \mu^+\mu^-$ could be used for the calibration of the muon identification. In order to reduce the systematic uncertainty on the trigger efficiencies, the requirements on

the detachment of the K_S^0 decay vertex will make the performance of the trigger lines be worse for ρ and ϕ decays. Studies will more likely need to use $K_S^0 \to \pi\mu\nu$, as was done in this analysis, applying muon identification requirements to the pion.

The LHCb detector will operate till the end of the Run 4 of the LHC, which is scheduled for 2030. The physics case for a Phase-II Upgrade of the detector has been presented [115], but is still pending to be resolved. In this hypothetical scenario, with 300 fb^{-1} accumulated in tape, LHCb could aim to reach the SM sensitivity for $K_S^0 \to \mu^+\mu^-$. The SM prediction for its branching fraction is expected to be improved, reducing the current uncertainties $\mathcal{O}(30\%)$ and being able to put stringent constraints to SM parameters and NP models.

4

Fast reconstruction techniques for muons in the Upgrade of the LHCb detector

The upgrade of the LHCb detector will finalize for the start of the Run 3 of the LHC. After the Long Shutdown (LS) 2, luminosity is expected to increase by a factor 5, going from 4×10^{32} cm^{-2}s^{-1} to 2×10^{33} cm^{-2}s^{-1}. Due to the high fluency of particles in the subdetectors, different improvements had to be applied in order to maintain the current detector performance. Profiting from the experience obtained in Run 1 and Run 2, the readout system and DAQ will also be changed. This applies also to the trigger, where different modifications must be done in order to keep covering the current LHCb physics program. A special case is strange decays, due to the challenge of reconstructing particles with very low p_T at such higher luminosity conditions. The ideas discussed in Sect. 2.2.4, used in the Run 2 of the LHCb detector, are being ported to the upgrade, and the current performance in this new environment will be presented here.

The different upgrades are shown in Table 4.1, together with the luminosity that is expected to be collected per run of the LHC. The LHC will be modified in order to run in high-luminosity conditions for the start of Run 4. The upgrades of the ATLAS and CMS detectors will take place for the start of this data-taking period, where they will be running in different conditions compared to Run 3. However, the role of the LHCb detector in a high-luminosity environment has not been approved yet, and in Run 4 it will operate at a similar instantaneous luminosity to that of Run 3. Several documents have been presented [71–73, 116], reporting the physics case and the impact that the measurements from the experiment can have. It must be mentioned that in Run 4 an overlap between two luminosities, different for LHCb with respect to ATLAS and CMS, will take place. This will have a negligible impact in the experiments since the LHC can be tuned to provide specific luminosities at each collision point.

Since at the time of writing this document the final design of the upgraded LHCb detector has not been established, more modifications are expected to be implemented before the start of data-taking, so algorithms and performances showed here must be considered as preliminary.

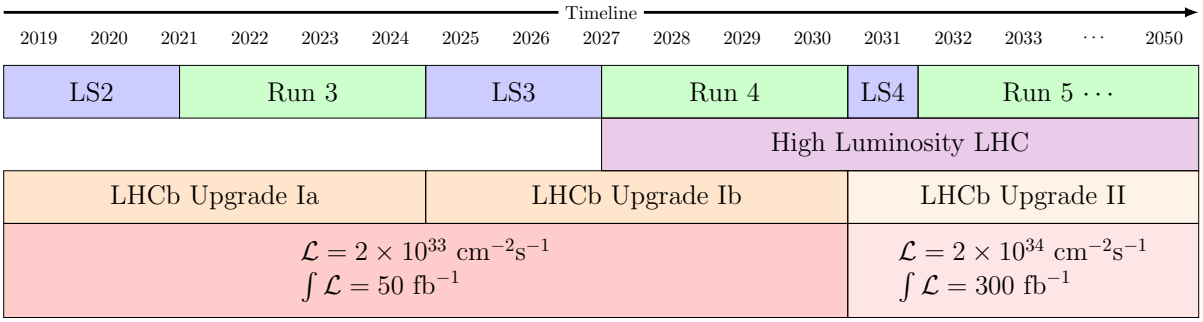

Figure 4.1: Scheme of the expected schedules for the upgrades of the LHCb detector, together with the instantaneous luminosity at nominal operation and the expected integrated luminosity. Modifications done to the LHCb detector are not synchronized with those from CMS and ATLAS, who will experience their major improvements for the operation start of the high-luminosity LHC. The LHCb experiment will take data with the high-luminosity LHC during Run 4, but with the same conditions as for Run 3. The role of the LHCb experiment on a high-luminosity environment has not been approved yet.

4.1 The Upgrade of the LHCb detector

Several challenges arise from the big increase in luminosity for the upgrade of the LHCb detector. The high fluency of particles through the tracking subdetectors makes the improvement of the tracking stations mandatory in order to maintain the current invariant mass, SV and IP resolutions. The granularity of the VELO, TT, ST and OT must be increased, so these detectors will be replaced by their upgraded versions [117]. On the other hand, the material budget will be reduced, in order to increase the radiation length of the devices. The VELO will be based on silicon pixel detector modules cooled using liquid CO_2 [118]. This subdetector will become closer to the beam pipe, narrowing its aperture from 5.5 mm in Run 2 to 3.5 mm, improving the IP resolution. The current TT will be replaced by the Upstream Tracker (UT), based also in silicon strips, but with a reduced thickness, finer granularity and improved coverage. The current ST and OT will be replaced by the SciFi, composed of scintillating-fibers.

The rest of the subdetectors will almost remain unchanged. The current performance on particle identification can be preserved by replacing the Hybrid Photo-Detectors (HPDs) by multi-anode photomultipliers (PMTs) in the RICH systems, and reducing the gain of the PMTs in the calorimeters. The different components of the remaining subsystems will be replaced by newer ones, due to the radiation damage suffered in Run 1 and Run 2. The scheme of the upgraded LHCb detector can be seen in Fig. 4.2.

The major change in the LHCb detector concerns the readout and trigger system. One of the current limiting factors in the physics program of the LHCb collaboration is the L0 trigger detector. This stage of the trigger, based in hardware and with high p_T and E_T signatures, becomes highly inefficient for many studies. As an example, in this work it has been shown the necessity of lowering the p_T thresholds of muon reconstruction to study strange decays, but it becomes also a necessity for searches for long-lived particles, for example. The L0 trigger from Run 2 is not only inefficient due to the requirements in p_T or E_T, but also due to its rigid structure. Its design makes it very hard to customize and

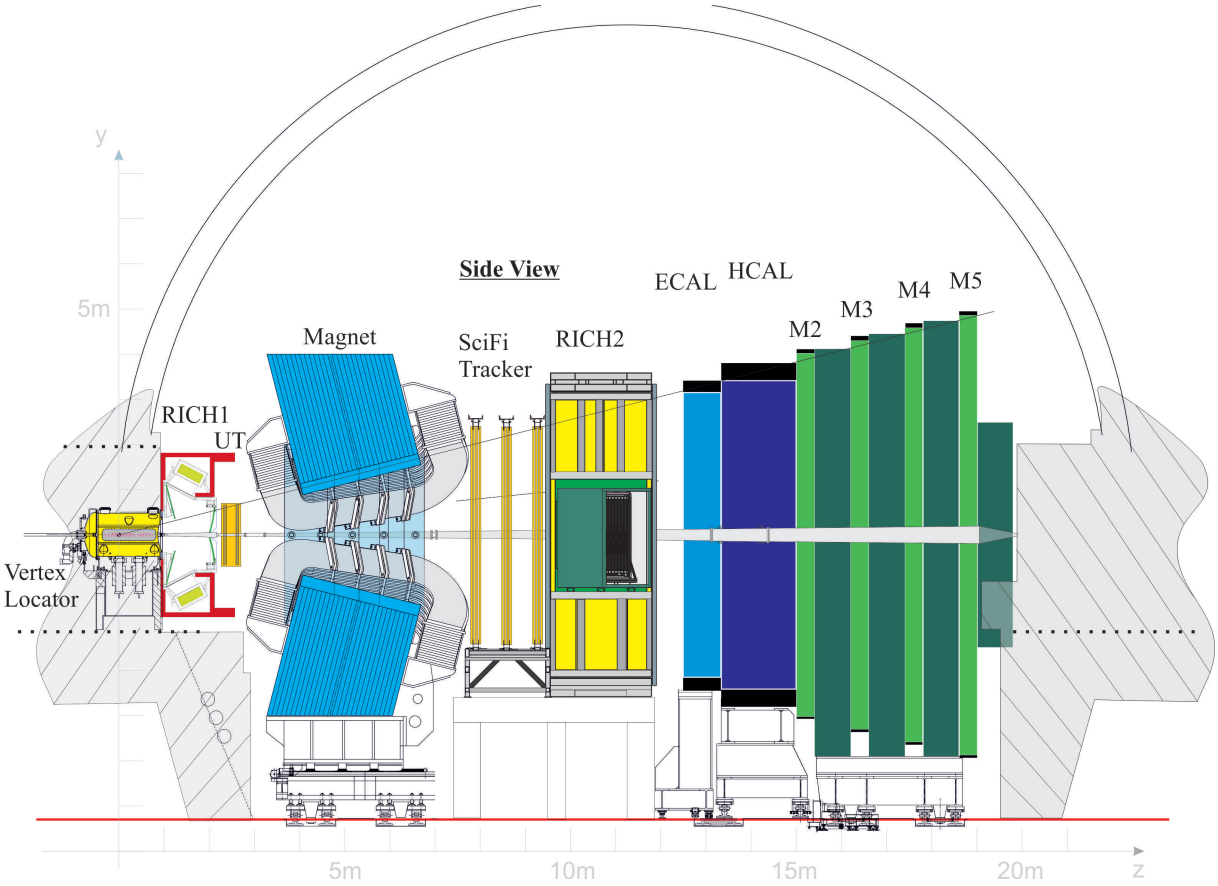

Figure 4.2: Layout of the LHCb detector in the upgrade. The major changes are present in the tracking subdetectors, with improved versions of the VELO, TT, ST and OT subsystems. The readout electronics and front-end (FE) are also changed, in order to process 30 MHz of events with no hardware trigger.

adapt to new necessities of the collaboration. In order to have a more flexible environment, and to be able to adapt the detector to the needs of the experimentalists, it was decided to drop the L0 trigger and keep a full software trigger. The challenge consists on processing the incoming bunch-crossing rate of 30 MHz, in such a way that only 2 to 5 GB/s are written to disk. To do so, the upgraded software trigger is expected to be composed by two different levels:

- **HLT1**: Similarly to the HLT1 trigger in Run 2 (see Sect. 2.2.3), at this level a full reconstruction of the event will be done. Selections based on the topology of the decays will be included, where any tracking-related quantity (PV, SV, IP, track quality, ...) will be available. Simple particle identification for muons will also be present, since processing the information from the RICH would not fit into the timing constraints.

- **HLT2**: Using data from the HLT1 stage, a full online detector alignment and calibration will be done. Selections will profit from the offline precision in particle identification and track quality. Current offline selections can be implemented at this stage.

In order to comply with these stringent requirements, the readout system of the different subsystems will be changed. Furthermore, the different trigger stages will be composed by several exclusive and inclusive selections. The large amount of data expected for some decays, like for calibration or charm studies, forced the LHCb to adopt an smarter data-taking procedure. Already for Run 2, in order to collect large quantities of certain decays like $D^0 \to K^-\pi^+$, for example, it was decided to keep only the information needed, dropping most of the raw event in the process. This allows to increase the number of candidates that are persisted, but forces analysts to be very careful and determine beforehand the quantities that they want to compute and which parts of the events they want to persist, since the rest will be later removed and be irrecoverable. This strategy, known as Turbo [119], constitutes a new approach for data-taking in many well-studied modes, or studies where the analysis strategy is very well known. Most of the exclusive lines for the LHCb upgrade are expected to follow this procedure. On the other hand, the trigger will contain several inclusive selections. There are several reasons to maintain this configuration, starting from the fact that from the point where a proposal for a new measurement is set, till the data to do the analysis is collected, some years can elapse. Having inclusive lines would allow to do preliminary studies and even perform first measurements of these new quantities. For those analysis where the strategy is not completely established, or where new considerations must be taken due to the increase of the sensitivity, they would allow provide a more versatile sample since any quantity can be computed from the event.

For strange decays, the upgrade trigger will more likely be composed also by a mixture of inclusive and exclusive selections. Studies like $K^0_S \to \mu^+\mu^-$ or $\Sigma^+ \to p\mu^+\mu^-$ could be done using exclusive selections whilst others, like $K^0_S \to \pi^0\mu^+\mu^-$, $K^\pm \to \pi^\pm\mu^+\mu^-$ or $K^0_S \to \ell^+\ell^-\mu^+\mu^-$, will probably be done using the inclusive trigger lines due to the lack of experience studying these modes. For many analyses, the no-bias stream will also be helpful due to the possible absence of requirements at the reconstruction level, providing normalization samples for many analyses (like $K^0_S \to \mu^+\mu^-$) and allowing to do other interesting measurements.

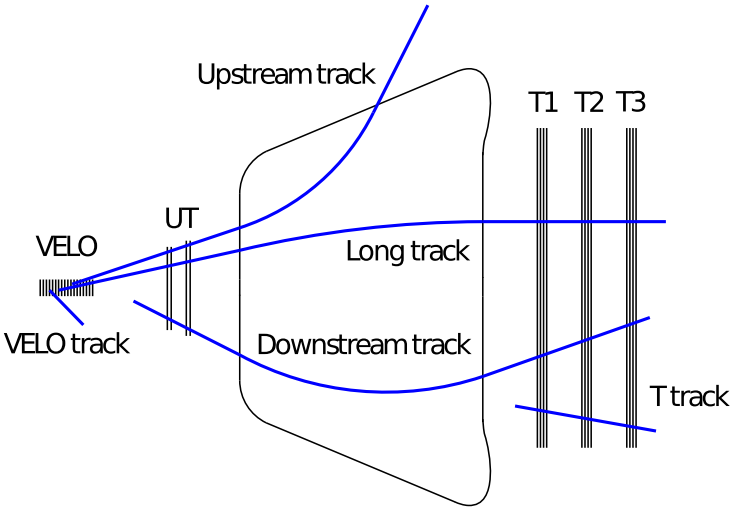

Figure 4.3: Scheme of the different track types present at LHCb. Most of the analyses make use of long tracks, with the information from the whole detector. Some special cases require the use of *Upstream* or *Downstream* tracks, whilst T-tracks and VELO tracks are oftenly reserved for more technical needs, like PV-finding or alignment and calibration purposes.

4.2 The tracking sequence in the upgrade

At LHCb, five different types of tracks are defined depending on the associated information from the subdetectors. A scheme showing the definition of the different track types can be found in Fig. 4.3. Tracking at LHCb starts by processing the information from the VELO. In the upgrade, this subdetector is made of different layers of silicon pixel detectors composed by two different stations. Pattern recognition starts by looking for pairs of unused hits on neighboring stations. Hits are required to satisfy $|dx/dz| < 0.4$ and $|dy/dz| < 0.4$, related to the acceptance of the subdetector. Track candidates are extrapolated in the upstream direction, and any closest hit within a search window is added if it satisfies a requirement on the maximal scattering angle. The upgraded VELO has a better performance than the version used in Run 2, increasing the reconstruction efficiency from 95–99% to 99% as measured with $B^0 \to K^{*0}\mu^+\mu^-$ decays, with a reduction of the ghost rate by a factor 2.48. More details about VELO tracking can be found in Ref. [118].

VELO tracks are then extrapolated to the UT in order to create *Upstream* (VELO-UT) tracks. This is done by extrapolating VELO tracks to the z-position at the center of the UT. Only hits that would satisfy $p > 3$ GeV/c and $p_T > 0.5$ GeV/c are selected. These are later clustered to form candidates, consisting on at least three UT hits on at least three UT layers with no more than one hit per layer. Each cluster is combined with the original VELO track, promoting it to *Upstream*. A fit is later performed and the best combination of VELO tracks and UT clusters is selected based on the number of hits on the track candidate and the χ^2 of the track fit. This procedure is different from what it was done for Run 1 and Run 2, where VELO tracks were directly extrapolated to the ST and OT. The information from the TT was later included in order to improve the quality of the long tracks. By using the UT information earlier in the reconstruction, the time of

processing an event and the ghost rate is reduced by a factor of three with a 1.5% loss in efficiency. More details on the *Upstream* tracking algorithm and its performance can be found in Ref. [120].

The Forward tracking algorithm is based on a Hough transformation approach[1]. *Upstream* tracks are used as an input, and they are promoted by searching for matching hits in the SciFi. This subdetector is composed by x-layers, arranged vertically, and u/v-layers, where the fibers are tilted by $\pm 5°$ with respect to the previous. The VELO track plus one additional x measurement in the SciFi after the magnet define the trajectory of the candidate. Projecting this trajectory on a reference plane, the closest hits in the x-layers constitute the input for a Hough cluster. For each identified Hough cluster a track candidate is formed. A simplified fit is used to remove outliers, and if the candidate is composed by a minimum number of hits, then a similar search in the u/v-layers is done. The additional hits are kept depending on a requirement on the χ^2 computed from successive fits to all the hits associated to the candidate. A Kalman fit is later applied, improving the quality of the track. The timing of the forward algorithm is proportional to the number of *Upstream* tracks and the number of hits in the SciFi stations. This is of relevance to process tracks with low p_T, justifying the use of special algorithms for specific processes, as will be discussed in Sect. 4.3. Tracks that can not be forwarded are also kept, since they can be of high importance in some analyses involving soft particles like for example, those using c-tagging with $D^{*+} \to D^0\pi^+_{\text{soft}}$ due to the low energy of π^+_{soft}. In addition, an algorithm uses hits in the SciFi station to make T-tracks and promote them to long tracks by matching them to VELO tracks. A Kalman fit is run afterwards, and a clone-killing algorithm removes duplicated tracks or badly reconstructed tracks based on the associated hits and the χ^2. The set of long tracks used later on in the analyses is composed by the combination of these two sets. More details on the *Forward* pattern recognition algorithm and its performance can be found in Ref. [121].

Many of the decays studied at LHCb involve Λ baryons or K^0_S mesons. Due to the larger lifetime of these particles, the tracking efficiency of the decay products is drastically reduced due to decays outside the VELO. An special algorithm uses information from the UT and SciFi in order to reconstruct such particles. The resulting tracks are referred to as *Downstream* tracks. These are constructed by extrapolating the SciFi tracks to the UT. However, the algorithm used in Run 1 and Run 2, described in Ref. [122], is too slow to be used in the upgrade. This is mostly due to the higher occupancy of the UT detector in the innermost region. The final procedure to build this kind of tracks is still to be established for the upgrade.

4.3 Fast reconstruction of muons in the Upgrade

Reconstruction of particles at low p_T is the most challenging aspect to study strange decays in the upgrade. As it happened in Run 2, tracks other than muons with small transverse momentum will not be processed due to the big decrease of the throughput of the HLT1. However, due to the lower occupancy of the muon chambers with respect to other subdetectors (see Fig. 4.4), a similar strategy to that showed in Sect. 2.2.4 for Run 2

[1]This is a technique commonly used in image analysis and it has been widely adapted for tracking purposes in particle detectors.

can be adopted. This idea was ported to the upgrade framework of the LHCb detector, but including some modifications in order to improve its performance.

In the main reconstruction chain discussed in Sect. 4.2, the throughput is mostly limited by the process of extrapolating the VELO-UT tracks through the magnet region, including the information from the SciFi. Creating forward tracks from VELO-UT tracks while maintaining low p_T thresholds becomes possible if one includes the information from the muon chambers early in the reconstruction chain. Instead of processing the hits in the SciFi, one can directly extrapolate the VELO-UT tracks to the muon chambers, and do a fast muon identification with the hits found in it. The decision whether the input tracks must be kept or not can be decided by the distribution of the hits in the muon stations, so the number of tracks being preserved is drastically reduced. This would force the LHCb to run with at least two different reconstruction chains, one processing any kind of particle satisfying the thresholds imposed by the tracking system, and another focused exclusively for muons where the p_T can go closer to the acceptance threshold of $\sim$80 MeV/c. By looking directly at the muon chambers, a loss in sensitivity is expected, since the extrapolation is not as accurate as if the information from the SciFi was used. In addition, muons suffer from multiple-scattering in the RICH2, ECAL, HCAL and muon stations, distorting the position of the hits in the muon chambers. For these reasons, although this algorithm could be used in any kind of analysis, for the case of heavier particles, like b or c hadron decays, this can result in a loss of sensitivity, since for these particles most of the muons satisfy the p_T requirements. A better performance would be achieved by following the default reconstruction chain, and applying the standard muon identification algorithms afterwards.

4.3.1 The VELO-UT muon matching algorithm

The workflow of the algorithm can be easily understood by looking at Fig. 4.5. The algorithm starts with VELO-UT tracks, which have an estimate of the momentum with a resolution $\sim$15%. This is achieved thanks to the remnant of the magnetic field inside the UT subdetector. Considering a constant magnetic field in the magnet region, its effect is approximated by a kink, where the magnet focal plane (the deflection point) is given by

$$z_f = a - b \cdot t_x^2, \tag{4.1}$$

where t_x is the slope of the track measured by the VELO[2]. The values of $a = 5298.09$ mm and $b = 849.31$ mm are obtained from a fit to the profile of the intersections of the VELO and SciFi track segments, as seen in Fig. 4.6a. The slopes of the track after the magnet are determined by a relation with the momentum of the incoming particle, which follows

$$|\Delta t_x| = \frac{\alpha}{p - \beta}, \tag{4.2}$$

and as can be seen in Fig. 4.6b. The fit shows that the best values are $\alpha = 1236.59$ MeV/c and $\beta = 311.84$ MeV/c.

Once the deflection of the track is determined, a search for hits is done in the muon chambers. The muon stations to look at are defined by the momentum of the input

[2]By doing this there is no distortion due to the effect of the magnetic field in the UT.

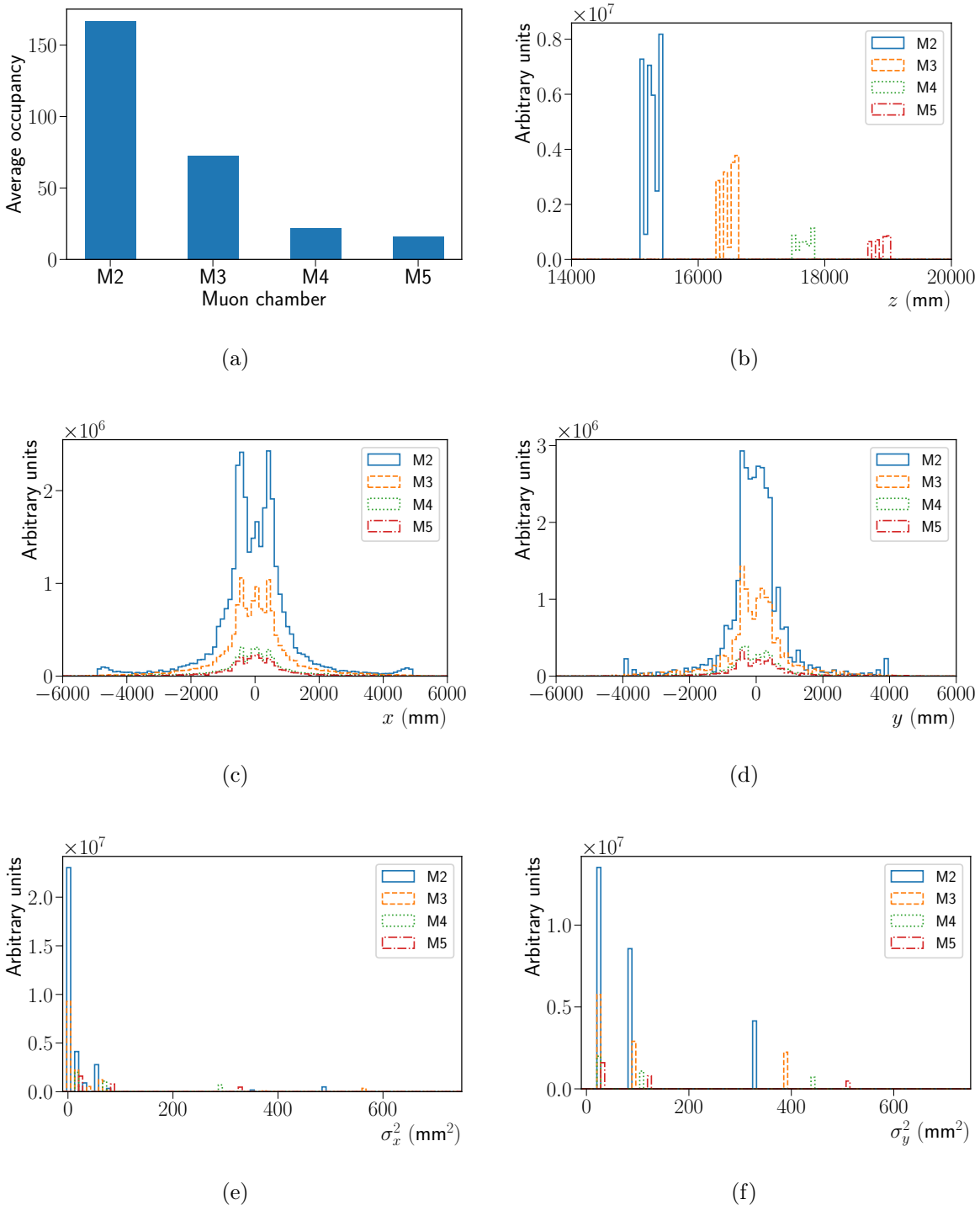

Figure 4.4: Occupancy of the different muon chambers obtained from simulated proton-proton collisions in upgrade conditions, and distribution of hits in the different coordinates together with their associated variances.

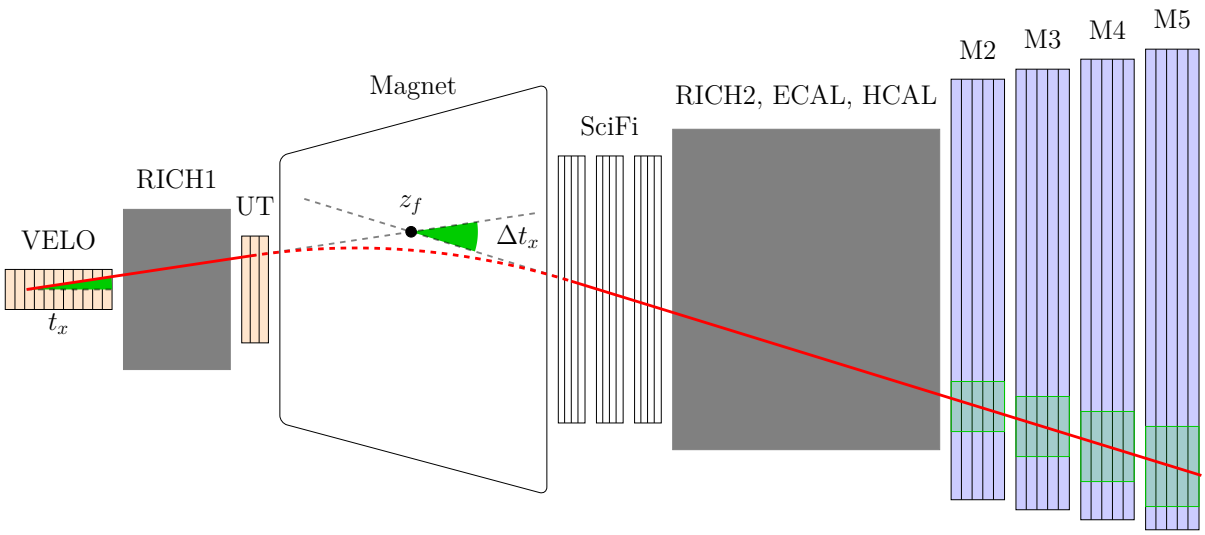

Figure 4.5: Scheme of the VELO-UT muon matching algorithm. Subdetectors used by the VELO-UT muon matching algorithm are highlighted in color. The LHCb detector has been simplified, and it is not to scale.

particle, following a similar procedure to what has been done offline for Run 2. Muon hits are composed by tiles, and can be divided in two different categories depending whether they are made of crossed or uncrossed tiles. A hit formed from two crossed tiles will have a more accurate measurement of the position in x and y, since it can be assumed that the particle has traveled close to the intersection point. In this algorithm both crossed and uncrossed hits are considered, since the uncertainty on the position will have an impact in the χ^2 of a fit to the hit positions. The momentum bounds are lowered by ∼20% on average with respect to similar offline Run 2 algorithms due to the worse momentum resolution of the input tracks. The sizes of the FoIs in the different muon stations are determined from simulation, in such a way that the amount of tracks that are not muons is drastically reduced. A summary of the requirements on the muon stations with hits and the bounds defining the FoIs are displayed in Table 4.1. If hits are found that satisfy the requirements imposed by the momentum of the input track, the track is considered to pass the algorithm if the χ^2/dof obtained from a fit to the position of the hits and the magnet focal plane is smaller than 20. By processing a simulated sample of proton-proton collisions in upgrade conditions, the algorithm achieves a purity of 2.1% with a ghost rate of 14%, to be compared with the values from the *Upstream* reconstruction: 0.1% and 11%, respectively. The number of tracks to be processed by the *Forward* tracking is reduced by a factor of 34. Efficiencies for particular decays will be treated in more detail in Sect. 4.3.2. This algorithm, called `MuonMatchVeloUT`, constitutes the major improvement for the upgrade in order to keep the current LHCb performance for strange decays. All HLT1 lines for this type of decays involving muons are expected to make use of the algorithm, with a reconstruction chain that will differ with respect to that for c and b hadron studies.

Muon chambers are tracking chambers with dense shields in front of them in order to prevent particles other than muons to generate hits. They can be used as an additional subdetector in order to improve the reconstruction of *Upstream* tracks. This leads to a

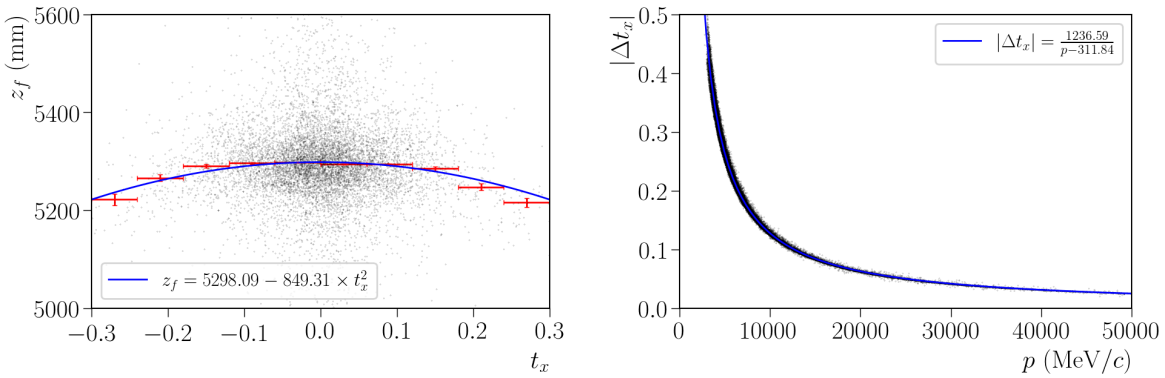

(a) (b)

Figure 4.6: Left: Distribution of the intersection points of the VELO and SciFi track segments for simulated particles. The profile is shown in red, together with the fit to Eq. 4.1. Right: Distribution of the variation of the slope, computed from the VELO and SciFi track segments, as a function of the momentum of the particle. The fit to Eq. 4.2 is displayed in blue. The plots have been obtained from simulated proton-proton collisions in upgrade conditions.

better estimation of the momentum of the particle, and also its charge. In tracking, the value that is usually updated corresponds to the ratio of these two quantities, namely q/p. By choosing the combination of hits that leads to the smallest χ^2 in the fit, the slope in the muon chambers can be evaluated. Considering that this slope is the same as that in the SciFi, Eq. 4.2 can be used in order to obtain the value of q/p from the difference in the slope Δt_x and the magnet polarity. In Fig. 4.7, the difference in resolution for simulated muons can be seen. In general *Upstream* tracks have, in average, an overestimated momentum, an effect that is enhanced for lower momentum values.

One of the current limitations of the algorithm has to do with the track extrapolation at low p_T, as can be seen in Fig. 4.8. This is more likely due to the worse resolution of the *Upstream* tracks in this region. A better estimation of the momentum, as well as a different extrapolation method including other variables, like the slope in the y axis or a dependence on the momenta would allow to improve the performance.

4.3.2 Studies for $K_S^0 \to \mu^+\mu^-$

A dedicated sample in upgrade conditions of $K_S^0 \to \mu^+\mu^-$ was created in order to evaluate the performance of the algorithm described in the previous section. To get access to the maximum efficiency for strange decays, a dedicated LHCb reconstruction sequence has been configured to run with the most relaxed requirements possible. A minimum p_T of the tracks was set to 80 MeV/c, due to acceptance requirements, and a minimum momentum of 2.5 GeV/c has been considered since the algorithm does not work for tracks with lower momentum[3]. Three different scenarios have been considered:

[3] This requirement, as explained in Sect. 4.3.1, is established due to the fact that for smaller momenta the majority of the muons do not survive to generate hits in the muon stations.

Table 4.1: Definition of the parameters for the search of hits in the muon stations.

Momentum (GeV/c)	**Muon stations**
$[2.5, 7]$	M3 and M2
$[7, 12]$	(M4 or M5), M3 and M2
> 12	M5, M4, M3 and M2
Muon station	**Station bounds $[x, y]$ (mm)**
M2	$[500, 400]$
M3	$[600, 500]$
M4	$[700, 600]$
M5	$[800, 700]$

- `Default`: The reconstruction sequence from Sect. 4.2 runs with no modifications apart from the requirements described above. The reconstruction path starts at the VELO after which *Upstream* tracks are created. These are finally promoted to *Forward* after extrapolating them through the magnet region to the SciFi.

- `MuonMatch`: In this case the `MuonMatchVeloUT` algorithm runs before forwarding the tracks through the magnet region. The algorithm acts only as a filter for the *Upstream* tracks, reducing the amount of them that need to be forwarded.

- `MuonMatch` setting q/p: Similarly to the previous mode, in this case the difference is that the best combination of hits is used to improve the momentum of the incoming *Upstream* track, as described in Sect. 4.3.1.

In Fig. 4.9, the dimuon invariant mass for the simulated $K^0_S \to \mu^+\mu^-$ candidates is shown for the different scenarios. The efficiency of the *Forward* tracking for *Upstream* tracks from $K^0_S \to \mu^+\mu^-$ decays in the standard reconstruction sequence is measured to be 72%, whilst using the `MuonMatchVeloUT` algorithm it goes down by a factor of 1.64, acquiring a value of 44%. It is important to note that no muon identification requirements have been applied to the *Forward* tracks in the `Default` sequence. The most basic muon identification requirement applied at LHCb is `IsMuon`, which follows a similar procedure of `MuonMatchVeloUT` tracks but taking *Forward* tracks as an input and accounting for the possible multiple scattering in the detector material. Such requirement has an efficiency of 73% with respect to reconstructible long tracks in Run 2 conditions for muons from $K^0_S \to \mu^+\mu^-$ decays. The `IsMuon` requirement is usually the minimum muon identification requirement needed at LHCb, since more sophisticated algorithms make use of the muon hits selected by it in order to apply a more exhaustive selection. Taking this into account the best performance, achieved by running the `Default` reconstruction sequence with no p_T requirements and applying `IsMuon` on top, is expected to have an efficiency of 53%. The efficiency ratio between the two sequences for $K^0_S \to \mu^+\mu^-$, is then 83%. Taking Run 2 samples as a benchmark, and without considering muon identification requirements, if tracks are asked to satisfy $p_T > 400$ MeV/c, it translates into a loss in efficiency of

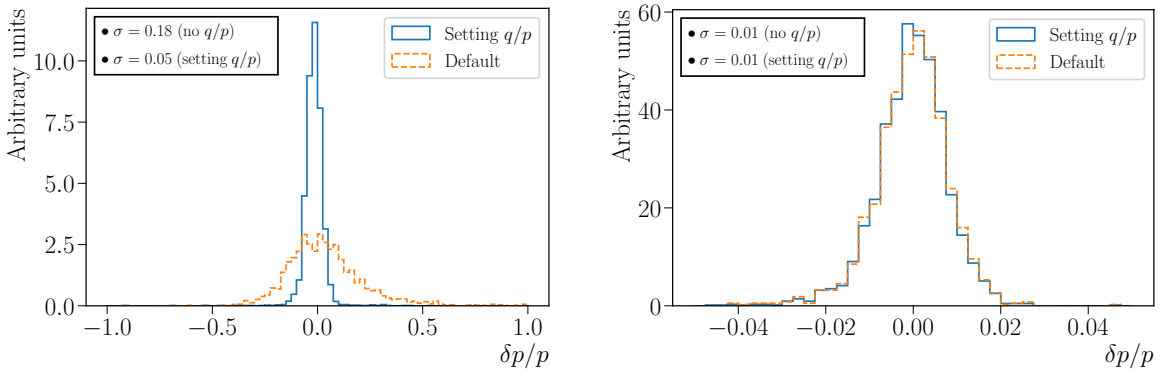

(a) (b)

Figure 4.7: Momentum resolution for tracks passing the `MuonMatchVeloUT` algorithm (left), together with those forwarded through the magnet (right) running in the default `MuonMatch` mode (dashed orange) and setting the value of q/p (solid blue). An improvement by a factor of four is observed, whilst the performance of the forward tracking remains almost unchanged.

around one order of magnitude, whilst if the threshold was relaxed to 250 MeV/c it would transform into a factor of 3. The current efficiency using the `MuonMatchVeloUT` algorithm is better to that of the `Default` reconstruction sequence with the standard p_T requirements of Run 2 and no muon identification requirements, defending its use in the upgrade.

Additional tests have been done in order to study the performance of the algorithm in the current framework for the upgraded HLT1. A selection has been developed emulating the requirements present in the Run 2 of the LHCb to study strange decays, called `Hlt1LowPtDiMuon`. In this trigger line, muons are required to satisfy the `MuonMatchVeloUT` algorithm, have a minimum value of the momentum and transverse momentum of 3 GeV/c and 80 GeV/c, respectively, a minimum value of the IP of 0.1 mm, and the track χ^2/dof being smaller than four. Muons are also required to satisfy the `IsMuon` requirement, which improves the quality of the muon identification using the fully extrapolated and fitted track. The combination must have a good vertex quality, with a χ^2/dof smaller than 25, separated by at least 0.5 mm perpendicular to the beam axis, with a ratio between the IP and the distance in the z-direction with respect to the best associated primary vertex smaller than 0.05, an invariant mass over the dimuon threshold, at 220 MeV/c^2, and the DOCA smaller than 0.3 mm. An additional line, `Hlt1LowPtMuon` has been designed in order to study semileptonic hyperon decays and Lepton Flavour Violation (LFV) modes, or any other signal decay with one soft muon in the final state. Similarly to the previous, muons must satisfy the `MuonMatchVeloUT` algorithm, with a transverse momentum greater than 80 MeV/c, a minimum momentum of 3 GeV/c, the IP must be greater than 0.4 mm, the χ^2_{IP} must be at least of 100, the track χ^2/dof must be smaller than four, and they must also satisfy the `IsMuon` requirement. Tracks also need to be separated at least by 10 mm with respect to the center of the beam pipe.

The retention is studied using different simulated samples in upgrade conditions. On

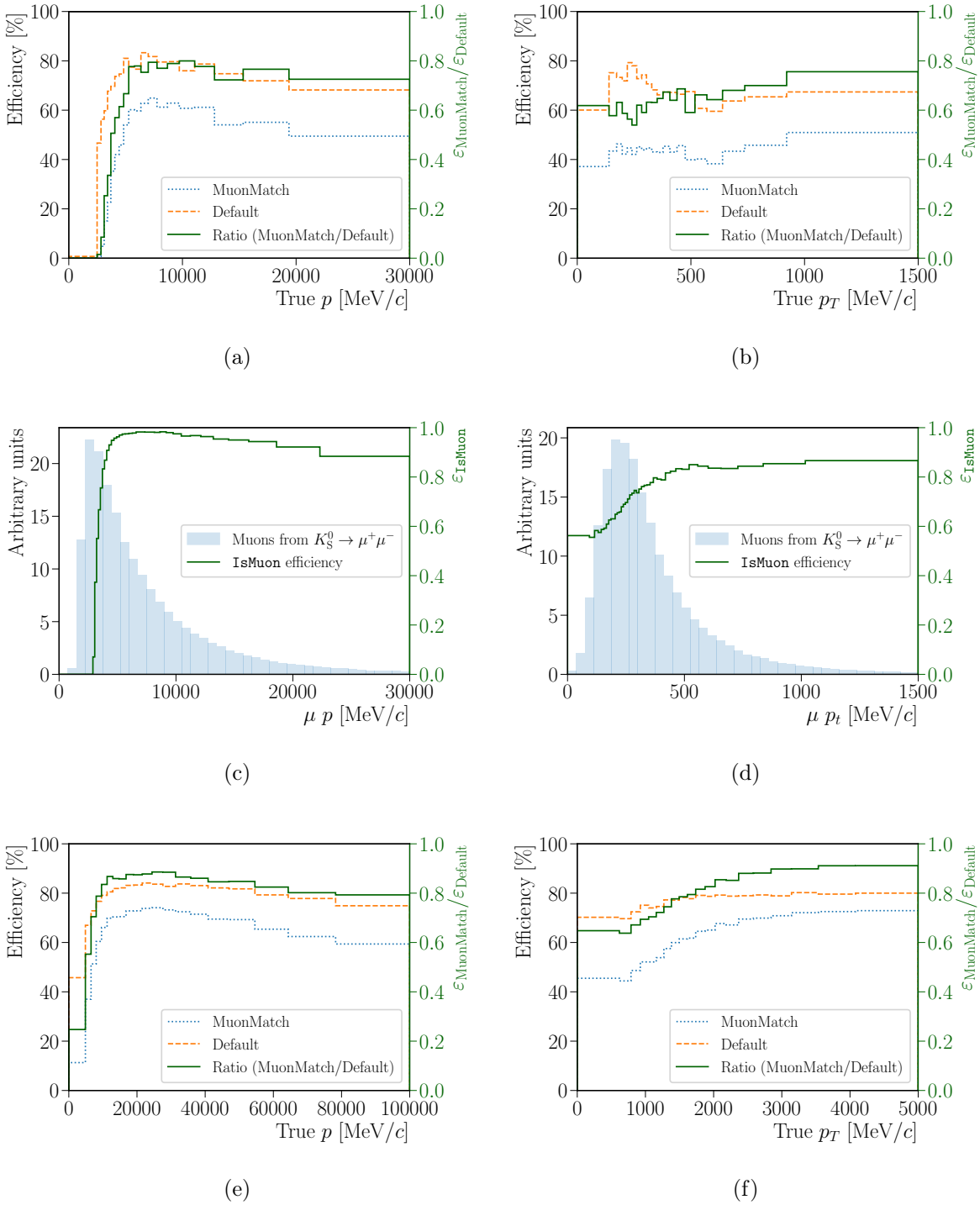

Figure 4.8: Top: Efficiencies of the *Forward* tracking in the `Default` (dashed orange) and `MuonMatch` (dotted blue) reconstruction sequences with respect to *Upstream* tracks, together with the efficiency ratio of the two (solid green), as a function of the true momentum (left) and transverse momentum (right) of muons from simulated $K^0_S \to \mu^+\mu^-$ candidates. Middle: Efficiencies of the `IsMuon` algorithm in Run 2 for muons from simulated $K^0_S \to \mu^+\mu^-$ candidates. Bottom: Similar plots to those displayed in the top of the figure but for simulated $J/\psi \to \mu^+\mu^-$ candidates, with different momenta ranges.

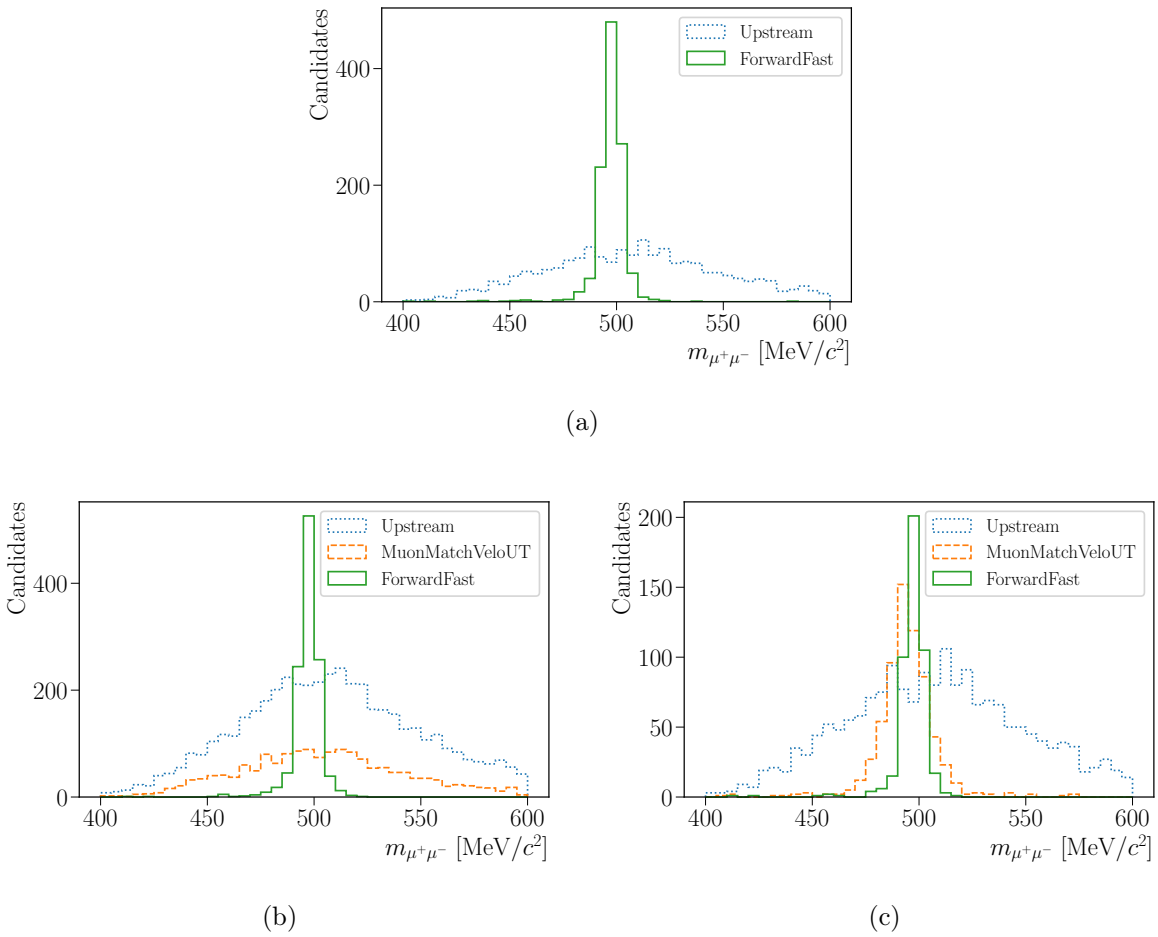

Figure 4.9: Dimuon invariant mass for different steps of the reconstruction chain and in three different reconstruction scenarios. Top: default reconstruction sequence. Bottom left: reconstruction chain including the `MuonMatchVeloUT` algorithm. Bottom right: reconstruction chain including the `MuonMatchVeloUT` algorithm, allowing it to improve the value of the momentum of the *Upstream* tracks.

Table 4.2: Rates in MB events and efficiencies for different simulated strange decays in upgrade conditions, expressed as a percentage, for the two HLT1 lines. The efficiencies are computed assuming that in events passing each trigger line, if the signal decay is present it satisfies the requirements. The numbers in parentheses denote the efficiencies if the head particles decay inside the VELO. In events with simulated $\Lambda \to p\mu\nu_\mu$ decays, the trigger lines have higher chances to be fired by particles from the underlying event since there is only one muon in the decay chain.

	`Hlt1LowPtDiMuon`	`Hlt1LowPtMuon`
Minimum Bias	28 kHz	12 kHz
$K^0_S \to \mu^+\mu^-$	0.11(0.43)	0.04(0.17)
$K^0_S \to \pi^0\mu^+\mu^-$	0.09(0.39)	0.03(0.13)
$\Sigma^+ \to p\mu^+\mu^-$	0.05(0.23)	0.02(0.09)
$\Lambda \to p\mu\nu_\mu$	0.01(0.14)	0.01(0.10)

one hand, $K^0_S \to \mu^+\mu^-$, $\Sigma^+ \to p\mu^+\mu^-$, $K^0_S \to \pi^0\mu^+\mu^-$ and $\Lambda \to p\mu\nu_\mu$ samples are used in order to estimate the efficiency of signal candidates. Due to the lack of an algorithm to calculate the number of TOS candidates at the moment, the signal efficiency is considered to be equal to the number of events passing the trigger selection evaluated on the signal samples. This approximation can be assumed at 1% level, since the purity of the offline selection for $K^0_S \to \mu^+\mu^-$ in Run 2 simulated events is greater than 99%[4]. On the other hand, the simulated sample of proton-proton collisions is used as MB proxy. The rate reserved for HLT1 lines in the upgrade is expected to be $\mathcal{O}(100$ kHz). With an input rate of 30 MHz, retentions must be $\sim$0.3% in order to be within an acceptable level. Results are shown in Table 4.2. Note that, for the two lines presented here, no requirements have been applied in variables like the ghost probability or additional muon identification requirements. These variables have shown to be very efficient in Run 2, but at the moment of writing this document no implementation of the corresponding algorithms has been done in the LHCb upgrade framework. Since in this analysis only the aforementioned trigger lines are present, no distinction is been done between *exclusive rate*, which is the contribution to the global rate that comes exclusively from each trigger line; and *inclusive rate*, which is the contribution to the global rate that is shared with other lines in the trigger system. In the scenario of having a big overlap between the retentions of `Hlt1LowPtDiMuon` and `Hlt1LowPtMuon` with the rest of the trigger lines the selections could be relaxed, leading to a high increase in efficiency. The imposition of additional requirements in the signal candidates at HLT2 and offline is expected to have an impact on the efficiency of 90%, as it happened between HLT1 and HLT2, and between HLT2 and the offline selection in Run 2. This means that efficiencies greater than 0.1% are possible for strange decays, giving a promising future for the Upgrade.

[4] This implies that on events with one $K^0_S \to \mu^+\mu^-$ candidate, less than 1% of the times the requirements will be satisfied by something that is not the $K^0_S \to \mu^+\mu^-$ candidate.

5

Conclusions

Strange decays still play a major role in the understanding of fundamental interactions. Experiments like NA62 or KOTO are about to measure the branching fractions of the $K \to \pi\nu\bar{\nu}$ decay modes. The possible anomaly in ε'/ε, together with recent searches for rare decays of strange hadrons, make this a very active field nowadays. The LHCb detector, initially developed to study b and c hadron decays, has showed to be able to adapt itself to cover also strange decays. With the study of $K^0_S \to \mu^+\mu^-$ and $\Sigma^+ \to p\mu^+\mu^-$, together with the preliminary studies of $K^0_S \to \pi^0\mu^+\mu^-$ and $K^0_S \to \ell^+\ell^-\ell^+\ell^-$ decays, the LHCb managed to obtain a hollow in this field.

In this thesis, a search for one of the most rare decays in nature studied at the LHC, $K^0_S \to \mu^+\mu^-$, has been presented. At LHCb, the excellent invariant mass resolution of $\mathcal{O}(4\ \text{MeV}/c^2)$ around the K^0_S meson nominal mass, together with efficient muon identification algorithms, allows to drastically reduce dangerous backgrounds, like $K^0_S \to \pi^+\pi^-$ or $K^0_S \to \pi\mu\nu$. A big contribution from inelastic material interactions is also observed, which is reduced thanks to the good knowledge of the geometry of the LHCb detector. The expected sensitivity suggested to start considering the $K^0_L \to \mu^+\mu^-$ contribution in the fits. Using data collected by the LHCb experiment in Run 2, the analysis concluded with a number of observed $K^0_S \to \mu^+\mu^-$ and $K^0_L \to \mu^+\mu^-$ decays compatible with zero. Using the likelihood profile of the $K^0_S \to \mu^+\mu^-$ branching fraction and combining it with the result obtained in Run 1 analysis, a new limit has been set to this decay, with a value of

$$\mathcal{B}(K^0_S \to \mu^+\mu^-) < 2.1(2.4) \times 10^{-10} \text{ at } 90(95)\% \text{ CL.} \tag{5.1}$$

The achieved result constitutes the most stringent limit up to date, and will help to discriminate among NP scenarios. In particular, this decay is helping to constraint different SUSY and leptoquark models, complementing the information from other studies, like $K \to \pi\nu\bar{\nu}$ or ε'/ε. The LHCb is expected to lower the limit on this branching fraction in the upgrade. The removal of the hardware trigger, currently the main bottleneck to study strange decays, gives a promising scenario, where sensitivities $\mathcal{O}(10^{-11})$ are possible.

To conclude, preliminary studies of low-p_T muon reconstruction techniques for the upgraded LHCb detector have been presented. These techniques might be the only option to maintain high efficiencies for strange decays involving muons. Current results show that the overall efficiency can be similar to that achieved in Run 2 with possible gains at the trigger level, providing a good perspective to study strange hadrons with the LHCb detector in the future.

Bibliography

[1] Particle Data Group, K. Nakamura *et al.*, *Review of particle physics*, J. Phys. G **G37** (2010) 075021.

[2] M. K. Gaillard, P. D. Grannis, and F. J. Sciulli, *The Standard Model of Particle Physics*, Rev. Mod. Phys. **71** (1999) S96, arXiv:hep-ph/9812285.

[3] Wikimedia Commons, *Standard Model*, File:Standard Model of Elementary Particles.svg, 2020.

[4] A. D. Sakharov, *Baryon asymmetry of the universe*, Soviet Physics Uspekhi **34** (1991) 417.

[5] E. Witten, *An SU(2) anomaly*, Physics Letters B **117** (1982) 324.

[6] LEP, ALEPH, DELPHI, L3, OPAL, LEP Electroweak Working Group, SLD Heavy Flavor Group, SLD Electroweak Group, *A Combination of Preliminary Electroweak Measurements and Constraints on the Standard Model*, arXiv:hep-ex/0103048.

[7] A. Djouadi and A. Lenz, *Sealing the fate of a fourth generation of fermions*, Phys. Lett. **B715** (2012) 310, arXiv:1204.1252.

[8] SNO Collaboration, Q. R. Ahmad *et al.*, *Direct Evidence for Neutrino Flavor Transformation from Neutral-Current Interactions in the Sudbury Neutrino Observatory*, Phys. Rev. Lett. **89** (2002) 011301.

[9] SNO Collaboration, Q. R. Ahmad *et al.*, *Measurement of the Rate of* $\nu_e + d \rightarrow p + p + e^-$ *Interactions Produced by* ^{8}B *Solar Neutrinos at the Sudbury Neutrino Observatory*, Phys. Rev. Lett. **87** (2001) 071301.

[10] M. H. Goroff and A. Sagnotti, *The Ultraviolet Behavior of Einstein Gravity*, Nucl. Phys. **B266** (1986) 709.

[11] G. 't Hooft and M. J. G. Veltman, *One loop divergencies in the theory of gravitation*, Ann. Inst. H. Poincare Phys. Theor. **A20** (1974) 69.

[12] C. A. Baker *et al.*, *An Improved experimental limit on the electric dipole moment of the neutron*, Phys. Rev. Lett. **97** (2006) 131801, arXiv:hep-ex/0602020.

[13] V. C. Rubin, *A Century of Galaxy Spectroscopy*, Astrophysical Journal **451** (1995) 419.

[14] S. P. Martin, *A Supersymmetry primer*, Adv. Ser. Direct. High Energy Phys. (2010), arXiv:hep-ph/9709356.

[15] S. Weinberg and E. Witten, *Limits on massless particles*, Physics Letters B **96** (1980) 59.

[16] M. Maniatis, *The next-to-minimal supersymmetric extension of the standard model reviewed*, Int. J. Mod. Phys. A **25** (2010) 3505, arXiv:0906.0777.

[17] N. Arkani-Hamed, S. Dimopoulos, and G. R. Dvali, *Phenomenology, astrophysics and cosmology of theories with submillimeter dimensions and tev scale quantum gravity*, Phys. Rev. D **59** (1999) 086004, arXiv:hep-ph/9807344.

[18] G. Jungman, M. Kamionkowski, and K. Griest, *Supersymmetric dark matter*, Phys. Rept. **267** (1996) 195, arXiv:hep-ph/9506380.

[19] A. Arbey, F. Mahmoudi, O. Stal, and T. Stefaniak, *Status of the Charged Higgs Boson in Two Higgs Doublet Models*, Eur. Phys. J. **C78** (2018) 182, arXiv:1706.07414.

[20] P. Langacker, *The Physics of Heavy Z' Gauge Bosons*, Rev. Mod. Phys. **81** (2009) 1199, arXiv:0801.1345.

[21] L. D. Duffy and K. van Bibber, *Axions as Dark Matter Particles*, New J. Phys. **11** (2009) 105008, arXiv:0904.3346.

[22] CAST, V. Anastassopoulos *et al.*, *New CAST Limit on the Axion-Photon Interaction*, Nature Phys. **13** (2017) 584, arXiv:1705.02290.

[23] ADMX, N. Du *et al.*, *A Search for Invisible Axion Dark Matter with the Axion Dark Matter Experiment*, Phys. Rev. Lett. **120** (2018) 151301, arXiv:1804.05750.

[24] J. A. Aguilar-Saavedra, R. Benbrik, S. Heinemeyer, and M. Pérez-Victoria, *Handbook of vectorlike quarks: Mixing and single production*, Phys. Rev. **D88** (2013) 094010, arXiv:1306.0572.

[25] M. Schmaltz and Y.-M. Zhong, *The leptoquark Hunter's guide: large coupling*, JHEP **01** (2019) 132, arXiv:1810.10017.

[26] B. Diaz, M. Schmaltz, and Y.-M. Zhong, *The leptoquark Hunter's guide: Pair production*, JHEP **10** (2017) 097, arXiv:1706.05033.

[27] Super-Kamiokande Collaboration, K. Abe *et al.*, *Search for proton decay via $p \to e^+\pi^0$ and $p \to \mu^+\pi^0$ in* 0.31 *megaton·years exposure of the Super-Kamiokande water Cherenkov detector*, Phys. Rev. D **95** (2017) 012004.

[28] LHCb, R. Aaij *et al.*, *Search for lepton-universality violation in $B^+ \to K^+\ell^+\ell^-$ decays*, Phys. Rev. Lett. **122** (2019) 191801, arXiv:1903.09252.

[29] LHCb collaboration, R. Aaij *et al.*, *Test of lepton flavor universality by the measurement of the $B^0 \to D^{*-}\tau^+\nu_\tau$ branching fraction using three-prong τ decays*, Phys. Rev. **D97** (2018) 072013, arXiv:1711.02505.

[30] S. L. Glashow, J. Iliopoulos, and L. Maiani, *Weak interactions with lepton-hadron symmetry*, Phys. Rev. D **2** (1970) 1285.

[31] J. H. Christenson, J. W. Cronin, V. L. Fitch, and R. Turlay, *Evidence for the 2π decay of the K_2^0 meson*, Phys. Rev. Lett. **13** (1964) 138.

[32] G. D'Ambrosio, G. F. Giudice, G. Isidori, and A. Strumia, *Minimal flavor violation: An effective field theory approach*, Nucl. Phys. B **645** (2002) 155, arXiv:hep-ph/0207036.

[33] M. Blanke, A. J. Buras, D. Guadagnoli, and C. Tarantino, *Minimal Flavour Violation Waiting for Precise Measurements of ΔM_s, $S_{\psi\phi}$, A_{SL}^s, $|V_{ub}|$, γ and $B_{s,d}^0 \to \mu^+\mu^-$*, JHEP **10** (2006) 003, arXiv:hep-ph/0604057.

[34] NA62, E. Cortina Gil *et al.*, *The Beam and detector of the NA62 experiment at CERN*, JINST **12** (2017) P05025, arXiv:1703.08501.

[35] T. Yamanaka and for the KOTO Collaboration, *The J-PARC KOTO experiment*, Progress of Theoretical and Experimental Physics **2012** (2012).

[36] KLEVER Project, F. Ambrosino *et al.*, *KLEVER: An experiment to measure $BR(K_L \to \pi^0\nu\bar{\nu})$ at the CERN SPS*, arXiv:1901.03099.

[37] V. Cirigliano *et al.*, *Kaon Decays in the Standard Model*, Rev. Mod. Phys. **84** (2012) 399, arXiv:1107.6001.

[38] LHCb Collaboration, R. Aaij *et al.*, *Evidence for the rare decay $\Sigma^+ \to p\mu^+\mu^-$*, Phys. Rev. Lett. **120** (2018) 221803.

[39] M. Bauer, S. Casagrande, U. Haisch, and M. Neubert, *Flavor Physics in the Randall-Sundrum Model: II. Tree-Level Weak-Interaction Processes*, JHEP **09** (2010) 017, arXiv:0912.1625.

[40] NA48/1, J. R. Batley *et al.*, *Observation of the rare decay $K_S^0 \to \pi^0\mu^+\mu^-$*, Phys. Lett. **B599** (2004) 197, arXiv:hep-ex/0409011.

[41] V. G. Chobanova *et al.*, *Sensitivity of LHCb and its upgrade in the measurement of $\mathcal{B}(K_S^0 \to \pi^0\mu^+\mu^-)$*, LHCb-PUB-2016-017.

[42] V. Chobanova *et al.*, *Probing susy effects in $K_S^0 \to \mu^+\mu^-$*, JHEP **2018** (2018) 24.

[43] G. Isidori and R. Unterdorfer, *On the short-distance constraints from $K_{L,S} \to \mu^+\mu^-$*, JHEP **2004** (2004) 009.

[44] G. Ecker and A. Pich, *The longitudinal muon polarization in $K_L \to \mu^+\mu^-$*, Nuclear Physics B **366** (1991) 189.

[45] C. Bobeth and A. J. Buras, *Leptoquarks meet ϵ'/ϵ and rare kaon processes*, JHEP **2018** (2018) 101.

[46] H.-M. Chang, M. González-Alonso, and J. Martin Camalich, *Nonstandard semileptonic hyperon decays*, Phys. Rev. Lett. **114** (2015) 161802.

[47] Particle Data Group, M. Tanabashi *et al.*, *Review of particle physics*, Phys. Rev. D **98** (2018) 030001.

[48] G. D'Ambrosio and T. Kitahara, *Direct CP Violation in $K \to \mu^+\mu^-$*, Phys. Rev. Lett. **119** (2017) 201802.

[49] G. D'Ambrosio, G. Ecker, G. Isidori, and H. Neufeld, *Radiative nonleptonic kaon decays*, in *2nd DAPHNE Physics Handbook*, pp. 265–313, 1994, arXiv:hep-ph/9411439.

[50] KTeV Collaboration, A. Alavi-Harati *et al.*, *Measurements of direct* CP *violation,* CPT *symmetry, and other parameters in the neutral kaon system*, Phys. Rev. D **67** (2003) 012005.

[51] J. R. Batley *et al.*, *A precision measurement of direct CP violation in the decay of neutral kaons into two pions*, Physics Letters B **544** (2002) 97.

[52] H. Burkhardt *et al.*, *First evidence for direct CP violation*, Physics Letters B **206** (1988) 169.

[53] L. K. Gibbons *et al.*, *Measurement of the CP-violation parameter Re(ε'/ε)*, Phys. Rev. Lett. **70** (1993) 1203.

[54] RBC, UKQCD, Z. Bai *et al.*, *Standard Model Prediction for Direct CP Violation in $K \to \pi\pi$ Decay*, Phys. Rev. Lett. **115** (2015) 212001, arXiv:1505.07863.

[55] H. Gisbert and A. Pich, *Direct CP violation in $K^0 \to \pi\pi$: Standard Model Status*, Rept. Prog. Phys. **81** (2018) 076201, arXiv:1712.06147.

[56] LHCb collaboration, R. Aaij *et al.*, *Improved limit on the branching fraction of the rare decay $K^0_S \to \mu^+\mu^-$*, Eur. Phys. J. **C77** (2017) 678, arXiv:1706.00758.

[57] J. Alitti *et al.*, *An improved determination of the ratio of W and Z masses at the CERN pp collider*, Physics Letters B **276** (1992) 354 .

[58] J. Ellis, M. K. Gaillard, and D. V. Nanopoulos, *A Historical Profile of the Higgs Boson*, arXiv:1201.6045.

[59] S. A. Bludman, *On the universal Fermi interaction*, Nuovo Cim. **9** (1958) 433.

[60] F. J. Hasert *et al.*, *Observation of neutrino-like interactions without muon or electron in the gargamelle neutrino experiment*, Physics Letters B **46** (1973) 138.

[61] G. Arnison *et al.*, *Experimental observation of lepton pairs of invariant mass around 95 GeV/c^2 at the CERN SPS collider*, Physics Letters B **126** (1983) 398.

[62] UA2, P. Bagnaia *et al.*, *Evidence for $Z^0 \to e^+e^-$ at the CERN $\bar{p}p$ collider*, Phys. Lett. **129B** (1983) 130.

[63] A. Abashian *et al.*, *The Belle Detector*, Nucl. Instrum. Meth. **A479** (2002) 117.

[64] BaBar, B. Aubert *et al.*, *The BaBar detector*, Nucl. Instrum. Meth. **A479** (2002) 1, arXiv:hep-ex/0105044.

[65] ATLAS, G. Aad *et al.*, *The ATLAS Experiment at the CERN Large Hadron Collider*, JINST **3** (2008) S08003.

[66] CMS, S. Chatrchyan *et al.*, *The CMS Experiment at the CERN LHC*, JINST **3** (2008) S08004.

[67] ALICE, K. Aamodt *et al.*, *The ALICE experiment at the CERN LHC*, JINST **3** (2008) S08002.

[68] LHCb collaboration, A. A. Alves Jr. *et al.*, *The LHCb detector at the LHC*, JINST **3** (2008) S08005.

[69] A. A. Alves Jr. *et al.*, *Performance of the LHCb muon system*, JINST **8** (2013) P02022, arXiv:1211.1346.

[70] LHCb collaboration, R. Aaij *et al.*, *LHCb detector performance*, Int. J. Mod. Phys. **A30** (2015) 1530022, arXiv:1412.6352.

[71] LHCb collaboration, *Framework TDR for the LHCb Upgrade: Technical Design Report*, CERN-LHCC-2012-007.

[72] LHCb Collaboration, *Letter of Intent for the LHCb Upgrade*, CERN-LHCC-2011-001.

[73] LHCb Collaboration, *Expression of Interest for an LHCb Upgrade*, CERN-LHCC-2008-007.

[74] LHCb collaboration, *LHCb reoptimized detector design and performance: Technical Design Report*, CERN-LHCC-2003-030.

[75] LHCb collaboration, R. Aaij *et al.*, *Measurement of* $Z \to \tau^+\tau^-$ *production in proton-proton collisions at* $\sqrt{s} = 8\,TeV$, JHEP **09** (2018) 159, arXiv:1806.05008.

[76] LHCb collaboration, R. Aaij *et al.*, *Search for a dimuon resonance in the* Υ *mass region*, JHEP **09** (2018) 147, arXiv:1805.09820.

[77] LHCb collaboration, R. Aaij *et al.*, *Measurement of the inelastic pp cross-section at a centre-of-mass energy of* $\sqrt{s} = 13$ *TeV*, JHEP **06** (2018) 100, arXiv:1803.10974.

[78] LHCb collaboration, R. Aaij *et al.*, *Study of* Υ *production in pPb collisions at* $\sqrt{s_{NN}} = 8.16$ *TeV*, JHEP **11** (2018) 194, arXiv:1810.07655.

[79] LHCb collaboration, R. Aaij *et al.*, *Prompt and nonprompt* J/ψ *production and nuclear modification in pPb collisions at* $\sqrt{s_{NN}} = 8.16$ *TeV*, Phys. Lett. **B774** (2017) 159, arXiv:1706.07122.

[80] LHCb collaboration, R. Aaij *et al.*, *Observation of* Z *production in proton-lead collisions at LHCb*, JHEP **09** (2014) 030, arXiv:1406.2885.

[81] LHCb, R. Aaij *et al.*, *LHCb Detector Performance*, Int. J. Mod. Phys. **A30** (2015) 1530022, arXiv:1412.6352.

[82] R. Aaij *et al.*, *Optimization of the muon reconstruction algorithms for LHCb Run 2*, LHCb-PUB-2017-007.

[83] LHCb, R. Aaij *et al.*, *Design and performance of the LHCb trigger and full real-time reconstruction in Run 2 of the LHC*, JINST **14** (2019) P04013, arXiv:1812.10790.

[84] R. Aaij, *Triggering on CP Violation Real-Time Selection and Reconstruction of $B_s^0 \to J/\psi\phi$ Decays*, PhD thesis, Jan, 2015, Presented 07 May 2015.

[85] V. Syropoulos, *Controlling Penguins : an estimate of penguin topologies contributing to the weak phase ϕ_s*, PhD thesis, 2017, Presented 03 Oct 2017.

[86] F. Dettori, D. Martinez Santos, and J. Prisciandaro, *Low-p_T dimuon triggers at LHCb in Run 2*, LHCb-PUB-2017-023.

[87] T. Sjostrand, S. Mrenna, and P. Z. Skands, *A Brief Introduction to PYTHIA 8.1*, Comput. Phys. Commun. **178** (2008) 852, arXiv:0710.3820.

[88] T. Sjostrand, S. Mrenna, and P. Z. Skands, *PYTHIA 6.4 Physics and Manual*, JHEP **05** (2006) 026, arXiv:hep-ph/0603175.

[89] I. Belyaev *et al.*, *Handling of the generation of primary events in Gauss, the LHCb simulation framework*, J. Phys. Conf. Ser. **331** (2011) 032047.

[90] D. J. Lange, *The EvtGen particle decay simulation package*, Nucl. Instrum. Meth. **A462** (2001) 152.

[91] P. Golonka and Z. Was, *PHOTOS Monte Carlo: A precision tool for QED corrections in Z and W decays*, Eur. Phys. J. **C45** (2006) 97, arXiv:hep-ph/0506026.

[92] Geant4 collaboration, J. Allison *et al.*, *Geant4 developments and applications*, IEEE Trans. Nucl. Sci. **53** (2006) 270.

[93] Geant4 collaboration, S. Agostinelli *et al.*, *Geant4: A simulation toolkit*, Nucl. Instrum. Meth. **A506** (2003) 250.

[94] M. Clemencic *et al.*, *The LHCb simulation application, Gauss: Design, evolution and experience*, J. Phys. Conf. Ser. **331** (2011) 032023.

[95] D. Müller, M. Clemencic, G. Corti, and M. Gersabeck, *ReDecay: A novel approach to speed up the simulation at LHCb*, Eur. Phys. J. **C78** (2018) 1009, arXiv:1810.10362.

[96] E871, D. Ambrose *et al.*, *Improved branching ratio measurement for the decay $K_{\rm L}^0 \to \mu^+\mu^-$*, Phys. Rev. Lett. **84** (2000) 1389.

[97] S. Gjesdal *et al.*, *Search for the decay $K_S \to 2\mu$*, Physics Letters B **44** (1973) 217.

[98] LHCb collaboration, R. Aaij *et al.*, *Search for the rare decay $K^0_S \to \mu^+\mu^-$*, JHEP **01** (2013) 090, arXiv:1209.4029.

[99] LHCb, R. Aaij *et al.*, *Strong constraints on the $K^0_S \to \mu^+\mu^-$ branching fraction*, arXiv:2001.10354.

[100] J. Podolanski and R. Armenteros, *III. Analysis of V-events*, The London, Edinburgh, and Dublin Philosophical Magazine and Journal of Science **45** (1954) 13.

[101] M. Alexander *et al.*, *Mapping the material in the LHCb vertex locator using secondary hadronic interactions*, JINST **13** (2018) P06008.

[102] F. Pedregosa *et al.*, *Scikit-learn: Machine learning in Python*, Journal of Machine Learning Research **12** (2011) 2825, see also http://scikit-learn.org.

[103] KLOE-2, D. Babusci *et al.*, *Measurement of the branching fraction for the decay $K_S \to \pi\mu\nu$ with the KLOE detector*, arXiv:1912.05990.

[104] T. Junk, *Confidence level computation for combining searches with small statistics*, Nucl. Instrum. Meth. **A434** (1999) 435, arXiv:hep-ex/9902006.

[105] A. A. Alves Junior *et al.*, *Prospects for measurements with strange hadrons at LHCb*, JHEP **2019** (2019) 48.

[106] KTeV Collaboration, A. Alavi-Harati *et al.*, *Measurement of the branching ratio and form factor of $K_L \to \mu^+\mu^-\gamma$*, Phys. Rev. Lett. **87** (2001) 071801.

[107] P. Laplace, *Théorie analytique des probabilités*, Courcier, Paris, 1812.

[108] C. J. Clopper and E. S. Pearson, *The use of confidence or fiducial limits illustrated in the case of the binomial*, Biometrika **26** (1934) 404.

[109] E. B. Wilson, *Probable inference, the law of succession, and statistical inference*, Journal of the American Statistical Association **22** (1927) 209.

[110] T. Skwarnicki, *A study of the radiative CASCADE transitions between the Upsilon-Prime and Upsilon resonances*, PhD thesis, Cracow, INP, 1986.

[111] M. Oreglia, *A Study of the Reactions $\psi' \to \gamma\gamma\psi$*, PhD thesis, SLAC, 1980.

[112] D. Martínez Santos and F. Dupertuis, *Mass distributions marginalized over per-event errors*, Nucl. Instrum. Meth. **A764** (2014) 150, arXiv:1312.5000.

[113] F. James and M. Roos, *Minuit: A System for Function Minimization and Analysis of the Parameter Errors and Correlations*, Comput. Phys. Commun. **10** (1975) 343.

[114] F. Feroz, M. P. Hobson, and M. Bridges, *MultiNest: an efficient and robust Bayesian inference tool for cosmology and particle physics*, Monthly Notices of the Royal Astronomical Society **398** (2009) 1601.

[115] LHCb collaboration, *Physics case for an LHCb Upgrade II — Opportunities in flavour physics, and beyond, in the HL-LHC era*, arXiv:1808.08865.

[116] LHCb collaboration, *Computing Model of the Upgrade LHCb experiment*, CERN-LHCC-2018-014.

[117] LHCb collaboration, *LHCb Tracker Upgrade Technical Design Report*, CERN-LHCC-2014-001.

[118] LHCb collaboration, *LHCb VELO Upgrade Technical Design Report*, CERN-LHCC-2013-021.

[119] R. Aaij *et al.*, *Tesla: an application for real-time data analysis in High Energy Physics*, Comput. Phys. Commun. **208** (2016) 35, arXiv:1604.05596.

[120] E. Bowen and B. Storaci, *VeloUT tracking for the LHCb Upgrade*, LHCb-PUB-2013-023.

[121] Y. Amhis, O. Callot, M. De Cian, and T. Nikodem, *Description and performance studies of the Forward Tracking for a scintilating fibre detector at LHCb*, LHCb-PUB-2014-001.

[122] Y. Amhis *et al.*, *The Seeding tracking algorithm for a scintillating detector at LHCb*, LHCb-PUB-2014-002.

A Multivariate analysis

Additional information about the performance of the ABDT algorithms of Sect. 3.4.2 is shown in this appendix. Checks have been done to evaluate the importance of the features used to train the classifiers, as well as their correlation, and can be seen in Fig. A.1 and Fig. A.2. In Fig. A.3, the distribution of the signal probability for different invariant mass ranges is shown, serving as an additional check for the absence of correlation between the output of the ABDT classifiers and the dimuon invariant mass. The distributions in Fig. A.4 reveal that in the left sideband of the dimuon invariant mass, dominated by doubly misidentified $K^0_S \to \pi^+\pi^-$ decays, for regions close to the VELO material the most dangerous background turns to come from inelastic interactions with the material of the detector.

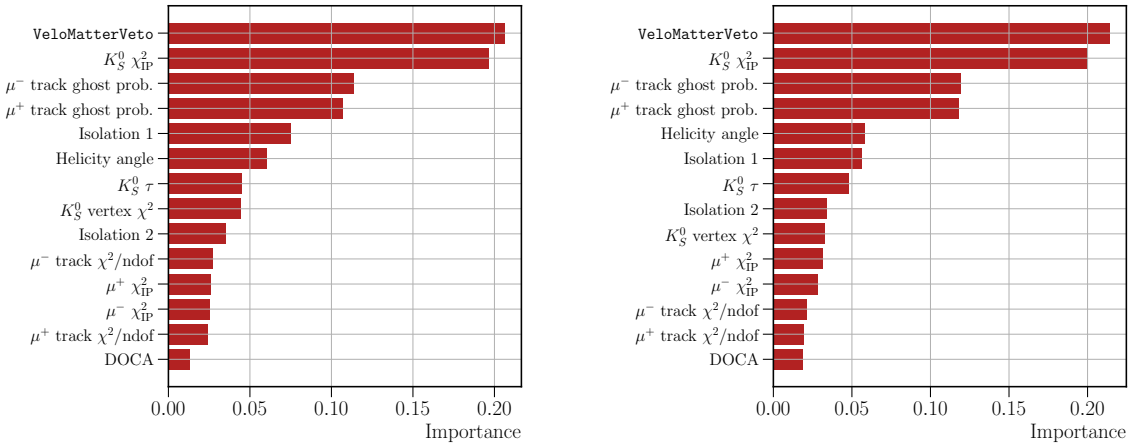

(a) (b)

Figure A.1: Importance of the variables used in the training of the TIS (left) and xTOS (right) ABDT classifiers, determined from the number of times each variable is used to split data across all the trees. The `VeloMatterVeto` variable leads the performance, followed by the χ^2_{IP} of the K^0_S and the ghost probabilities of the muons.

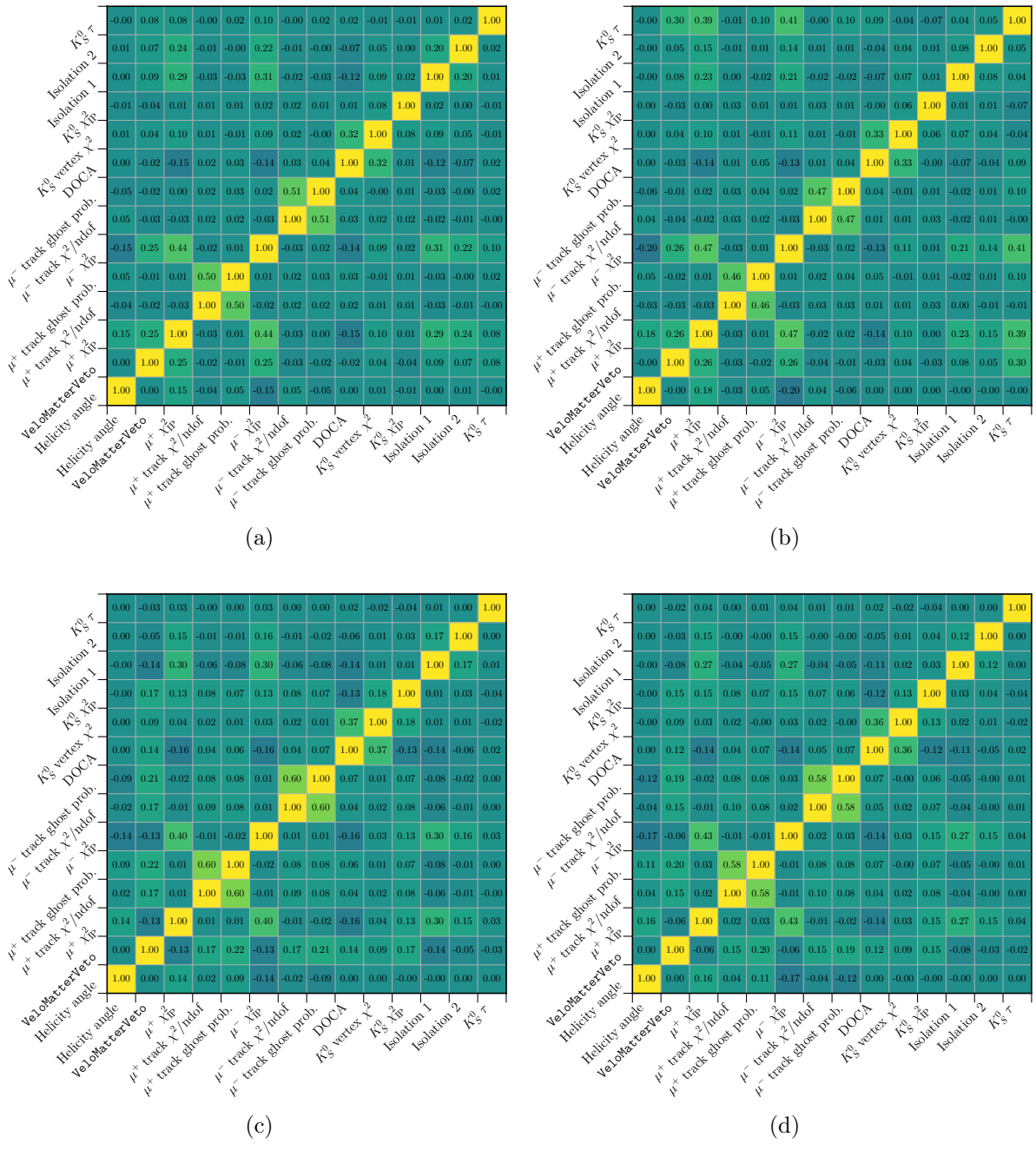

Figure A.2: Correlation matrices for the variables used in the training of the TIS (left) and xTOS (right) ABDT classifiers in the signal (top) and background (bottom) samples.

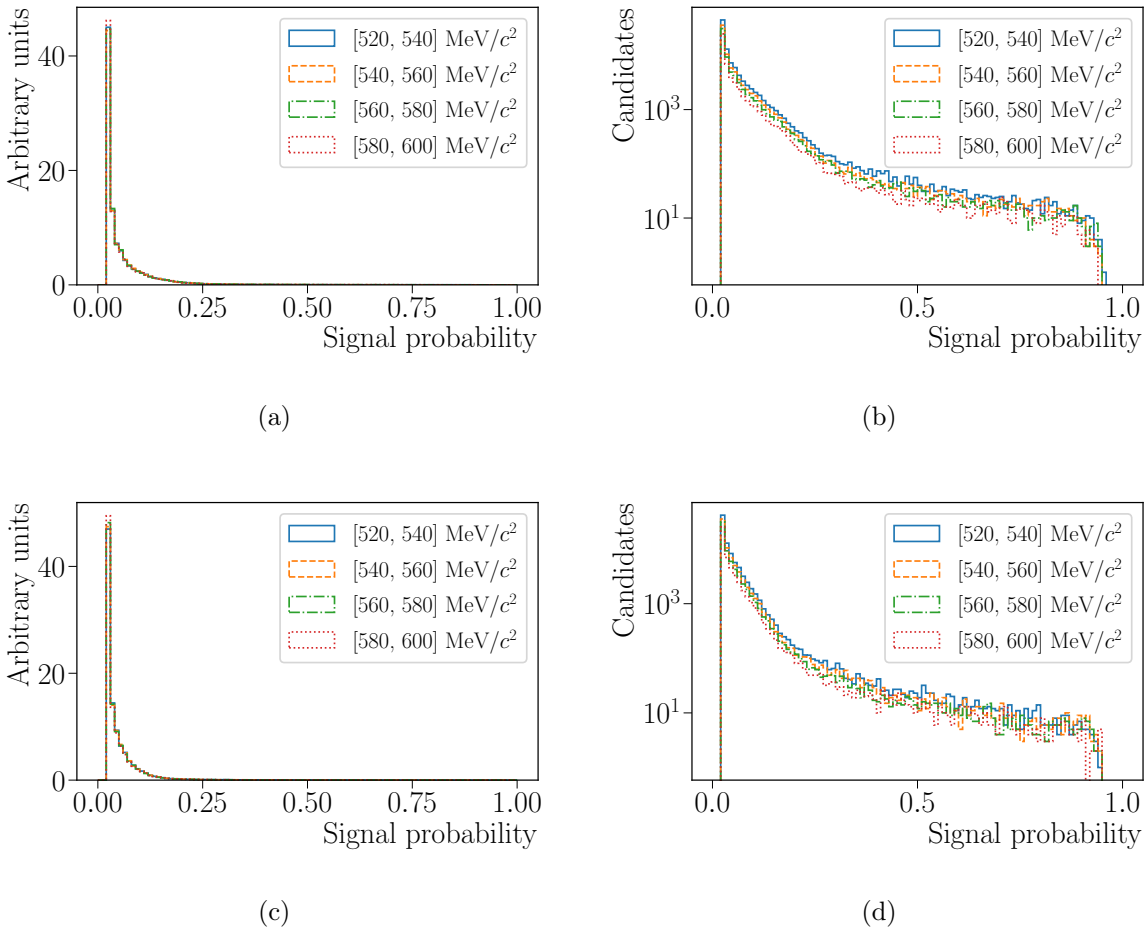

Figure A.3: Distribution of the signal probability of background candidates from the right sideband of the dimuon invariant mass for different ranges. Top and bottom plots correspond to the TIS and xTOS trigger categories, respectively. Histograms on the right are versions in logarithmic scale of the plots on the left.

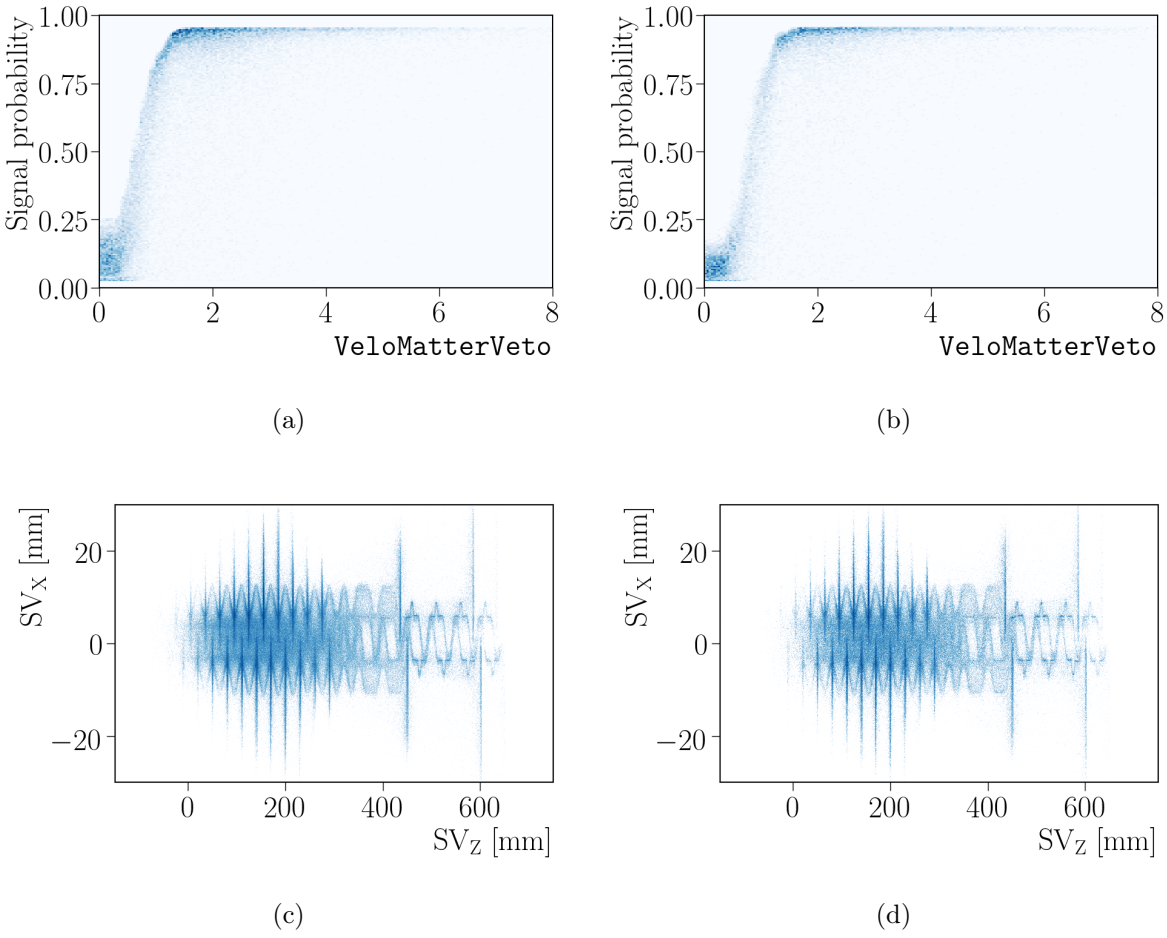

Figure A.4: Signal probability of the ABDT classifiers for the TIS (top left) and xTOS (top right) trigger categories as a function of the `VeloMatterVeto` tool defined in Sect. 3.4.2 for simulated $K^0_S \to \mu^+\mu^-$ candidates. The bottom plots show the SV position for $K^0_S \to \mu^+\mu^-$ candidates on the left sideband $m_{\mu^+\mu^-} < 490$ MeV/c^2 after requiring the signal probability to be smaller than 25%, where the pattern of the VELO can be clearly seen.

B Muon identification

In Fig. B.1 and Fig. B.2, the evolution of the expected CLs as a function of the requirement in the `muonIDPlusBDT` variable is shown for different ABDT bins and trigger categories. The requirement on the `muonIDPlusBDT` variable is determined using the minimum of the expected CLs as a figure of merit. A wide range of values for the requirement with close values for the expected CLs is found, being very similar for the two trigger categories. To simplify the selection, the same requirements are applied to each trigger category, also common for some groups of ABDT bins.

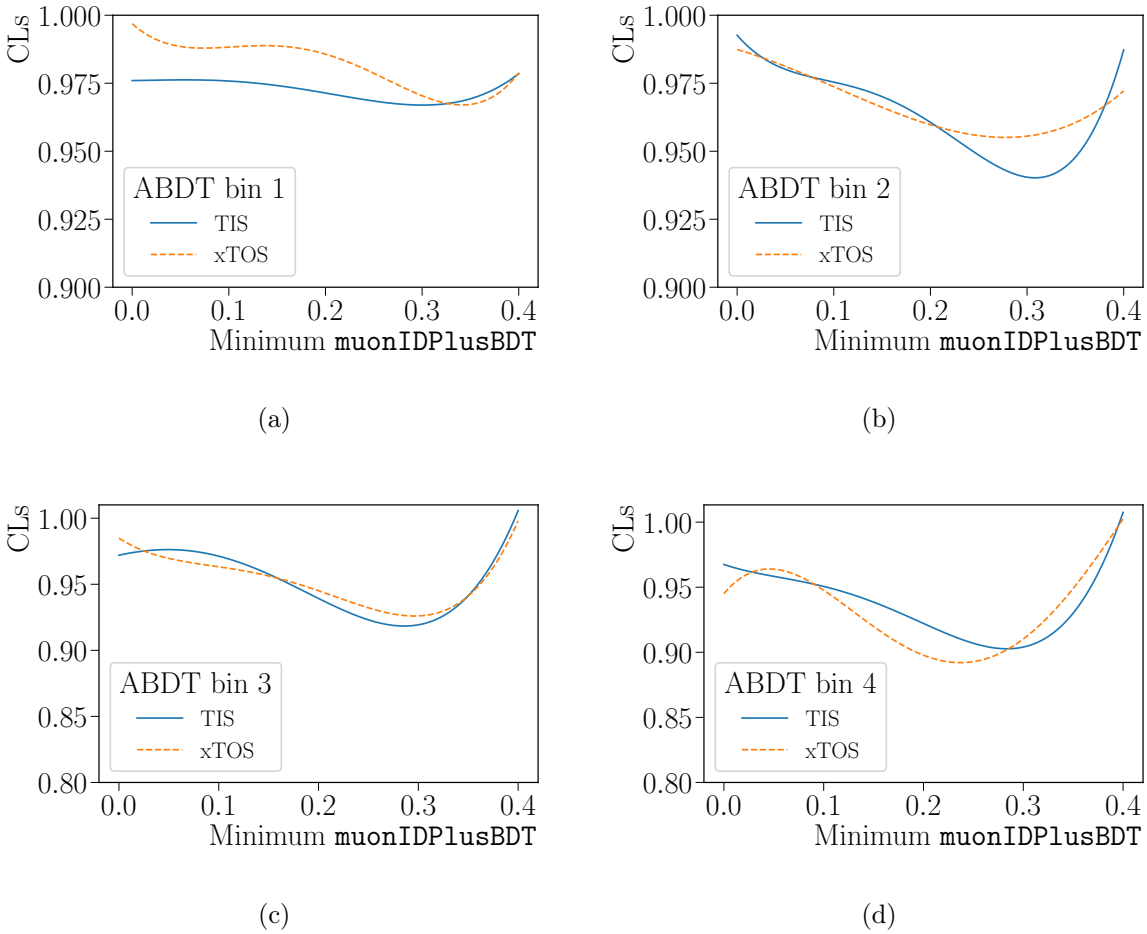

Figure B.1: Distribution of the expected CLs as a function of the requirement on the `muonIDPlusBDT` variable in the first four ABDT bins of each trigger category. Fluctuations are due to a small number of pseudo-experiments. Similar optimal values are found for the two trigger categories.

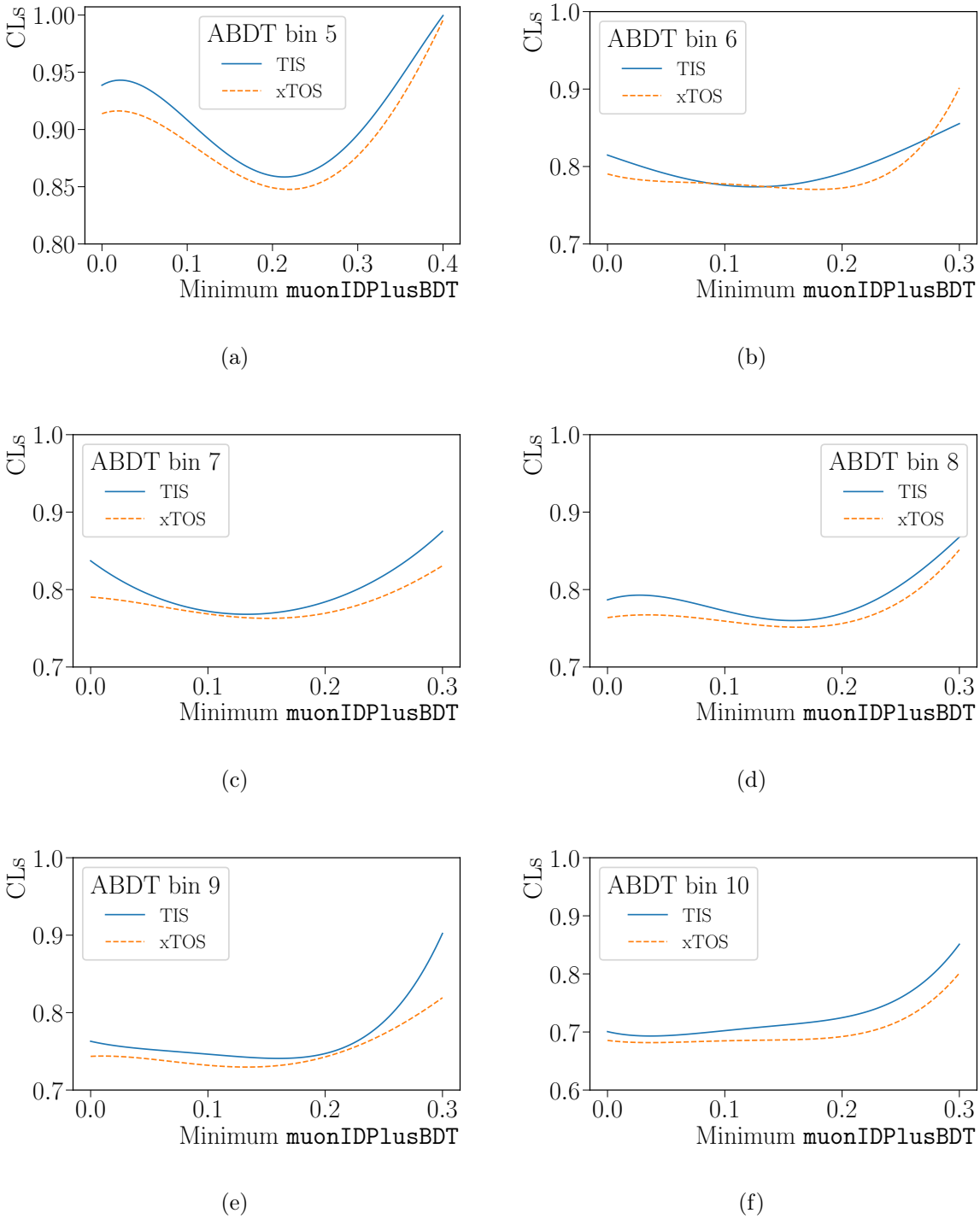

Figure B.2: Distribution of the expected CLs as a function of the requirement on the `muonIDPlusBDT` variable in the last six ABDT bins of each trigger category. Fluctuations are due to a small number of pseudo-experiments. Similar optimal values are found for the two trigger categories.

C Normalization

This appendix contains the values of the efficiencies for $K^0_S \to \mu^+\mu^-$ and $K^0_S \to \pi^+\pi^-$ where counting is done on a different way with respect to the method discussed in Sect. 3.7. In Table C.1, Table C.3 and Table C.5, efficiencies calculated using the number of entries in the MC samples are shown. In Table C.2, Table C.4 and Table C.6, efficiencies calculated using the sum of GBDT-based weights (discussed in Sect. 3.2) are shown. Central values are consistent with those obtained after the weighting procedure, in Tables 3.3–3.5.

Table C.1: Efficiencies for $K^0_S \to \pi^+\pi^-$ and $K^0_S \to \mu^+\mu^-$ candidates for the requirements applied before the division in bins of the BDT. The efficiencies are calculated from the number of candidates surviving each selection step. The results with p_T-based weights, used in the normalization, are shown in Table 3.3.

	$\boldsymbol{K^0_S \to \mu^+\mu^-}$	$\boldsymbol{K^0_S \to \pi^+\pi^-}$
Reconstruction + selection	$(7.105 \pm 0.009) \times 10^{-3}$	$(4.749 \pm 0.016) \times 10^{-3}$
TIS	$(6.323 \pm 0.033) \times 10^{-2}$	
xTOS	$(3.807 \pm 0.026) \times 10^{-2}$	

Table C.2: Efficiencies for $K^0_S \to \pi^+\pi^-$ and $K^0_S \to \mu^+\mu^-$ candidates for the requirements applied before the division in bins of the BDT. The efficiencies are calculated by summing the GBDT-based weights in the different MC samples after each selection step. Since such weights can not be calculated for the samples at generator level, the efficiency including generation, reconstruction and selection is calculated using p_T-based weights instead. The results with p_T-based weights, used in the normalization, are shown in Table 3.3.

	$\boldsymbol{K^0_S \to \mu^+\mu^-}$	$\boldsymbol{K^0_S \to \pi^+\pi^-}$
Reconstruction + selection	$(7.639 \pm 0.011) \times 10^{-3}$	$(5.223 \pm 0.017) \times 10^{-3}$
TIS	$(6.739 \pm 0.036) \times 10^{-2}$	
xTOS	$(4.154 \pm 0.029) \times 10^{-2}$	

Table C.3: ABDT, muon identification and total efficiencies for $K^0_S \to \mu^+\mu^-$ candidates in each trigger category. The efficiencies are calculated from the number of candidates surviving each selection step. The results with p_T-based weights, used in the normalization, are shown in Table 3.4.

	TIS			**TOS**		
ABDT bin	**ABDT**	**muon-ID**	**Total**	**ABDT**	**muon-ID**	**Total**
1	$(6.27 \pm 0.13) \times 10^{-2}$	0.252 ± 0.009	$(7.08 \pm 0.31) \times 10^{-6}$	$(6.45 \pm 0.17) \times 10^{-2}$	0.294 ± 0.013	$(5.13 \pm 0.26) \times 10^{-6}$
2	$(6.29 \pm 0.13) \times 10^{-2}$	0.242 ± 0.009	$(6.83 \pm 0.30) \times 10^{-6}$	$(6.47 \pm 0.17) \times 10^{-2}$	0.268 ± 0.012	$(4.70 \pm 0.25) \times 10^{-6}$
3	$(6.30 \pm 0.13) \times 10^{-2}$	0.263 ± 0.010	$(7.44 \pm 0.31) \times 10^{-6}$	$(6.47 \pm 0.17) \times 10^{-2}$	0.307 ± 0.013	$(5.37 \pm 0.27) \times 10^{-6}$
4	$(6.33 \pm 0.13) \times 10^{-2}$	0.479 ± 0.011	$(1.36 \pm 0.04) \times 10^{-5}$	$(6.54 \pm 0.17) \times 10^{-2}$	0.514 ± 0.014	$(9.10 \pm 0.35) \times 10^{-6}$
5	$(6.33 \pm 0.13) \times 10^{-2}$	0.507 ± 0.011	$(1.44 \pm 0.04) \times 10^{-5}$	$(6.48 \pm 0.17) \times 10^{-2}$	0.563 ± 0.014	$(9.87 \pm 0.36) \times 10^{-6}$
6	$(6.30 \pm 0.13) \times 10^{-2}$	0.814 ± 0.008	$(2.30 \pm 0.06) \times 10^{-5}$	$(6.45 \pm 0.17) \times 10^{-2}$	0.856 ± 0.010	$(1.49 \pm 0.04) \times 10^{-5}$
7	$(6.22 \pm 0.13) \times 10^{-2}$	0.817 ± 0.008	$(2.29 \pm 0.06) \times 10^{-5}$	$(6.41 \pm 0.17) \times 10^{-2}$	0.875 ± 0.009	$(1.52 \pm 0.04) \times 10^{-5}$
8	$(6.22 \pm 0.13) \times 10^{-2}$	0.825 ± 0.008	$(2.31 \pm 0.06) \times 10^{-5}$	$(6.37 \pm 0.17) \times 10^{-2}$	0.870 ± 0.009	$(1.50 \pm 0.04) \times 10^{-5}$
9	$(6.17 \pm 0.13) \times 10^{-2}$	0.906 ± 0.006	$(2.51 \pm 0.06) \times 10^{-5}$	$(6.36 \pm 0.17) \times 10^{-2}$	0.919 ± 0.008	$(1.58 \pm 0.05) \times 10^{-5}$
10	$(6.13 \pm 0.13) \times 10^{-2}$	0.925 ± 0.006	$(2.55 \pm 0.06) \times 10^{-5}$	$(6.29 \pm 0.17) \times 10^{-2}$	0.942 ± 0.007	$(1.60 \pm 0.05) \times 10^{-5}$

Table C.4: ABDT, muon identification and total efficiencies for $K^0_S \to \mu^+\mu^-$ candidates in each trigger category. The efficiencies are calculated by summing the GBDT-based weights in the different MC samples after each selection step. Since such weights can not be calculated for the samples at generator level, the efficiency including generation, reconstruction and selection is calculated using p_T-based weights instead. The total efficiency is then computed multiplying this efficiency by the efficiency on top of it. The results with p_T-based weights, used in the normalization, are shown in Table 3.4.

	TIS			**TOS**		
ABDT bin	**ABDT**	**muon-ID**	**Total**	**ABDT**	**muon-ID**	**Total**
1	$(6.19 \pm 0.13) \times 10^{-2}$	0.262 ± 0.010	$(8.36 \pm 0.37) \times 10^{-6}$	$(6.36 \pm 0.17) \times 10^{-2}$	0.298 ± 0.013	$(6.01 \pm 0.31) \times 10^{-6}$
2	$(6.20 \pm 0.13) \times 10^{-2}$	0.246 ± 0.009	$(7.85 \pm 0.35) \times 10^{-6}$	$(6.37 \pm 0.17) \times 10^{-2}$	0.278 ± 0.013	$(5.62 \pm 0.30) \times 10^{-6}$
3	$(6.22 \pm 0.13) \times 10^{-2}$	0.270 ± 0.010	$(8.65 \pm 0.37) \times 10^{-6}$	$(6.36 \pm 0.17) \times 10^{-2}$	0.313 ± 0.013	$(6.32 \pm 0.32) \times 10^{-6}$
4	$(6.23 \pm 0.13) \times 10^{-2}$	0.490 ± 0.011	$(1.57 \pm 0.05) \times 10^{-5}$	$(6.40 \pm 0.17) \times 10^{-2}$	0.530 ± 0.014	$(1.08 \pm 0.04) \times 10^{-5}$
5	$(6.23 \pm 0.13) \times 10^{-2}$	0.515 ± 0.011	$(1.65 \pm 0.05) \times 10^{-5}$	$(6.39 \pm 0.17) \times 10^{-2}$	0.576 ± 0.014	$(1.17 \pm 0.04) \times 10^{-5}$
6	$(6.24 \pm 0.13) \times 10^{-2}$	0.826 ± 0.008	$(2.65 \pm 0.06) \times 10^{-5}$	$(6.41 \pm 0.17) \times 10^{-2}$	0.865 ± 0.009	$(1.76 \pm 0.05) \times 10^{-5}$
7	$(6.20 \pm 0.13) \times 10^{-2}$	0.828 ± 0.008	$(2.64 \pm 0.06) \times 10^{-5}$	$(6.38 \pm 0.17) \times 10^{-2}$	0.887 ± 0.009	$(1.79 \pm 0.05) \times 10^{-5}$
8	$(6.19 \pm 0.13) \times 10^{-2}$	0.835 ± 0.008	$(2.66 \pm 0.06) \times 10^{-5}$	$(6.33 \pm 0.17) \times 10^{-2}$	0.881 ± 0.009	$(1.77 \pm 0.05) \times 10^{-5}$
9	$(6.18 \pm 0.13) \times 10^{-2}$	0.914 ± 0.006	$(2.91 \pm 0.07) \times 10^{-5}$	$(6.31 \pm 0.17) \times 10^{-2}$	0.928 ± 0.007	$(1.86 \pm 0.05) \times 10^{-5}$
10	$(6.23 \pm 0.13) \times 10^{-2}$	0.931 ± 0.005	$(2.99 \pm 0.07) \times 10^{-5}$	$(6.45 \pm 0.18) \times 10^{-2}$	0.950 ± 0.006	$(1.95 \pm 0.06) \times 10^{-5}$

Table C.5: ABDT and total efficiencies for $K^0_S \to \pi^+\pi^-$ candidates in each trigger category. The total efficiencies do not include the average downscale factor of the minimum bias stream. The efficiencies are calculated from the number of candidates surviving each selection step. The results with p_T-based weights, used in the normalization, are shown in Table 3.5.

	TIS		**xTOS**	
ABDT bin	**ABDT**	**Total**	**ABDT**	**Total**
1	$(7.12 \pm 0.08) \times 10^{-2}$	$(3.38 \pm 0.04) \times 10^{-4}$	$(7.82 \pm 0.09) \times 10^{-2}$	$(3.71 \pm 0.04) \times 10^{-4}$
2	$(7.33 \pm 0.09) \times 10^{-2}$	$(3.48 \pm 0.04) \times 10^{-4}$	$(7.70 \pm 0.09) \times 10^{-2}$	$(3.66 \pm 0.04) \times 10^{-4}$
3	$(7.28 \pm 0.08) \times 10^{-2}$	$(3.46 \pm 0.04) \times 10^{-4}$	$(7.81 \pm 0.09) \times 10^{-2}$	$(3.71 \pm 0.04) \times 10^{-4}$
4	$(7.02 \pm 0.08) \times 10^{-2}$	$(3.33 \pm 0.04) \times 10^{-4}$	$(8.37 \pm 0.09) \times 10^{-2}$	$(3.98 \pm 0.04) \times 10^{-4}$
5	$(7.37 \pm 0.09) \times 10^{-2}$	$(3.50 \pm 0.04) \times 10^{-4}$	$(7.27 \pm 0.08) \times 10^{-2}$	$(3.45 \pm 0.04) \times 10^{-4}$
6	$(6.43 \pm 0.08) \times 10^{-2}$	$(3.06 \pm 0.04) \times 10^{-4}$	$(5.97 \pm 0.08) \times 10^{-2}$	$(2.84 \pm 0.04) \times 10^{-4}$
7	$(6.13 \pm 0.08) \times 10^{-2}$	$(2.91 \pm 0.04) \times 10^{-4}$	$(5.63 \pm 0.08) \times 10^{-2}$	$(2.67 \pm 0.04) \times 10^{-4}$
8	$(5.75 \pm 0.08) \times 10^{-2}$	$(2.73 \pm 0.04) \times 10^{-4}$	$(5.14 \pm 0.07) \times 10^{-2}$	$(2.44 \pm 0.04) \times 10^{-4}$
9	$(4.88 \pm 0.07) \times 10^{-2}$	$(2.32 \pm 0.03) \times 10^{-4}$	$(5.39 \pm 0.07) \times 10^{-2}$	$(2.56 \pm 0.04) \times 10^{-4}$
10	$(4.45 \pm 0.07) \times 10^{-2}$	$(2.11 \pm 0.03) \times 10^{-4}$	$(4.62 \pm 0.07) \times 10^{-2}$	$(2.19 \pm 0.03) \times 10^{-4}$

Table C.6: ABDT and total efficiencies for $K^0_S \to \pi^+\pi^-$ candidates in each trigger category. The total efficiencies do not include the average downscale factor of the minimum bias stream. The efficiencies are calculated by summing the GBDT-based weights in the different MC samples after each selection step. Since such weights can not be calculated for the samples at generator level, the efficiency including generation, reconstruction and selection is calculated using p_T-based weights instead. The total efficiency is then computed multiplying this efficiency by the efficiency on top of it. The results with p_T-based weights, used in the normalization, are shown in Table 3.5.

	TIS		**xTOS**	
ABDT bin	**ABDT**	**Total**	**ABDT**	**Total**
1	$(7.08 \pm 0.08) \times 10^{-2}$	$(3.70 \pm 0.05) \times 10^{-4}$	$(7.76 \pm 0.09) \times 10^{-2}$	$(4.05 \pm 0.05) \times 10^{-4}$
2	$(7.26 \pm 0.09) \times 10^{-2}$	$(3.79 \pm 0.05) \times 10^{-4}$	$(7.62 \pm 0.09) \times 10^{-2}$	$(3.98 \pm 0.05) \times 10^{-4}$
3	$(7.16 \pm 0.08) \times 10^{-2}$	$(3.74 \pm 0.05) \times 10^{-4}$	$(7.70 \pm 0.09) \times 10^{-2}$	$(4.02 \pm 0.05) \times 10^{-4}$
4	$(6.89 \pm 0.08) \times 10^{-2}$	$(3.60 \pm 0.05) \times 10^{-4}$	$(8.19 \pm 0.09) \times 10^{-2}$	$(4.28 \pm 0.05) \times 10^{-4}$
5	$(7.22 \pm 0.09) \times 10^{-2}$	$(3.77 \pm 0.05) \times 10^{-4}$	$(7.11 \pm 0.08) \times 10^{-2}$	$(3.71 \pm 0.05) \times 10^{-4}$
6	$(6.35 \pm 0.08) \times 10^{-2}$	$(3.32 \pm 0.04) \times 10^{-4}$	$(5.88 \pm 0.08) \times 10^{-2}$	$(3.07 \pm 0.04) \times 10^{-4}$
7	$(6.10 \pm 0.08) \times 10^{-2}$	$(3.19 \pm 0.04) \times 10^{-4}$	$(5.58 \pm 0.08) \times 10^{-2}$	$(2.92 \pm 0.04) \times 10^{-4}$
8	$(5.76 \pm 0.08) \times 10^{-2}$	$(3.01 \pm 0.04) \times 10^{-4}$	$(5.11 \pm 0.07) \times 10^{-2}$	$(2.67 \pm 0.04) \times 10^{-4}$
9	$(4.88 \pm 0.07) \times 10^{-2}$	$(2.55 \pm 0.04) \times 10^{-4}$	$(5.37 \pm 0.07) \times 10^{-2}$	$(2.80 \pm 0.04) \times 10^{-4}$
10	$(4.52 \pm 0.07) \times 10^{-2}$	$(2.36 \pm 0.04) \times 10^{-4}$	$(4.73 \pm 0.07) \times 10^{-2}$	$(2.47 \pm 0.04) \times 10^{-4}$

D Signal mass calibration

In this appendix, the results for the fits to the dimuon invariant mass of simulated $K^0_S \to \mu^+\mu^-$ candidates used to calibrate the signal mass shape, are shown. The momentum of the muons has been downscaled in order to improve the data/MC agreement. The downscale factor has been obtained from simulated and data $K^0_S \to \pi^+\pi^-$ candidates.

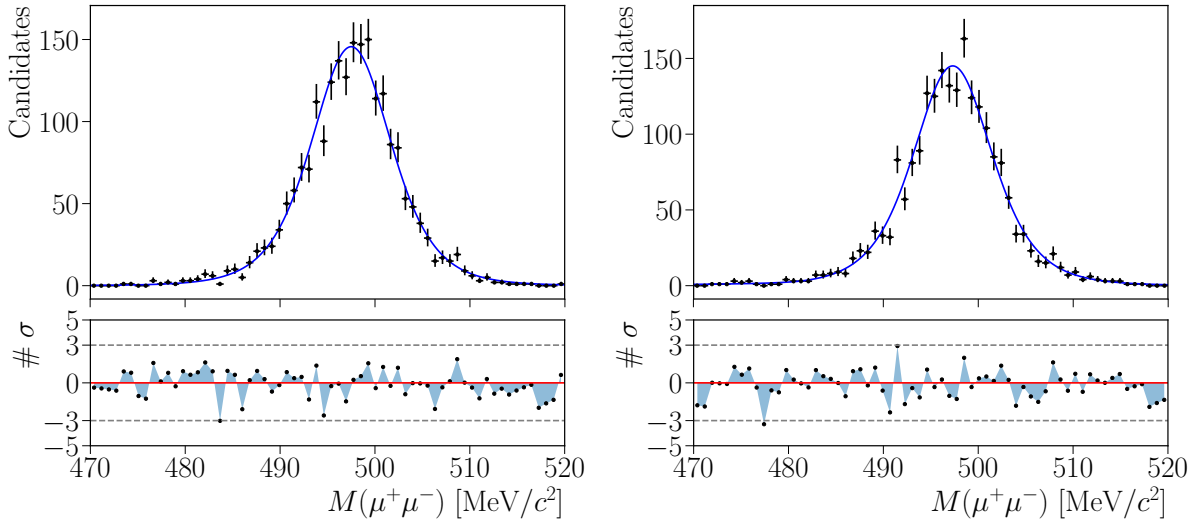

Figure D.1: Result of the fits to the dimuon invariant mass for simulated $K^0_S \to \mu^+\mu^-$ candidates with the muon momentum downscaled by 0.99939 for the first two bins (1–2) of the TIS trigger category. The residual plots, showing the deviation of the fit curve to the data points, as a number of standard deviations, are displayed under their corresponding invariant mass plots. Parameters extracted in these fits, associated to the signal PDF, are fixed in the final fit to data.

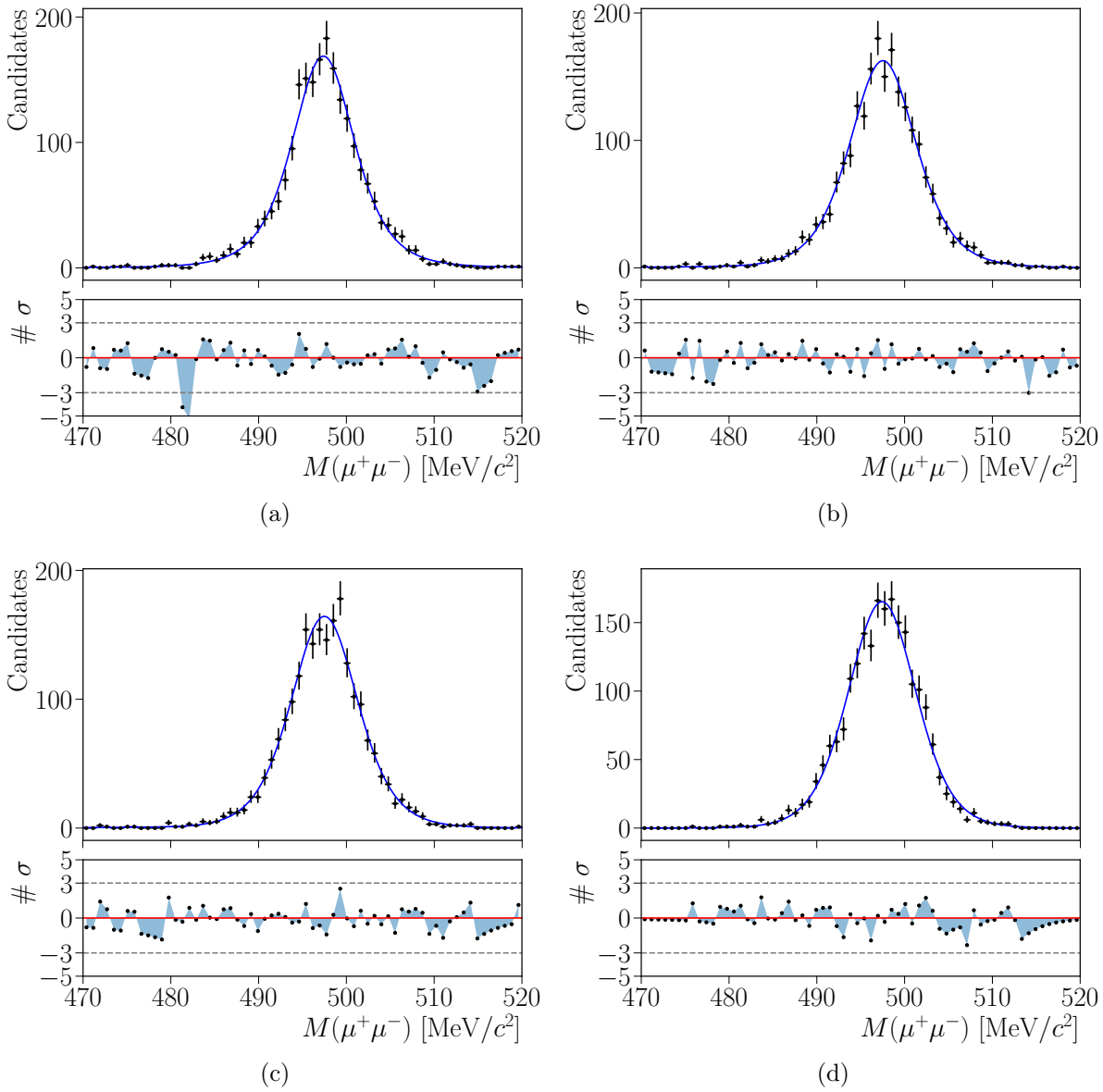

Figure D.2: Result of the fits to the dimuon invariant mass for simulated $K^0_S \to \mu^+\mu^-$ candidates with the muon momentum downscaled by 0.99939 for the middle four bins (3–6) of the TIS trigger category. The residual plots, showing the deviation of the fit curve to the data points, as a number of standard deviations, are displayed under their corresponding invariant mass plots. Parameters extracted in these fits, associated to the signal PDF, are fixed in the final fit to data.

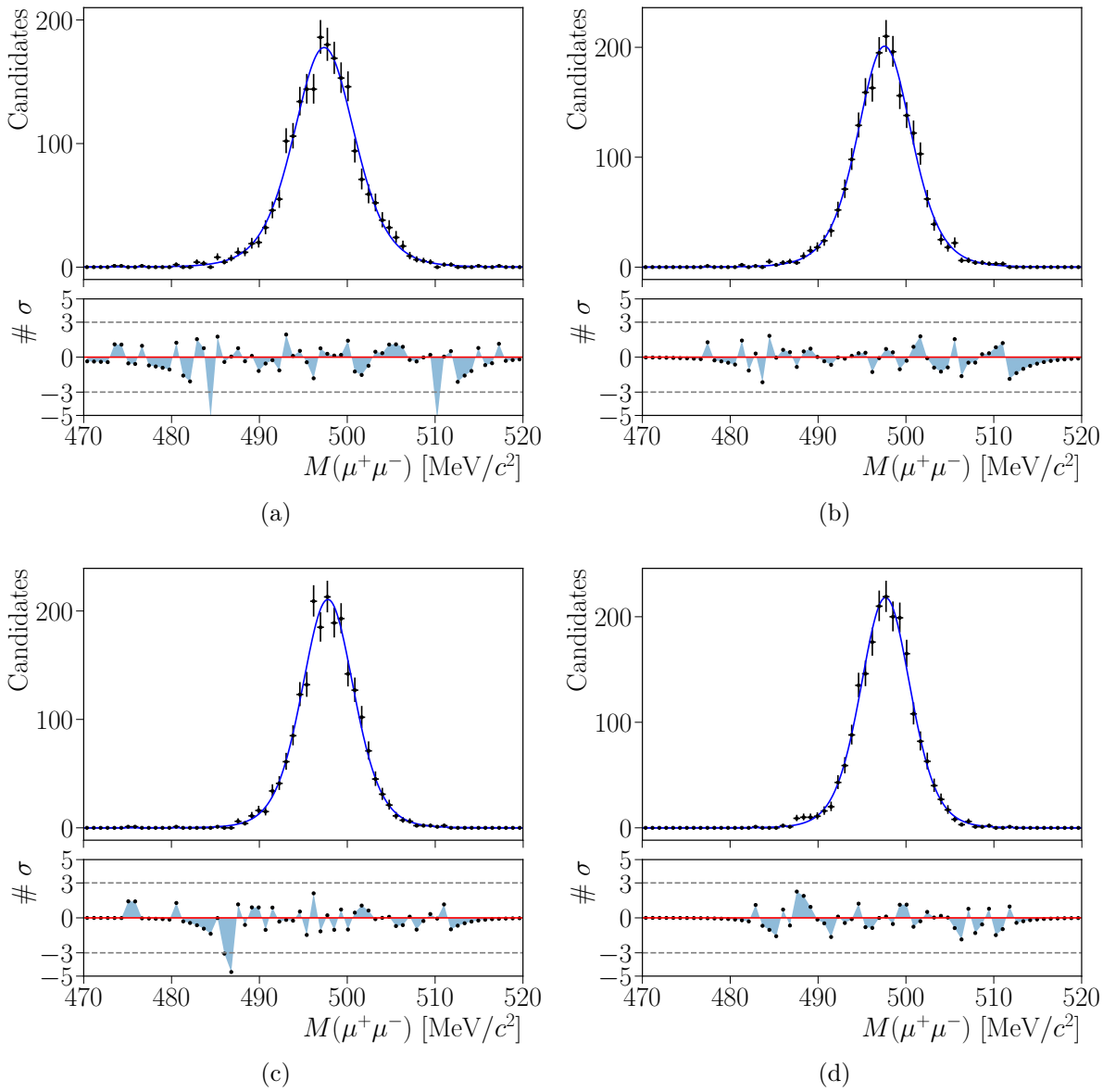

Figure D.3: Result of the fits to the dimuon invariant mass for simulated $K^0_S \to \mu^+\mu^-$ candidates with the muon momentum downscaled by 0.99939 for the last four bins (7–10) of the TIS trigger category. The residual plots, showing the deviation of the fit curve to the data points, as a number of standard deviations, are displayed under their corresponding invariant mass plots. Parameters extracted in these fits, associated to the signal PDF, are fixed in the final fit to data.

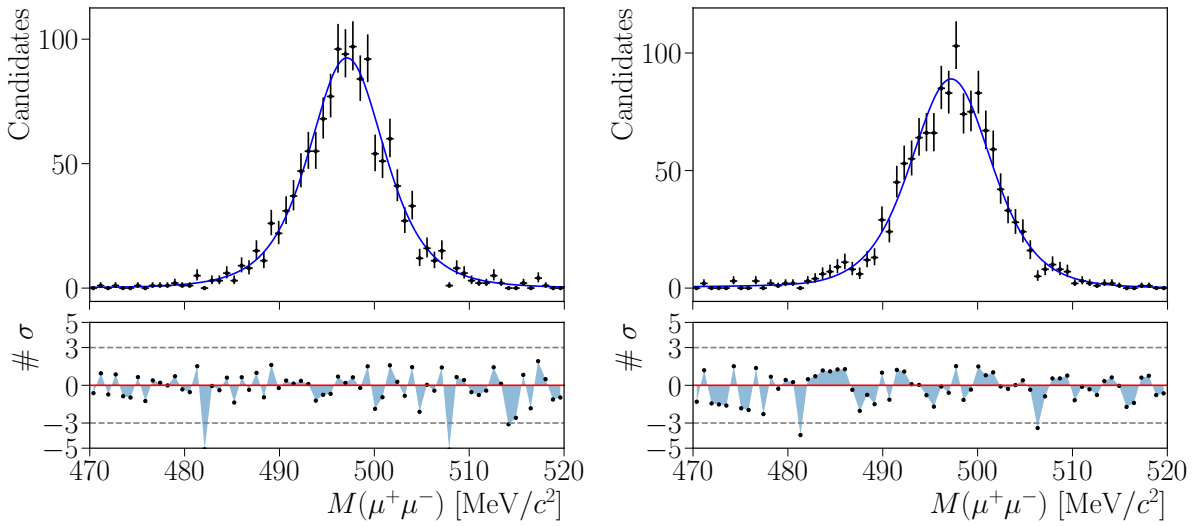

Figure D.4: Result of the fits to the dimuon invariant mass for simulated $K^0_S \to \mu^+\mu^-$ candidates with the muon momentum downscaled by 0.99939 for the first two bins (1–2) of the xTOS trigger category. The residual plots, showing the deviation of the fit curve to the data points, as a number of standard deviations, are displayed under their corresponding invariant mass plots. Parameters extracted in these fits, associated to the signal PDF, are fixed in the final fit to data.

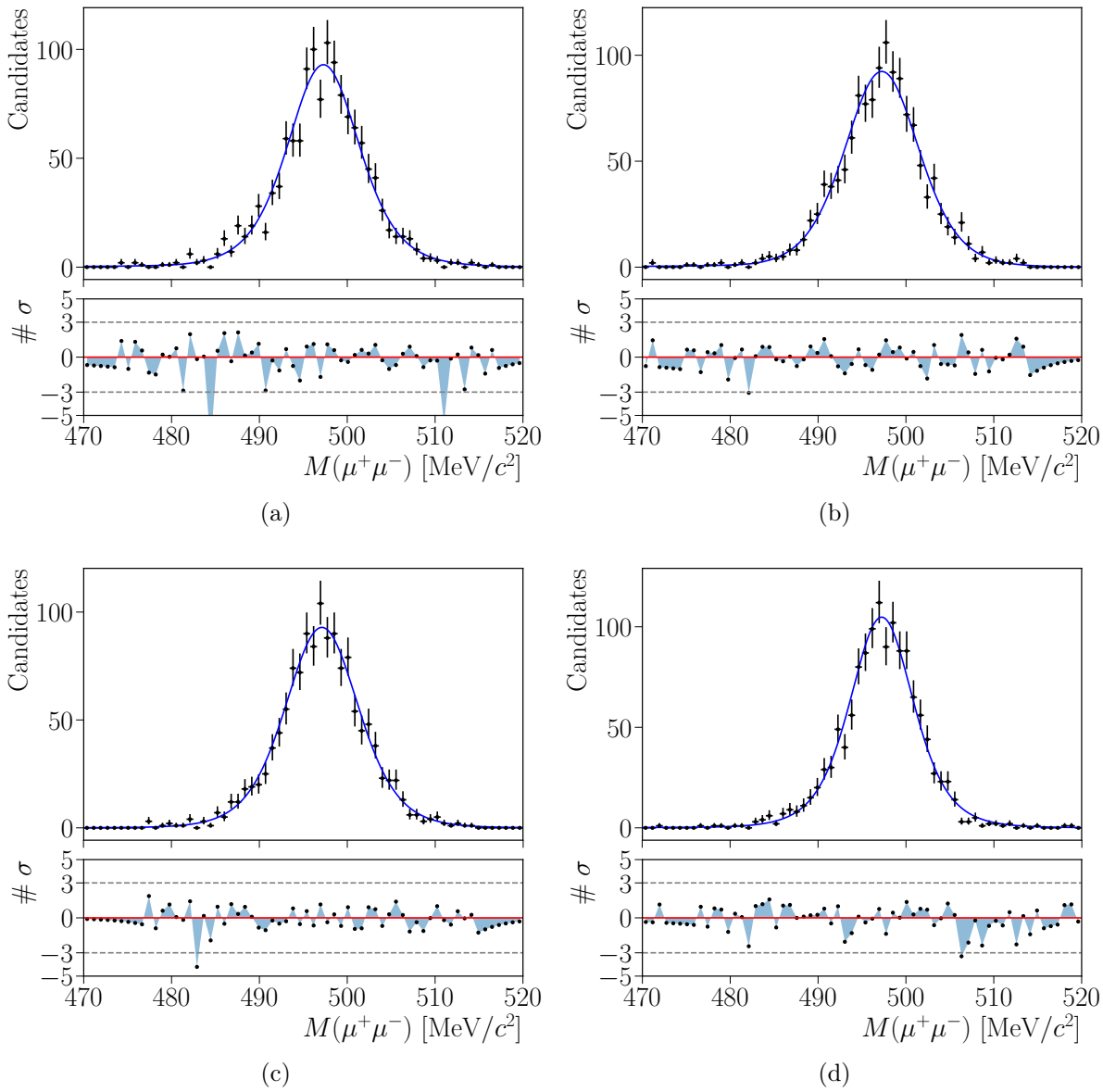

Figure D.5: Result of the fits to the dimuon invariant mass for simulated $K^0_S \to \mu^+\mu^-$ candidates with the muon momentum downscaled by 0.99939 for the middle four bins (3–6) of the xTOS trigger category. The residual plots, showing the deviation of the fit curve to the data points, as a number of standard deviations, are displayed under their corresponding invariant mass plots. Parameters extracted in these fits, associated to the signal PDF, are fixed in the final fit to data.

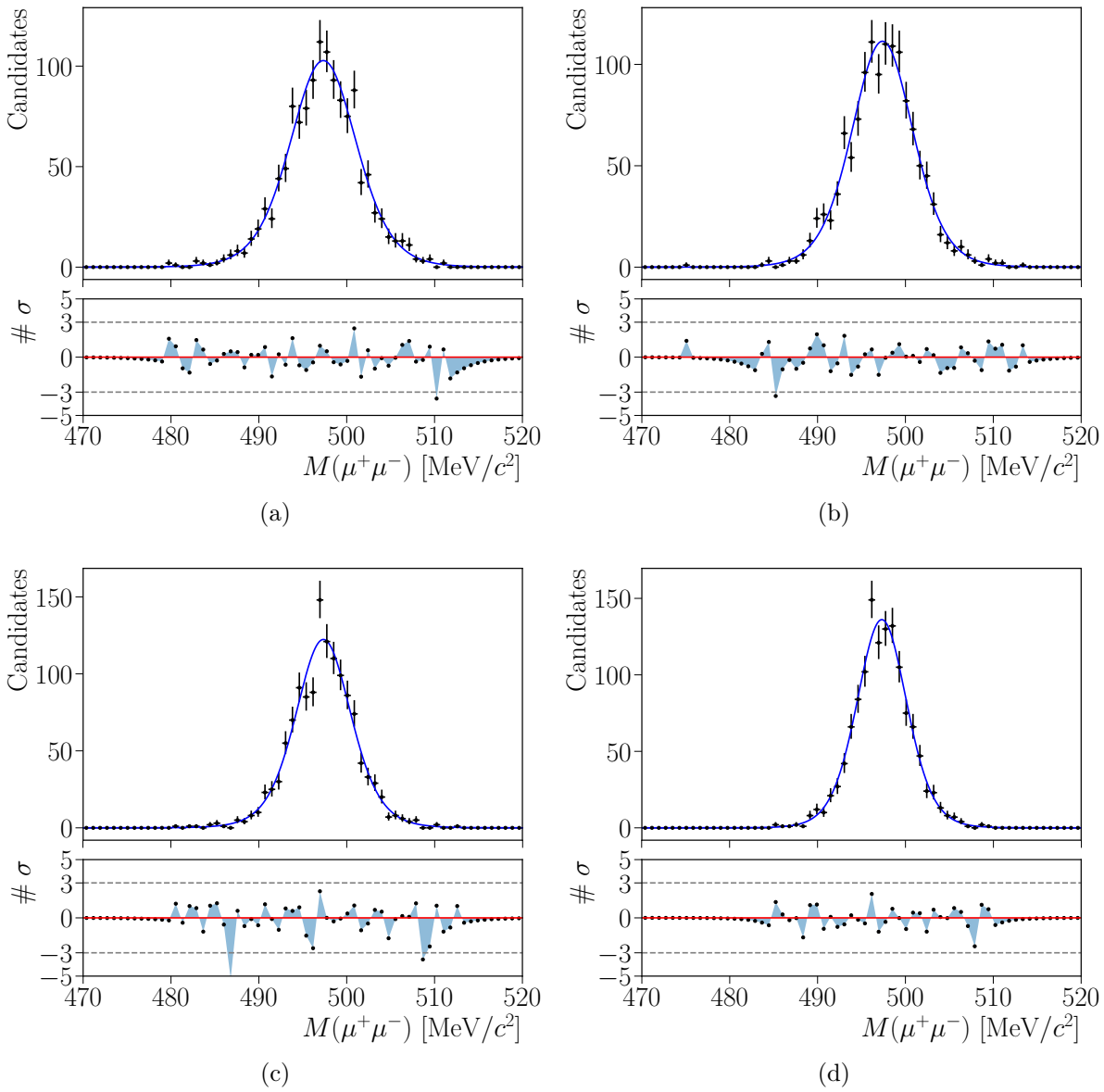

Figure D.6: Result of the fits to the dimuon invariant mass for simulated $K^0_S \to \mu^+\mu^-$ candidates with the muon momentum downscaled by 0.99939 for the last four bins (7–10) of the xTOS trigger category. The residual plots, showing the deviation of the fit curve to the data points, as a number of standard deviations, are displayed under their corresponding invariant mass plots. Parameters extracted in these fits, associated to the signal PDF, are fixed in the final fit to data.

E Fit results for all categories

In this appendix, the projections of the combined maximum likelihood fit to the twenty GBDT bins (ten per trigger category) are shown. The yield of $K^0_S \to \mu^+\mu^-$ decays is compatible with zero, and the likelihood profile of its associated branching fraction is used in order to calculate the limit.

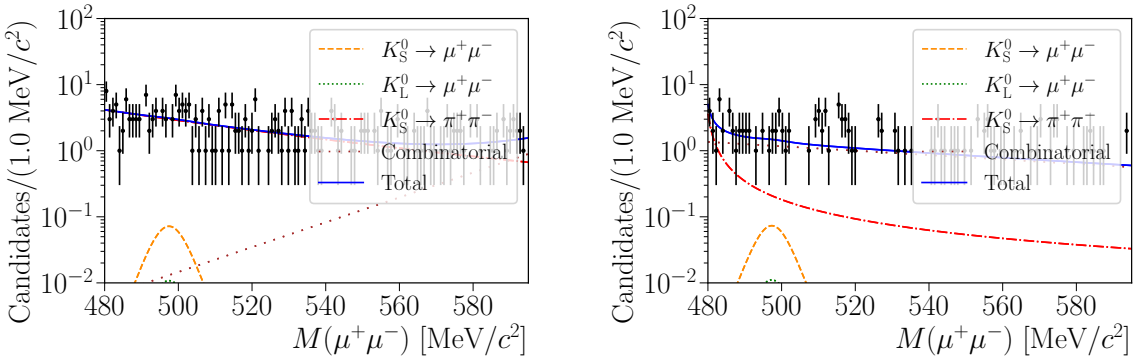

(a) (b)

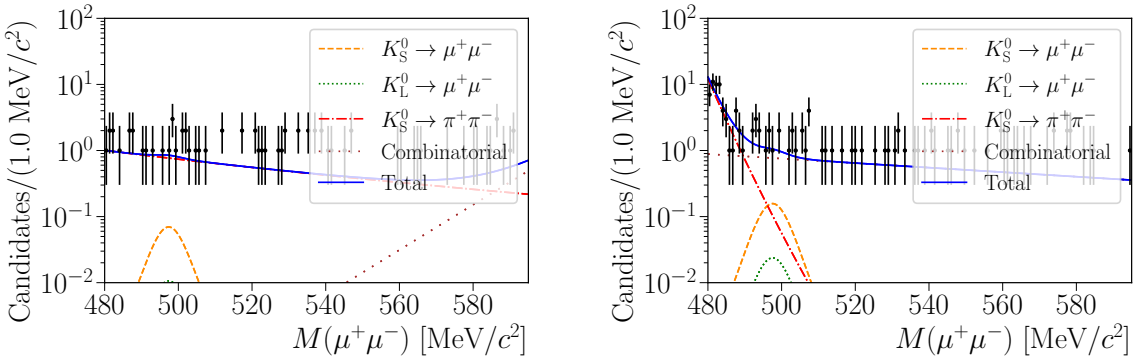

(c) (d)

Figure E.1: Projection of the combined maximum likelihood fit to the dimuon invariant mass of $K^0_S \to \mu^+\mu^-$ candidates for the TIS trigger category. The spectra for the ABDT bins 1–4 is shown, from left to right and from top to bottom.

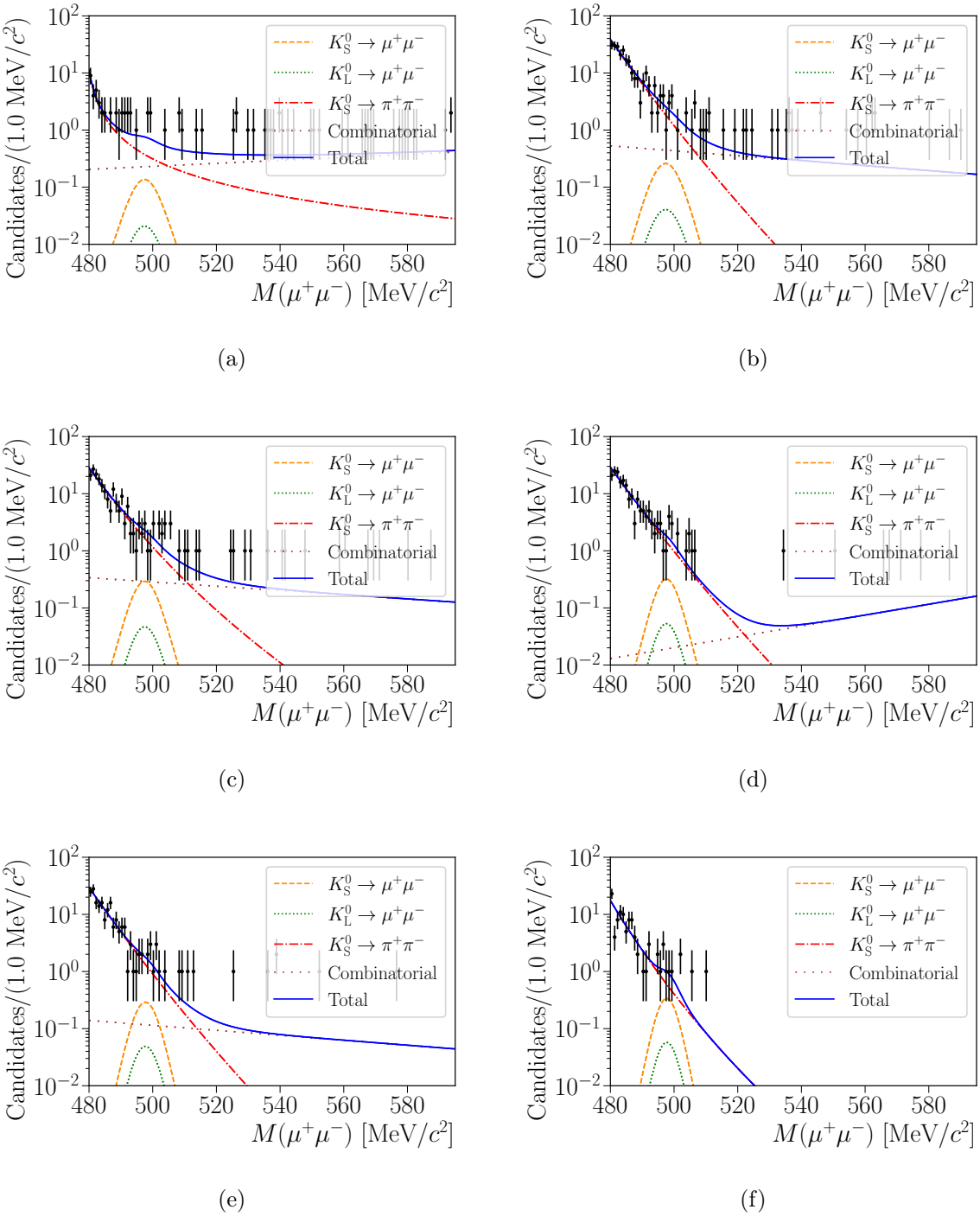

Figure E.2: Projection of the combined maximum likelihood fit to the dimuon invariant mass of $K^0_S \to \mu^+\mu^-$ candidates for the TIS trigger category. The spectra for the ABDT bins 5–10 is shown, from left to right and from top to bottom.

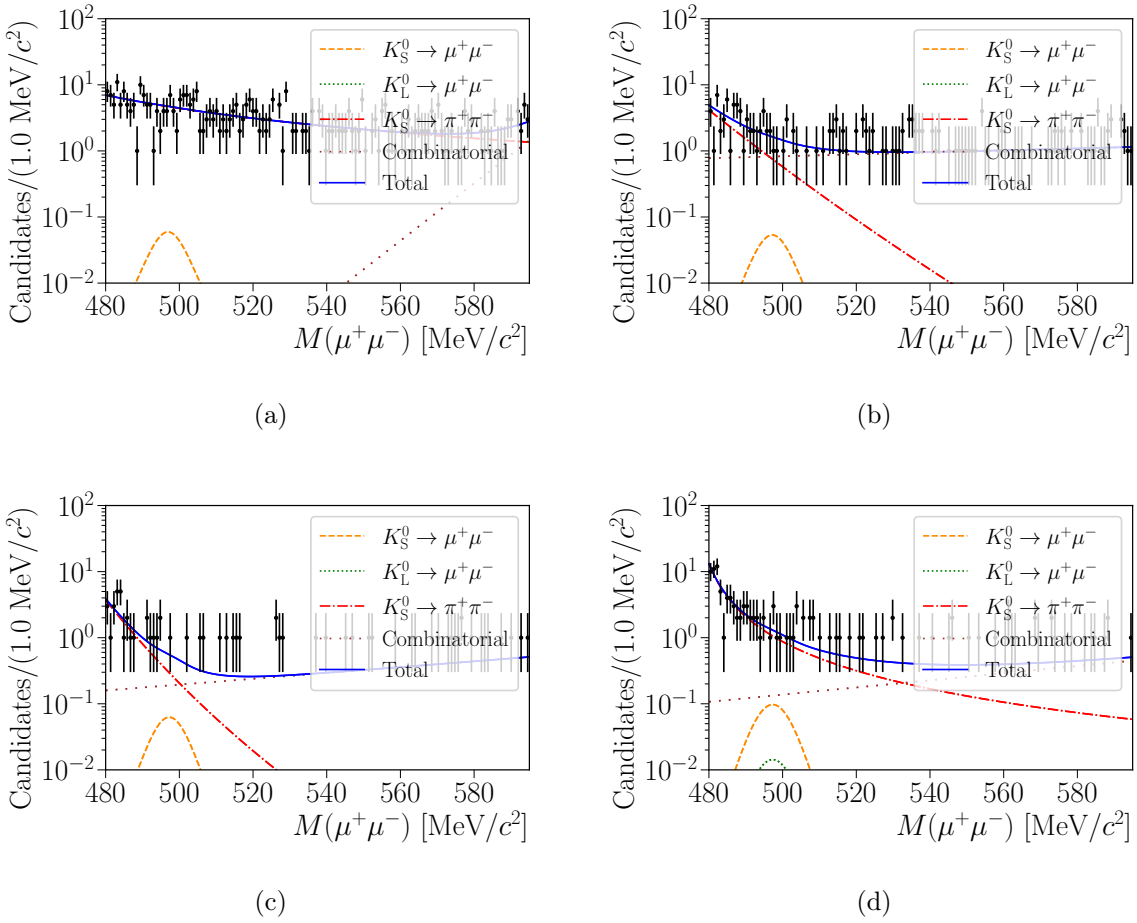

Figure E.3: Projection of the combined maximum likelihood fit to the dimuon invariant mass of $K^0_S \to \mu^+\mu^-$ candidates for the xTOS trigger category. The spectra for the ABDT bins 1–4 is shown, from left to right and from top to bottom.

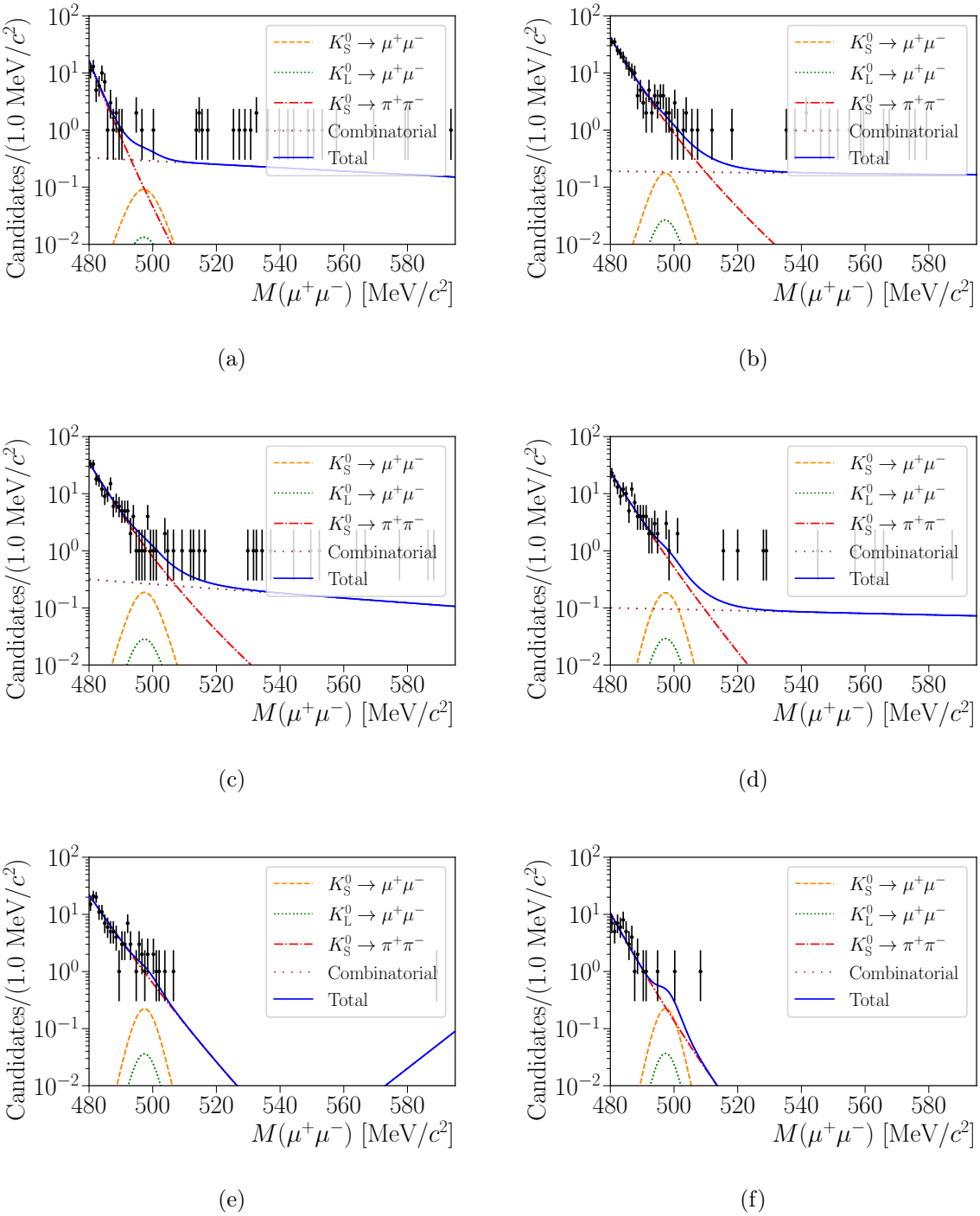

Figure E.4: Projection of the combined maximum likelihood fit to the dimuon invariant mass of $K^0_S \to \mu^+\mu^-$ candidates for the xTOS trigger category. The spectra for the ABDT bins 5–10 is shown, from left to right and from top to bottom.

F Resumo da tese en galego

F.1 Introdución teórica

O Modelo Estándar (SM) constitúe actualmente a teoría cuántica de campos para explicar as interaccións fundamentais entre partículas. A pesar de que consegue describir con gran precisión a meirande parte dos procesos, non é capaz de explicar fenómenos coma a oscilación de neutrinos [8,9], a gran asimetría entre materia e anti-materia no universo, a presenza de materia ou enerxía escura [13], ou a gravidade, unha interación que non se atopa recollida polo modelo. Elaborar unha nova teoría ou modelo resulta necesario para explicar os anteriores fenómenos, comunmente denominados como Nova Física (NP). Polo xeral, dende o punto de vista teórico trátanse de introducir novos graos de liberdade ao SM, na forma de novas partículas. De especial interese son os modelos baseados en supersimetría (SUSY) [14]. En SUSY, establécese unha invariancia baixo as transformacións de fermións (partículas con momento angular intrínseco, *spin*, semienteiro) a bosóns (partículas con *spin* enteiro). Os modelos baseados en SUSY, a parte de explicar os fenómenos non recollidos no SM mencionados anteriormente, ofrecen un vínculo coa gravidade e a teoría de cordas. Existen moitas outras posibilidades, dende extensións do SM onde se inclúen partículas adicionais para describir novas interacións, coma *leptoquarks* [25,26] ou quarks vectoriais [24], a modelos de dimensións extra ou teorías de gran unificación (GUTs). Polo momento, non existe un indicio claro que favoreza ningunha delas, e os resultados experimentais axudan a acoutar os parámetros libres destes modelos.

A busca de NP pode levarse a cabo de forma directa, producindo a nova partícula no laboratorio; ou de forma indirecta, estudando a súa influencia na desintegración doutras partículas. Experimentos coma ATLAS [65] e CMS [66] xeralmente tratan de facelo do primeiro xeito, mentres que outros coma LHCb [68], adoitan levalo a cabo polo segundo. Crear as novas partículas só resulta posible se un pode realizar colisións nunhas condicións determinadas, coma por exemplo, a unha enerxía lixeiramente superior á da nova partícula en cuestión. Os resultados obtidos en ATLAS e CMS non reflexan a existencia de ningunha nova partícula. Porén, no caso de que a masa invariante das novas partículas sexa moito maior á dos aceleradores actuais, a busca indirecta pode ser o único modo de estudalas.

No experimento LHCb, a busca de novas partículas lévase a cabo principalmente co estudo das desintegracións de hadróns con quarks b ou c. Nos últimos anos este detector amosou ser capaz de facer estudos moi interesantes de hadróns con quark s. Moitos fenómenos físicos, coma a violación CP [31], ou a existencia do quark c [30] descubríronse en estudos de desintegracións de partículas con quark s (*strange decays*). Desintegracións extremadamente raras de kaóns, coma $K \to \pi\nu\bar{\nu}$ ou $K^0_S \to \mu^+\mu^-$, deixáronse durante moito tempo de lado, debido á falta de medios para levar a cabo o seu estudo. As análises centráronse no estudo de partículas con máis alta masa, debido ao seu vínculo máis forte con NP, e ás expectativas xeradas sobre a existencia de SUSY. Non obstante hoxe en día, debido á posibilidade de producir estes hadróns en grandes cantidades, e ás melloras na discriminación de sinal, resulta posible estudar estas desintegracións. Os experimentos

NA62 [34] e KOTO [35] están a piques de recoller a suficiente cantidade de datos coma para probar a predición do SM para as desintegracións $K \to \pi\nu\bar{\nu}$, de gran interese dende o punto de vista teórico. Por outra banda en LHCb, debido á gran cantidade de mesóns K^0_S producidos, xunto con melloras na reconstrución e selección de candidatos, resulta posible estudar desintegracións coma $K^0_S \to \mu^+\mu^-$, altamente suprimidas no SM, nos que os efectos de contribucións por NP poden ser moi altos.

F.2 O detector LHCb

Situado no Centro Europeo para a Investigación Nuclear (CERN), LHCb é un detector dun só brazo que recolle información das colisións protón-protón producidas polo Large Hadron Collider (LHC). Está deseñado para reconstruír partículas cunha pseudorapidez entre $2 < \eta < 5$ e medir propiedades de hadróns con quarks b ou c xerados nas colisións. Na Fig. F.1 pódese ver a sección lateral do detector. Está composto por un sistema de detección de trazas de alta precisión, formado polo Vertex Locator (VELO) e o Tracker Turicensis (TT), ubicados antes do electroimán; e subdetectores adicionais ubicados a continuación, formados por unha rexión interna, o Silicon Tracker (ST), e outra externa, o Outer Tracker (OT). Nun experimento enfocado ao estudo da física do sabor coma LHCb, resulta esencial identificar o tipo de partículas detectadas. Os electróns e os fotóns identifícanse cun calorímetro electromagnético (ECAL). A información compleméntase co Scintillator Pad Detector (SPD) e o Preshower (PS), separados por un muro de chumbo. Estes dous subdetectores permiten distinguir entre π^0, fotóns e electróns. A distinción entre hadróns lévase a cabo con dous detectores de tipo RICH (RICH1 e RICH2), localizados antes e despois do electroimán. Isto permite distinguir entre pións, kaóns e protóns. Un calorímetro hadrónico (HCAL) proporciona información adicional para a identificación. Finalmente, os muóns son identificados usando cinco cámaras de muóns, que alternan placas de ferro e material detector. O material detector está composto de Multi Wire Proportional Chambers en rexións cerca de onde circulan os protóns, e Resistive Plate Chambers arredor.

O detector recolle datos cunha frecuencia de 40 MHz no Run 2 do LHC, o que supón un evento cada 25 ns. En cada evento pode haber varias colisións entre protóns, incluíndo distintos puntos de colisión (PV), aínda que en LHCb este valor é moi cercano a un. Dado que a maior parte dos eventos non conteñen información de interese resulta necesario filtralos. Isto lévase a cabo cun sistema de disparo, que reduce a frecuencia dos eventos de 40 MHz a 12.5 kHz en tres niveis. O primeiro (L0), implementado en *hardware*, é ríxido e pouco configurable. Os dous seguintes (HLT1 e HLT2), implementados en *software*, permiten unha alta configuración, adaptando facilmente as seleccións sobre os eventos aos intereses dos analistas. En cada nivel do sistema de disparo existen distintas seleccións, cada unha delas enfocada nun tipo de física ou desintegración distintos. A maiores, o sistema garda eventos sen ningún tipo de selección cada certo número de eventos (controlado por un parámetro de escala), o que aporta unha mostra sen sesgos polo sistema de disparo (MB). O sistema de sistema de disparo foi modificado no Run 2 para aumentar drasticamente a eficiencia para seleccionar *strange decays*. A eficiencia combinada de HLT1 e HLT2 aumentou cerca dunha orde de magnitude con respecto ao Run 1. Porén o L0, optimizado para estudar hadróns co quark b ou c, non puido ser modificado, e constitúe o factor limitante á hora de estudar *strange decays*.

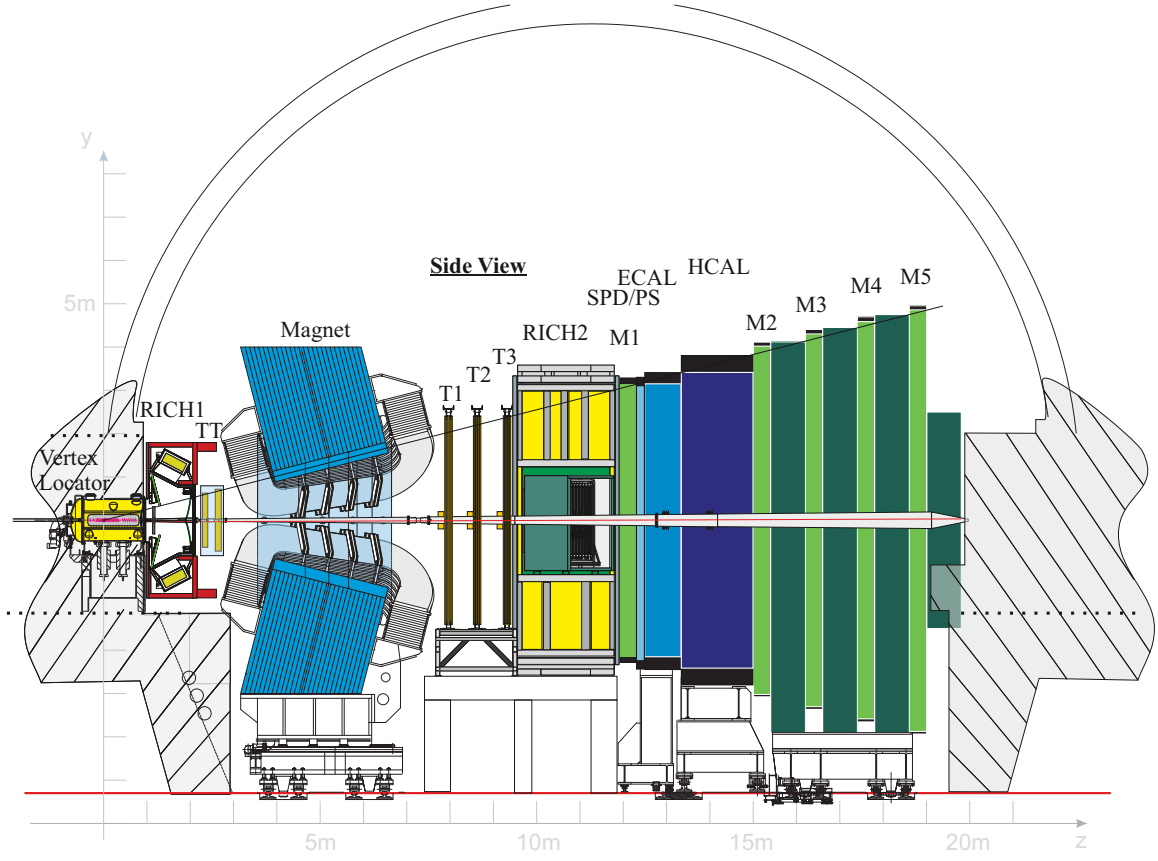

Figure F.1: Sección transversal do detector LHCb [68].

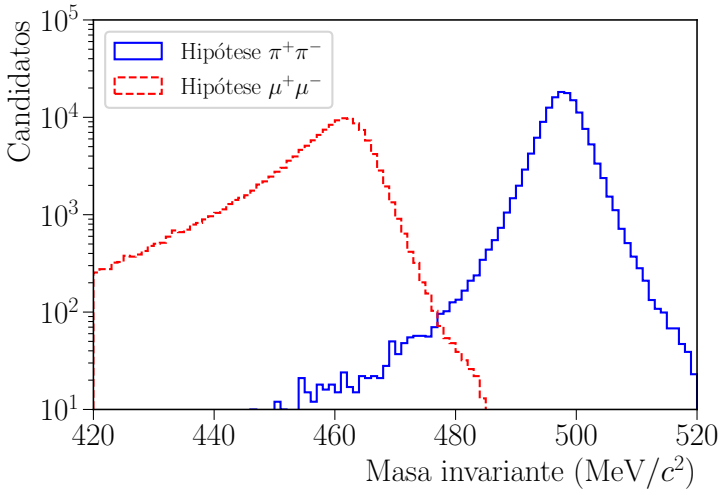

Figure F.2: Distribución da masa invariante de dous corpos para candidatos simulados de $K^0_S \to \pi^+\pi^-$, reconstruídos coma $K^0_S \to \pi^+\pi^-$ (azul continuo) e coma $K^0_S \to \mu^+\mu^-$ (vermello a raias). Os picos están separados por 40 MeV/c^2, o que se corresponde con 10 veces a resolución.

F.3 Busca da desintegración $K^0_S \to \mu^+\mu^-$

A desintegración $K^0_S \to \mu^+\mu^-$ está moi suprimida no SM. A predición para o seu cociente de ramificación é [47]

$$\mathcal{B}_{\text{SM}}(K^0_S \to \mu^+\mu^-) = (5.18 \pm 1.50 \pm 0.02) \times 10^{-12}. \tag{F.1}$$

O seu interese dende o punto de vista teórico nace pola alta sensibilidade á NP. Unha medida do cociente de ramificación $\mathcal{O}(10^{-11})$ permitiría poñer restricións na transición $s \to d\ell^+\ell^-$. No caso de que desintegracións coma $K \to \pi\nu\bar{\nu}$ indiquen un aumento da amplitude $s \to d\ell^+\ell^-$, a medida de $\mathcal{B}(K^0_S \to \mu^+\mu^-)$ permitiría discriminar entre escenarios de NP. Por outro lado, esta desintegración permite restrinxir modelos de SUSY [42] ou que inclúen leptoquarks [45].

Neste traballo levouse a cabo unha busca da desintegración $K^0_S \to \mu^+\mu^-$ con datos recollidos polo detector LHCb no Run 2 do LHC nos anos 2016, 2017 e 2018. Isto supón unha luminosidade de 5.6 fb^{-1}, recollida a unha enerxía no centro de masas de $\sqrt{s} = 13$ TeV. A selección básica de candidatos lévase a cabo con combinacións de dúas trazas, cada unha delas non compatible con provir dun PV e cun número determinado de *hits* nas cámaras de muóns. As traxectorias deben formar un vértice afastado do PV, pero a combinación debe resultar nunha partícula compatible con provir dun PV. Esta desintegración é limpa dende o punto de vista experimental, dado que ao reconstruír a masa invariante de dous muóns, nesta rexión de enerxías atópanse moi poucas contribucións doutras desintegracións. O fondo máis importante provén de $K^0_S \to \pi^+\pi^-$, cun cociente de ramificación $\mathcal{O}(10^{12})$ veces máis alto, onde os dous pións son misidentificados coma muóns. Debido á boa resolución do LHCb a esta enerxía, arredor de 4 MeV/c^2 (ver Fig. F.2), e grazas aos algoritmos de identificación de muóns, este fondo pode ser reducido drasticamente. Durante a análise, observouse un elevado número de candidatos provintes de interaccións inelásticas co material do VELO. Grazas ao bo coñecemento

da xeometría do subdetector [101], este fondo puido ser reducido eficientemente. Tanto a contribución por colisións inelásticas co material coma o fondo debido á combinación aleatoria de trazas no detector son reducidas usando un *Adaptive Boosted Decision Tree* (ABDT). Contribucións doutras desintegracións, coma $K^0 \to \pi\mu\nu$ ou $\Lambda \to p\mu\nu_\mu$, así coma desintegracións máis raras de hadróns con quark s, resultan desprezables. Debido á alta sensibilidade desta análise, decidiuse ter en conta a contribución por desintegracións do tipo $K^0_{\rm L} \to \mu^+\mu^-$, cuxo valor determinouse tendo en conta a eficiencia para $K^0_{\rm S} \to \mu^+\mu^-$ e a diferencia entre a vida media dos mesóns $K^0_{\rm S}$ e $K^0_{\rm L}$.

Para calcular o cociente de ramificación resulta necesario determinar a cantidade de mesóns $K^0_{\rm S}$ que se producen nas colisións. Isto lévase a cabo estudando candidatos a $K^0_{\rm S} \to \pi^+\pi^-$, un modo de desintegración que se escolle debido á súa semellanza a $K^0_{\rm S} \to \mu^+\mu^-$. Os candidatos a $K^0_{\rm S} \to \pi^+\pi^-$ obtéñense de mostras de MB, debido á baixa eficiencia do sistema de disparo para esta desintegración. A selección aplicada para $K^0_{\rm S} \to \pi^+\pi^-$ é idéntica á de $K^0_{\rm S} \to \mu^+\mu^-$, exceptuando as decisións no sistema de disparo e aos requisitos nos algoritmos de identificación de muóns. Isto fai que moitas incertezas sistemáticas se cancelen ao computar a normalización

$$\mathcal{B}(K^0_{\rm S} \to \mu^+\mu^-) = \frac{N^{\mu}_{\text{observados}}}{N^{\pi}_{\text{observados}}} \times \frac{\varepsilon^{\pi}_{\text{selección}}}{\varepsilon^{\mu}_{\text{selección}}} \times \frac{\varepsilon^{\pi}_{\text{sist. disp.}}}{\varepsilon^{\mu}_{\text{sist. disp.}}} \times \frac{1}{\varepsilon^{\mu}_{\text{muon-ID}}} \times \mathcal{B}(K^0_{\rm S} \to \pi^+\pi^-). \quad \text{(F.2)}$$

As eficiencias determínanse usando candidatos simulados corrixidos con datos, e o valor de $\mathcal{B}(K^0_{\rm S} \to \pi^+\pi^-)$ obtense de Ref. [1]. Os únicos parámetros restantes, $N^{\mu}_{\text{observados}}$ e $N^{\pi}_{\text{observados}}$, obtéñense a partir dos datos con axustes á masa invariante de dous muóns e dous pións, respectivamente.

O número de candidatos a $K^0_{\rm S} \to \mu^+\mu^-$ observados obtense dun *unbinned maximum likelihood fit* simultáneo a vinte mostras independentes, definidas en base ao valor do ABDT e aos requisitos no sistema de disparo. Na Fig. F.3 amósanse os resultados do axuste para as catro mostras na que a sensibilidade é maior. O espectro atópase dominado pola contribución de $K^0_{\rm S} \to \pi^+\pi^-$ dobremente misidentificado, cun fondo remanente composto por combinacións aleatorias de trazas e por interacións co material. A partir do axuste obtívose un valor de 34 ± 23 candidatos observados de $K^0_{\rm S} \to \mu^+\mu^-$, compatible con cero. O *profile* do *likelihood* de $\mathcal{B}(K^0_{\rm S} \to \mu^+\mu^-)$, combinado co resultado obtido para o Run 1 do LHCb [56], permite obter un valor:

$$\mathcal{B}(K^0_{\rm S} \to \mu^+\mu^-) < 2.1(2.4) \times 10^{-10} \text{ at } 90(95)\% \text{ CL}. \quad \text{(F.3)}$$

Este resultado supón o mellor límite ata a data, e permite restrinxir aínda máis os modelos de NP explicados na Sect. F.1.

Para o comezo da nova toma de datos, planeada para 2021, o detector LHCb vai sufrir unha actualización. O cambio máis importante para o estudo de $K^0_{\rm S} \to \mu^+\mu^-$ constitúe o deseño dun sistema de disparo baseado puramente en *software*. Isto permitirá incrementar a eficiencia para detectar esta desintegración en arredor dunha orde de magnitude, o que permitirá acadar un valor para o cociente de ramificación $\mathcal{O}(10^{-11})$. Valores cercanos á predición do SM probablemente só poderán ser explorados tras un hipotético Upgrade II do LHCb.

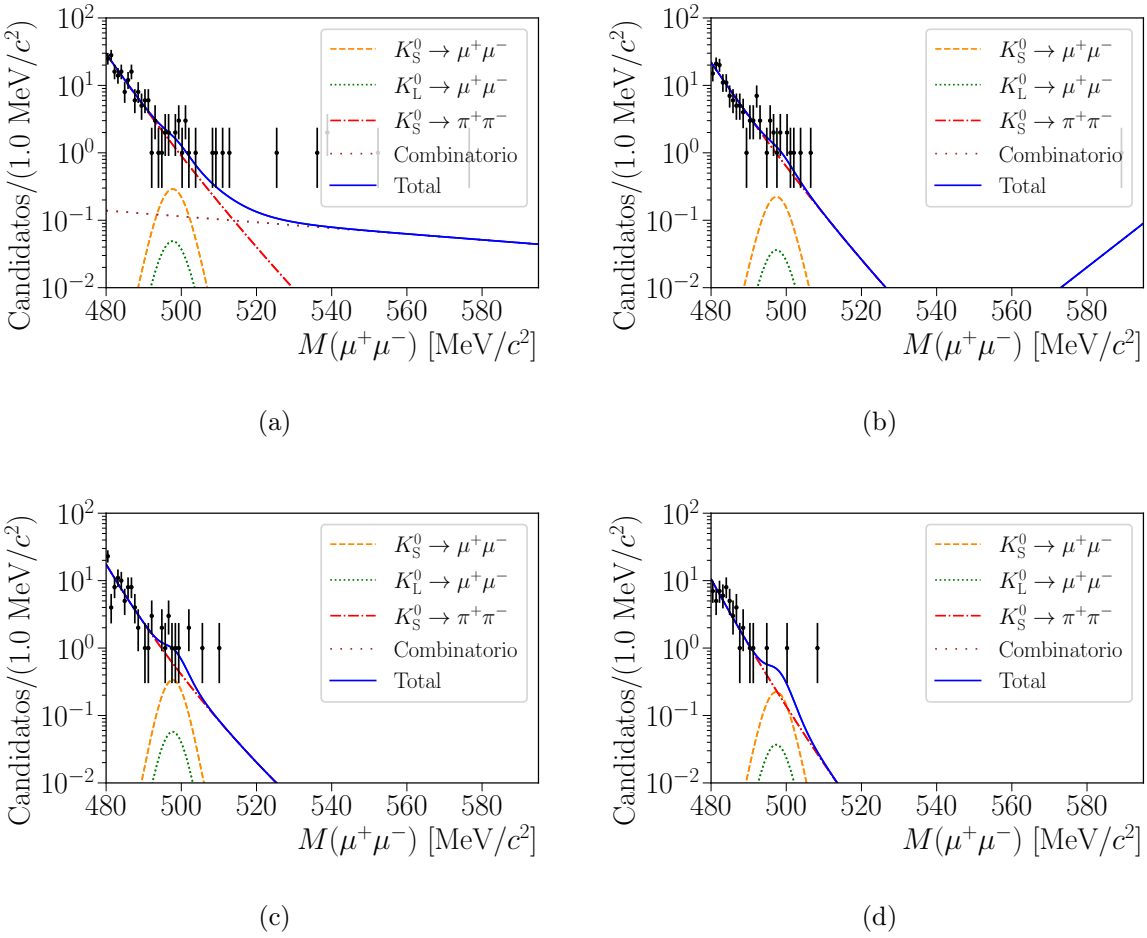

Figure F.3: Proxeccións do *unbinned maximum likelihood fit* á masa invariante de dous muóns para as catro mostras nas que a sensibilidade é maior. O espectro atópase dominado por desintegracións do tipo $K^0_S \to \pi^+\pi^-$, onde os dous pións son misidentificados coma muóns. A altas enerxías, pódese aprezar o fondo remanente de combinacións aleatorias de trazas e colisións inelásticas co detector.

F.4 Técnicas rápidas de reconstrución de muóns na actualización do detector LHCb

No *upgrade* do detector LHCb [71–73, 116], espérase traballar a unha luminosidade instantánea cinco veces maior que a do Run 2, incrementando de 4×10^{32} cm^{-2}s^{-1} a 2×10^{33} cm^{-2}s^{-1}. Debido ao aumento drástico da fluencia de partículas nos detectores, resulta necesario realizar modificacións tanto para soportar o aumento no dano por radiación coma para ser capaces de procesar toda a información. As modificacións máis importantes lévanse a cabo no VELO, que pasa a basearse nunha tecnoloxía de píxeles de silicio, o TT que pasa a chamarse UT e aumenta a súa granularidade, mentres que o ST e OT son substituídos polo SciFi, un detector de *scintillating-fibers*. Toda a electrónica e máis os sistema de adquisición de datos son modificados. Ademáis o L0 é retirado, dando paso a un sistema de disparo baseado unicamente en *software*. A eliminación deste nivel do sistema de disparo, necesario para ampliar o programa de física do experimento, constitúe un ambicioso proxecto, que supón un reto a nivel computacional. A reconstrución e o deseño do novo sistema de disparo deben ser capaces de procesar a información a unha frecuencia de 30 MHz. Os avances en programación, coma o uso de *multithreading*, e a inclusión de novas técnicas de reconstrución, indican que é posible manter ou incrementar as eficiencias do Run 2 para a maior parte do programa de física do LHCb, traballando nestas condicións tan extremas.

O sistema de disparo no *upgrade* está deseñado en dous niveis, HLT1 e HLT2. No primeiro nivel lévase a cabo unha reconstrución total das partículas do evento, engadindo unha información moi básica sobre a identificación de muóns. As seleccións neste nivel realízanse principalmente dende o punto de vista topolóxico, e decir, baseanse na xeometría da desintegración, o número de partículas a seleccionar, de onde proveñen e na súa cinemática. No HLT1 pódese levar a cabo unha identificación de muóns moi simple, baseada no número de *hits* nas cámaras de muóns asociados a cada traza. No HLT2 toda a información do detector se atopa dispoñible, mellorando a calibración de moitas magnitudes físicas e incluíndo unha completa identificación das partículas coa información dos detectores RICH, calorímetros e as cámaras de muóns. Neste último nivel, calquera técnica actualmente usada *offline* pode ser incluída.

O sistema de disparo no *upgrade* resulta beneficioso para a maior parte do programa de física do LHCb. Non obstante, o estudo de *strange decays* lévase a cabo cerca do límite da aceptancia do detector, a moi alta pseudorapidez. Debido ao baixo momento transverso das partículas que son productos das desintegracións deste tipo, as trazas a reconstruír sitúanse nas zonas de máis afluencia de partículas. Isto fai que a cantidade de combinacións que resulta necesario facer durante a reconstrución aumente drasticamente, o que imposibilita a reconstrución de todas as partículas a nivel de sistema de disparo. Non obstante, a maior parte das partículas nun evento son hadróns, os cales, polo xeral, non producen *hits* nas cámaras de muóns. O número de muóns por evento é moito máis reducido, polo que a reconstrución destas partículas para calquer rango de p_T resulta máis plausible. Introducindo a información das cámaras de muóns durante a reconstrución das trazas, resulta posible limitar o número de partículas a procesar, reducindo o tempo de execución.

A reconstrución no LHCb comeza no VELO, formando unha traza elemental. Esta

traza extrapólase ao UT, onde se promoven incluíndo información deste subdetector. Debido ao campo magnético remanente arredor do UT resulta posible ter, tras este paso, unha estimación do momento da partículas cunha resolución do ∼10%. Chegados a este punto, un ten que extrapolar as trazas a través do electroimán do LHCb e buscar *hits* nas cámaras de reconstrución que se atopan detrais, o SciFi, o que permite ter unha traza completamente reconstruída. Este proceso é moi custoso computacionalmente, e aínda máis ao traballar a moi baixo momento. Para partículas diferentes aos muóns, non existe ningunha maneira de reducir o número de trazas a procesar, debido a que a identificación nos detectores RICH consume demasiado tempo. Porén o número de *hits* presente nas cámaras de muóns é moito máis reducido. Extrapolando as trazas reconstruídas no UT directamente ás cámaras de muóns, resulta posible facer un filtrado, reducindo o número de obxectos a procesar. Neste traballo implementouse esta idea para o *upgrade* do LHCb. Este algoritmo, denominado `MuonMatchVeloUT`, está deseñado con especial interese para o estudo de muóns que proveñen de *strange decays*.

A eficiencia do algoritmo determinouse con candidatos simulados de colisións protón-protón en condicións do *upgrade*. Marcouse como comportamento ideal aquel correspondente á reconstrución normal de LHCb sen ningún tipo de requisito en p_T. Os resultados amosan unha redución do número de trazas a extrapolar dun factor 47, cunha pureza dun 2.5%, definida coma a fracción de muóns reais presente no conxunto de trazas que satisfán o algoritmo, incrementando o 0.1% obtido tras a reconstrución no UT. A eficiencia do algoritmo é de $\mathcal{O}(40\%)$, un factor 0.66 respecto á secuencia normal, para muóns $p_T < 1.5$ GeV/c. Esta diferenza en eficiencia é debido, en parte, ao feito de requerir que os muóns sobrevivan ata as cámaras de muóns e que xeren *hits* nelas, algo que non se leva a cabo na secuencia normal de reconstrución. Utilizando valores semellantes aos do Run 2 para a eficiencia de `IsMuon`, o requerimento básico para identificar muóns en LHCb, e que constitúe un 70% para muóns de baixo momento, obtéñense valores semellantes para a eficiencia total. Fixéronse estudos adicionais usando o entorno de traballo existente para o HLT no upgrade, tomando coma punto de partida as seleccións presentes no Run 2 do LHC para moitos tipos de *strange decays*. Os resultados reflexan unha eficiencia de 0.11% para $K^0_S \to \mu^+\mu^-$, 0.08% para $\Sigma^+ \to p\mu^+\mu^-$ e 0.04% para $K^0_S \to \pi^0\mu^+\mu^-$, cunha tasa de eventos gardados no rango 10–30 kHz para colisións protón-protón. Estes valores entran no rango das eficiencias de reconstrución e selección (sen requerimentos no sistema de disparo) do Run 2. Isto implica que as eficiencias totais poden mellorar respecto ao Run 2, establecendo boas expectativas para o *upgrade* do LHCb.

F.5 Conclusións

As desintegracións de hadróns con estrañeza seguen desempeñando un papel moi importante no estudo das interaccións fundamentais. Experimentos coma NA62 ou KOTO están a piques de medir os cocientes de ramificación das desintegracións $K \to \pi\nu\bar{\nu}$. A posible anomalía en ε'/ε, xunto coas buscas recentes de desintegracións raras de hadróns con estrañeza incrementan o interese neste campo. O detector LHCb, inicialmente construído para estudar desintegracións de hadróns con quarks b e c, amosa ser capaz de adaptarse e cubrir tamén desintegracións involucrando estrañeza. Co estudo de $K^0_S \to \mu^+\mu^-$ e $\Sigma^+ \to p\mu^+\mu^-$, xunto cos estudos preliminares das desintegracións $K^0_S \to \pi^0\mu^+\mu^-$ e $K^0_S \to \ell^+\ell^-\ell^+\ell^-$, o detector LHCb consegue facerse sitio neste campo.

Neste traballo presentouse a busca dunha das desintegracións máis raras da natureza, $K^0_S \to \mu^+\mu^-$. No LHCb, a excelente resolución na masa invariante de $\mathcal{O}(4\ \mathrm{MeV}/c^2)$ arredor da masa nominal do mesón K^0_S, xunto cunha identificación de muóns eficiente, permiten discriminar estas desintegracións de fondos perigosos, coma $K^0_S \to \pi^+\pi^-$ ou $K^0 \to \pi\mu\nu$. Tamén se observa un fondo moi importante procedente de interaccións inelásticas co material do detector, reducida grazas ao bo coñecemento da xeometría do LHCb. A sensibilidade actual suxeriu a consideración da contribución por desintegracións $K^0_L \to \mu^+\mu^-$ nos axustes á masa invariante dos dous muóns. Utilizando datos recollidos polo experimento LHCb no Run 2, a análise concluíu cun número de desintegracións $K^0_S \to \mu^+\mu^-$ e $K^0_L \to \mu^+\mu^-$ compatible con cero. Utilizando o *likelihood profile* do cociente de ramificación para $K^0_S \to \mu^+\mu^-$, e combinando o resultado co obtido na análise do Run 1, establécese un novo límite para esta desintegración de

$$\mathcal{B}(K^0_S \to \mu^+\mu^-) < 2.1(2.4) \times 10^{-10} \text{ at } 90(95)\% \text{ CL.} \tag{F.4}$$

Este resultado constitúe o límite máis baixo hoxe en día, e permitirá discriminar escenarios de nova física. En particular, esta desintegración está axudando a restrinxir diferentes modelos de supersimetría e de leptoquarks, complementado a información obtida por outros estudos, coma $K \to \pi\nu\bar{\nu}$ ou ε'/ε. Espérase que o detector LHCb poida baixar o límite trala súa actualización. A eliminación do L0, que constitúe hoxe en día a maior limitación para estudar desintegracións estrañas, revela un escenario prometedor, onde sensibilidades $\mathcal{O}(10^{-11})$ poden ser acadadas.

Para concluír, amosáronse resultados preliminares sobre técnicas de reconstrución a baixo momento transverso para a actualización do LHCb. Estas técnicas poden ser a única opción para manter a eficiencia actual de desintegracións estrañas no futuro do detector. Os resultados actuais revelan que a eficiencia total para estas desintegracións pode ser semellante á obtida no Run 2 sen perdas debido aos requerimentos do sistema de disparo. Isto tradúcese nunha mellora na eficiencia de arredor dunha orde de magnitude.

Acronyms and abbreviations

ABDT Adaptive Boosted Decision Tree. 35–38, 40, 41, 44, 45, 47–52, 54, 55, 57–61, 91, 92, 94–96, 98–101, 109–112, 117

BDT Boosted Decision Tree. 33, 40

CERN European Organization for Nuclear Research. iii, v, vii, 7, 11, 12, 114

DAQ Data Acquisition. 17, 65

DOCA distance of closest approach. 27, 32, 76

FE front-end. 67

FoI field of interest. 15, 73

GBDT Gradient Boosted Decision Tree. 27, 28, 47, 97, 99, 101, 109

HLT High Level Trigger. 18, 21, 22, 26, 30, 56, 57, 120

HPD Hybrid Photo-Detector. 66

IP impact parameter. 27, 30, 32, 39, 66, 68, 76

$\boldsymbol{\chi^2_{\text{IP}}}$ impact parameter significance. 27, 30, 32, 35, 76, 91

L0 Level Zero Trigger. 18

LEP Large Electron-Positron collider. 3, 11, 12

LFV Lepton Flavour Violation. 76

LHC Large Hadron Collider. iii, v, vii, 3, 5, 11–14, 17, 18, 22, 25, 51, 63, 65, 66, 81, 114, 116, 120

LS Long Shutdown. 65

MB minimum bias. 21, 26, 27, 30, 31, 51–55, 58, 79

MC Monte Carlo. 22, 27, 28, 30, 44, 47, 53, 54, 97, 99, 101, 103

MSSM Minimal Supersymmetric Standard Model. 5, 8

MVA multivariate analysis. 27, 33, 35

NN Neural Network. 17, 33

NP new physics. 7–12, 14, 63, 81

PDF probability density function. 51, 54, 57, 58, 103–108

PHSP phase-space. 44, 45

PMT photomultiplier. 66

PV primary vertex. 17, 18, 32, 33, 39, 56, 68, 69

QCD Quantum Chromodynamics. 1, 2, 4, 11, 20, 22

QED Quantum Electrodynamics. 1

QFT Quantum Field Theory. 1

ROC Receiver Operating Characteristic. 36, 40

SM Standard Model. iii, 1–7, 9–11, 25, 41, 62, 63

$\mathbf{s_{MB}}$ average downscale factor of the no-bias stream. 47, 51, 56

SUSY Supersymmetry. 5, 7, 10, 11, 81

SV secondary vertex. 27, 30, 32, 33, 35, 56, 66, 68, 94

TCK Trigger Configuration Key. 19, 21, 51, 54

TIS Triggered Independently of Signal. 19, 20, 30, 35, 36, 38, 41, 48–50, 53–61, 91–94, 97, 100, 101, 103–105, 109, 110

TOB Triggered On Both. 20

TOS Triggered On Signal. 19, 20, 30, 79

xTIS Exclusively Triggered Independently of Signal. 20

xTOS Exclusively Triggered On Signal. 20, 30, 35, 36, 38, 41, 48–50, 56–61, 91–94, 97, 100, 101, 106–108, 111, 112